Particle Deflection and Plate-out Dynamics in a Helium Stream

by

Hermanus Johannes Steyn

Thesis presented in partial fulfilment of the requirements for the degree of Master of Science in Mechanical Engineering at the University of Stellenbosch

Department of Mechanical and Mechatronic Engineering
University of Stellenbosch
Private Bag X1, 7602 Matieland, South Africa

Supervisor: Mr. R.T. Dobson

December 2009

Declaration

I, the undersigned, hereby declare that the work contained in this thesis is my own original work and that I have not previously in its entirety or in part submitted it at any university for a degree.

Signature: .....
HJ Steyn

Date: .....

Summary

In the primary circuit components of high temperature reactors, various unwanted particles have been found. These particles include, for example, graphite and silver-110 (^{110m}Ag). The silver-110 (^{110m}Ag) particles are radioactive, with a half-life of 253 days. The presence of radioactive particles in the primary circuit components constitutes an unwanted maintenance problem from a radiation hazard point of view. The development of a method to remove these particles from the helium stream is therefore needed. This thesis consideres two possible methods of removing silver from the helium stream, namely laser ablation of microparticles and electrostatic precipitation. These methods require the generation of silver ions or charged particles, the deflection of these particles in a helium gas stream passing through an electric field and the subsequent plate-out of these particles onto deflection electrodes.

To find a suitable method of generating ions, various methods to generate the silver ions were investigated and evaluated. These methods include existing ion sources, thermionic, field and photoelectric emission and laser ablation of microparticles. No existing ion sources could be found which could be utilised in helium at high pressure. From calculations it was concluded that thermionic, field and photoelectric emission could also not be used to raise the energy of the emitted electrons sufficiently to ionize silver in a helium flight path. These methods were found not to be feasible ion sources in helium at high pressures. However, laser ablation of microparticles was found to constitute a feasible technology.

Laser ablation was successfully utilised by Nichols *et al.* (2000) to deflect silver nanoparticles in an electric field across a two bar helium stream. An apparatus, similar to the one developed by Nichols *et al.* (2000), was designed and built. The apparatus included a silver insertion mechanism and tests with this apparatus were called the microparticle tests. To determine the efficacy of the silver insertion mechanism, the microparticle tests were done without the use of a laser. It was found that a laser was not necessary as microparticles collected on both the deflection electrodes. Dielectrophoresis was proposed as a possible explanation for the deflection and the plate-out of the mi-

croparticles.

To theoretically model the deflection of the silver particles, two models were proposed, namely the deterministic and the stochastic deflection models. The latter describes the deflection of atoms, ions and polarized particles by using probability theory. From this model it was found that the Brownian motion force is far larger that the force created by the polarizibility of the atom due to an electric field. The deterministic deflection model describes the deflection of larger particles in a continuum. From this model it was found that a silver microparticle with a radius of 3 μm in a helium stream with bulk velocity of 0.0198 m/s would deflect 4.6 μm per helium flight path length of 140 mm. From these calculation it was found that the apparatus which had been built was not long enough to deflect and plate-out all the silver microparticles.

The dielectrophoresis force on nanoparticles cannot be calculated, as the theory of dielectrophoresis is only valid for particles with diameter larger than 1 μm. Changes were therefore made to the apparatus to generate nanoparticles as their mobility is larger than that of microparticles. The nanoparticles were created by means of an arc discharge in helium; therefore tests with this modified apparatus were called the arc discharge test. The nanoparticles so created, deflected and deposited on both deflection electrodes. With the use of an atomic force microscope some of the particles could be classified as microparticles. According to the deterministic deflection model they should not have deflected. Combined with the fact that oxygen was in the plasma, due to the oxidation of the electrodes, a hypothesis of bipolar charging was thus proposed. The deterministic deflection model was used and supplemented with field and diffusion charging calculations, to support this hypothesis. A reasonable correlation between the theoretical model and this experimental results was obtained.

Based on the arc discharge test, electrostatic precipitation was proposed as the indicated means of scrubbing silver and other particles such as graphite from a helium stream. It is recommended that a new apparatus be built and that the deterministic deflection model be used to predict the deflection of the particles. With this apparatus the uncertainties of breakdown voltage, the effect of thermionic emission and the size of the particles, all of which have been identified as being important, can then also be determined.

Opsomming

In die primêre komponente van die kringloop van hoë temperatuurreaktors, was verskillende ongewenste partikels soos grafiet en silwer-110 (^{110m}Ag) teenwoordg. Silwer-110 (^{110m}Ag) is radioaktief met 'n halfleeftyd van 253 dae. Vanuit 'n radiasie-risiko oogpunt word daar onderhoudsimplikasies geskep deur die teenwoordigheid van radioaktiewe partikels in die primêre komponente. Die ontwikkeling van 'n metode om hierdie partikels uit die heliumstroom the verwyder was dus nodig. Hierdie tesis ondersoek twee moontlike metodes van verwydering van silwer uit die heliumstroom, naamlik laser-ablasie van mikropartikels en elektrostatiese presipitasie. Hierdie metodes benodig die generasie van silwer ione of gelaaide partikels, die defleksie daarvan in 'n heliumstroom wat deur 'n elektriese veld vloei en die platering van die partikels op defleksie elektrodes.

Om 'n geskikte metode the vind wat ione genereer was, verskillende metodes om die silwer ione te verkry, ondersoek en geëvalueer. Hierdie metodes sluit in bestaande ioonbronne, termioniese, veld en fotoëlektriese emissie en laser-ablasie van mikropartikels. Geen ioonbronne was gevind wat gebruik kan word in helium by hoë druk nie. Die gevolgtrekking is gemaak vanaf berekeninge dat termioniese, veld en fotoëlektriese emissie ook nie gebruik kan word om die energie van die voortgebronge elektrone genoeg te verhoog om silwer in 'n heliumstroom te ioniseer nie. Daar was gevind dat hierdie metodes nie geskik is as ioonbronne in helium by hoë druk nie. Daarenteen was laser-ablasie van mikropartikels gevind om 'n geskikte tegnologie voor te stel.

Laser-ablasie van mikropartikels was suksesvol deur Nichols *et al.* (2000) gebruik om silwer nanopartikels te deflekteer in 'n elektriese veld oor helium van twee bar. 'n Apparaat soortgelyk aan Nichols *et al.* (2000) se eksperiment, was dus ontwerp en gebou. Die apparaat het 'n silwer insitmeganisme bevat en toetse met hierdie apparaat was die mikropartikel toetse genoem. Om die effektiwiteit van die insitmeganisme te bepaal, was toetse gedoen sonder opstelling van die laser. Daar was eksperimenteel gevind dat die laser nie nodig was nie, omdat mikropartikels op beide defleksie elektrodes geplateer het. Dielektroforese was voorgestel as 'n moontlike verduideliking vir de-

flektering en platering vir die silwer mikropartikels.

Om die defleksie van silwer partikels teoreties te moduleer was twee modelle voorgestel, naamlik deterministiese en stogastiese defleksiemodelle. Laasgenoemde beskryf die defleksie van atome, ione en gepolariseerde partikels deur gebruik te maak van waarskynlikheidsteorie. Die stogastiese defleksiemodel dui aan dat die Brownian bewegingskrag veel groter is as die krag wat geskep word deur die polarisasie van 'n atoom as gevolg van 'n elektriese veld. Die deterministiese defleksiemodel beskryf die defleksie van groter partikels in 'n kontiuum. Met hierdie model was gevind dat silwer mikropartikels met 'n radius van 3 μm in 'n heliumstroom van snelheid van 0.0198 m/s, 4.6 μm sal deflekteer per 140 mm van heliumstroom lengte. Dit bewys dat die apparaat wat gebou was, se lengte onvoldoende was om al die silwer mikropartikels te deflekteer en te laat neerslaan.

Die dielektroforese krag van nanopartikels kan nie uitgewerk word nie, omdat die dielektroforese model slegs geldig is vir partikels groter as 1 μm. Veranderings was dus aan die apparaat gemaak om nanopartikels te genereer omdat hul mobiliteit hoër is as die van mikropartikels. Die nanopartikels was geskep deur gebruik van 'n boogontlading in helium; daarom was toetse met hierdie gemodifiseerde apparaat die boogontladingstoets genoem. Die nanopartikels wat so geskep was, het gedeflekteer en het op beide elektrodes neergeslaan. Met die gebruik van 'n atomiese krag mikroskoop was dit gevind dat sommige van hierdie partikels mikropartikels was. Volgens die deterministiese defleksiemodel moes hul nie gedeflekteer het nie. Gekombineerd met die feit dat daar, weens oksidasie van die elektrodes, suurstof in die plasma was, was 'n hipotese van bipolêre lading voorgestel. Die deterministiese defleksiemodel is saam met die veld- en diffusielading gebruik om hierdie hipotese te staaf. 'n Redelike korrelasie tussen die teoretiese en eksperimentele data was gevind.

Gebaseer op die boogontladingstoets, was elektrostatiese presipitasie voorgestel as 'n metode om silwer en ander partikels soos grafiet uit 'n heliumstroom te verwyder. Daar word voorgestel dat 'n nuwe apparaat gebou word en dat die deterministiese defleksiemodel gebruik word vir die bepaling van defleksie van die partikels. Deur die nuwe apparaat te gebruik kan die onsekerhede van deurslagspanning, effek van termioniese emissie en grootte van die partikels wat geidentifiseer is as belangrik, ook bepaal word.

Contents

List of Figures

List of Tables

Nomenclature

Constants

e	electron charge [1.602192x10^{-19} C]
g	gravitational acceleration [9.81 m/s^2]
$\hbar$	Planck's constant [6.62075x10^{-34} Js]
k_B	Boltzmann's constant [1.38066x10^{-23} J/K]
N_A	Avogadro's constant [6.022137x10^{23} g/mol]
R	Universal gas constant [8.3145 J/mol K]

Variables

A	area [m^2], constant
C	capacitor, capacitance [F]
c	distance between two centres
C_m	Cunningham correction factor
c_p	specific heat capacity [J/kgK]
d	diameter [m], distance [m]
D	duty cycle, drain
e	electomotive force
E	energy [J], electric field [V/m]
$\langle E \rangle$	total average energy [J]
F	force [N], fluence [J/cm^2]
f	friction coefficient, frequency [Hz]
G	gate of transistor
q	charge [C]
Q	flow rate [m^3/s]
H	height [m]

$\Delta_{vap}H$	enthapy of evaporation [J/mol]
i	current [A]
I	density of light flux [W/cm^2]
IP	ionizational potential [eV]
J	current density [A/cm^2]
k	loss coefficient, thermal conductivity [W/mK]
K	flow coefficient
K_{CM}	Clausius-Mossotti function
l	length [m]
L	inductance [H]
L_v	latent heat of evaporation [J/g]
m	mass [kg], dipole moment [Cm]
$\dot{\mathrm{m}}$	mass flow rate [kg/m^3]
M	molecular mass
N	number
n	number of moles
p	pressure [bar, Pa], position [m]
r	reflection coefficient, radius [m]
R	radius of a praticle [m], resistance [Ω]
Re	Reynolds number $Re = \rho v d_h / \mu$
S	source of transistor
S_x	standard deviation
T	temperature [K]
t	time
u	internal energy
v	velocity [m/s]
V	volume [m^3], voltage [V]
$\dot{\mathrm{W}}$	Work [J]
Y_c	compressibility factor
$\overline{x}$	sample mean
X	distance [m]
x	varying distance [m]
z	height [m]

Greek symbols

α	ionization constant, polarizibility [Cm^2/V]
	thermal diffusitivity [m/s^2] $\alpha = k/\rho c_p$
γ	secondary electron emission coefficient
δ	difference
ε	permittivity [F/m]
ζ	current ratio, Riemann-zeta function
θ	polar coordinate
λ	mean free path [m]
μ	viscosity [kg/ms], permanent electric dipole moment [Cm]
ξ	random vector
ρ	density [kg/m^3], resesitivity [Ωm], charge density [C/m^3]
σ	conductivity [Sm^{-1}], collision cross-section [cm^2]
τ	mean free time [s]
ϕ	work function [eV], electric potential [V], magnetic flux

Subscripts

a	atom, above
A	anode
Ag	silver
b	below
B	breakdown
c	critical
C	cathode
cap	capacitor
d	diode
DS	drain to source
e	electron, electrons per volume
ec	electrostatic
ef	effective
$elec$	electric field
es	electrode spacing
exp	experiment
bc	before collision

f	Fermi
F	Field emission
$f0$	Fermi energy at 0 K
g	gas
G	ground
h	hydraulic
He	helium
i	individual element
im	image
l	left
m	molecules per volume, middle
n	neutral
o	output
or	orifice
p	most probable, pipe, particle
P	primary
r	right
res	result
rel	relative
S	secondary
T	thermionic
TN	threshold
v	vapour
ves	vessel
w	water
0	initial electrons

Abbreviations

ac	alternating current
APTD	atmospheric pressure Townsend-like discharges
DEP	dielectrophoresis
EA	electron affinity
emf	electromotive force
ESP	electrostatic precipitation
ICP	inductively coupled plasma

IRZ	initial radiation zone
LA	laser ablation
LAM	laser ablation of microparticles
LIS	laser ion source
MIP	microwave induced plasma
MS	mass spectrometry
NAZ	normal analytical zone
NMISA	National Metrology Institute of South Africa
RF	radio frequency
SXPS	scanning X-ray photoelectron spectroscopy

Chapter 1

Introduction

Various unwanted particles (for example graphite, silver, cecium, strontium, etc.) have been found in the primary circuit components of high temperature reactors (Bäumer, 1990). Silver-110 (^{110m}Ag) is predominantly released from intact coated fuel particles (van der Merwe, 2004) and is reported to have the highest dose rate of the released fission products (Sawa *et al.*, 2004). Access of personnel for maintenance is limited as a result of reduced safe exposure times, which is due to the radiation fields created by the deposits of fission product (van der Merwe and Clifford, 2008). The radiation fields are mostly created by silver-110 (^{110m}Ag) with a half life of 253 days (Sawa *et al.*, 2004).

PBMR (Pty) Ltd is a South African company that intends to build a demonstration high temperature reactor. The acronym PBMR is short for pebble bed modular reactor and as the name suggests, the reactor contains fuel pebbles and can be constructed as seperate but modular units in order to take advantage of economies of scale and step wise power output as demand increases. Low enriched uranium (approximately 10% U^{235}) triplecoated isotropic particles are contained in the fuel spheres. Helium is used as an energy transfer medium from the reactor core to the gas-turbine and generator system. This technology has proven successful, as evidenced by a system that operated for more than 20 years in Jülich, Germany (Bäumer, 1990).

PBMR's objective of improving an excellent design by enhancing safety characteristics requires the removal of the unwanted particles. Although various removal techniques can be envisaged, such as removal by magnetic fields or centrifugal forces, the task of creating silver ions in a helium environment for subsequent deflection in an electric field is investigated in this thesis. The deflection is to be of such a magnitude that the particles would adhere or plate-out onto the surface of the electrodes, hence the title: particle deflection and plate-out dynamics. The objectives of this thesis can thus be

given as the generation of ions or charged particles in helium, the deflection thereof in an electric field and the subsequent plate-out dynamics of these particles. Finally, a recommendation is to be made for PBMR to scrub silver from the designed system.

The content of this thesis attempts to describe the steps followed to achieve the objectives. An extensive literature study, given in chapter 2, provides an investigation into existing ion sources and a basic understanding of the physical environment which could influence the experiments which were conducted. The theory of electron emission from metals was investigated in chapter 3 as a means of generating electrons to ionize silver in their flight path. Chapters 4 and 6 explain the experimental setups and results. The models used to calculate the deflection of the silver particles are explained in chapter 5. In chapter 7 the decisions made to achieve the objectives prescribed for this thesis are discussed and conclusions are drawn based on the results obtained from the tests and literature study. In chapter 8 a possible means of scrubbing silver and other particles is proposed as well as future work. Appendix A contains the derivations of a number of equations that were needed in the investigation. The remaining appendices illustrate the orifice flow meter calculations, safety and operational procedures of the experiments and a number of sample calculations.

Chapter 2

Literature study

The extensive literature study presented in this chapter undertakes an investigation into the technology of creating ions, or charged particles, and of deflecting them. The creation of ions is investigated and discussed in the sections of existing ion sources, ionization and laser ablation. The section on electrostatics of particles presents an analysis of the creation of charged particles and deflection of those charged particles.

2.1 Existing ion sources

This section identifies and discusses various existing ion sources which are predominantly used as sample introduction methods for mass spectrometry (MS). MS is a method whereby a compound, which has undergone fragmentation and ionization, is elementally and istopically analysed (Niu and Houk, 1996).

2.1.1 Liquid metal ion source

A liquid metal ion source (LMIS) consists of a liquid metal which is contained inside a heated reservoir, see figure 2.1. A needle (the anode) with a sharp tip protrudes from the reservoir. The liquid metal flows along the needle to cover the tip and the extracting electrode is placed opposite the needle. A voltage of 2-10 kV (Sato *et al.*, 1993) is applied. Electrons move from the cathode to the anode needle in the vacuum between them. Once the electrons reach the anode they interact with the liquid metal atoms, which ionizes the atoms. These ions are then attracted towards the cathode.

Some of the ions pass through the collimating hole in the extracting electrode, which creates the LMIS.

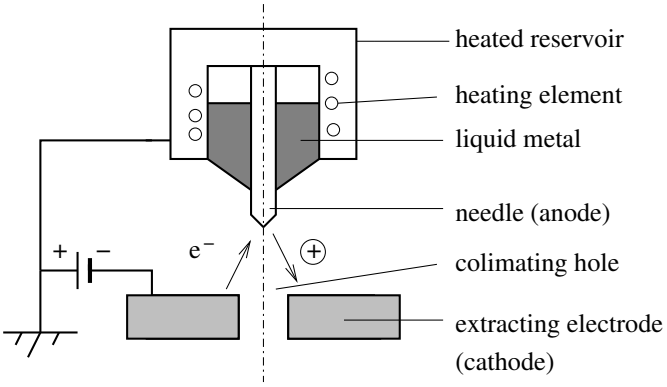

Figure 2.1: The LMIS (Sato *et al.*, 1993)

2.1.2 Inductively coupled plasma

Koirtyohann *et al.* (1980) stated that ions are generated in an inductively coupled plasma (ICP). The plasma is created by a high-frequency current passing through the radio

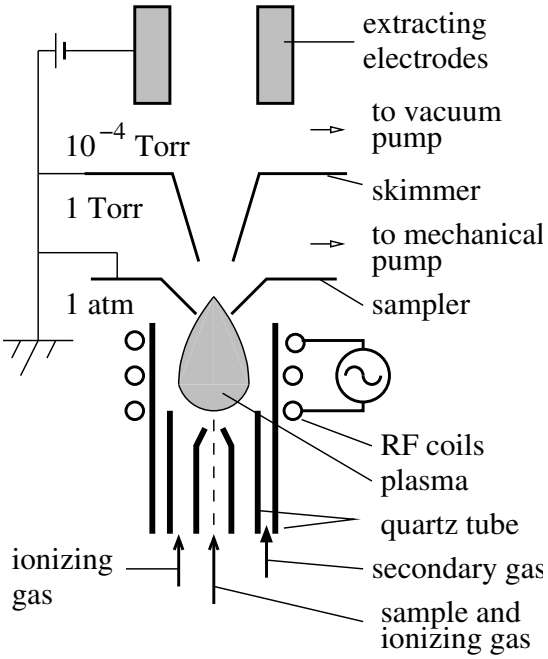

(a) A schematic of the ICP (Niu and Houk, 1996)

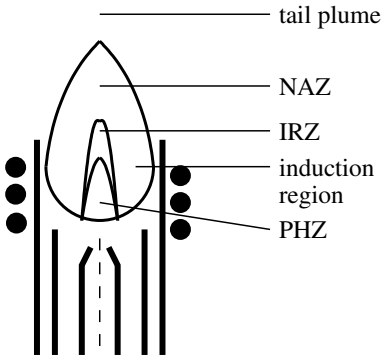

(b) Schematic view of various zones of the ICP (Koirtyohann *et al.*, 1980)

Figure 2.2: The ICP

frequency (RF) coils, shown in figure 2.2(a). The rapid changes in the magnetic fields induce eddy currents in the gas and resistance to these eddy currents produce temperatures of up to 10 000 K, according to Niu and Houk (1996). The sample, i.e. the material to be ionized, is inserted in various ways but most commonly as an aqueous solution (Niu and Houk, 1996). The inserted solution, with the flow of the sample gas, is called the aerosol. As the aerosol moves through the centre of the plasma, the droplets are dried and vapourized into molecules, which are then atomized and ionized. The function of the secondary gas is to serve as a coolant to protect the quartz tubes from the elevated temperatures.

The plasma produced by an ICP, as described by Koirtyohann *et al.* (1980) and shown in figure 2.2(b), consists of various zones. The initial radiation zone (IRZ) consists mostly of molecular species and neutral atoms, the normal analytical zone (NAZ) consists of ions while the tail plume consists of neutral atoms. After the plasma has been created by the ICP, the sampler and skimmer, as indicated on figure 2.2(a), are used to extract the ions. The placement of the sampler relative to the IRZ influences the characteristics of the spectra (Niu and Houk, 1996). Note that the pressure decreases as the ions propagate to the next section and that the pressure in the extaction electrode region is 10^{-4} Torr.

2.1.3 Microwave induced plasma

In a microwave induced plasma (MIP) a quartz tube is heated by microwaves which then releases charged particles (Zander and Hieftje, 1978). These charged particles supply electrons, which ionizes the helium inside the quartz tube. The ionized helium leads to plasma ignition. The aerosol is forced through the plasma, whereafter atomic emission is detected (Zander and Hieftje, 1978).

2.1.4 Laser ion source

When a metal is ionized by means of a laser it is referred to as a laser ion source (LIS). Two means of injecting the metal molecules into the laser path are considered in this section, namely sputtered silver clusters and a hot cavity.

Wucher (1993) conducted experiments where a silver sample, under high vacuum, was bombarded with an argon ion beam, hence the name sputtered silver clusters. After bombardment the silver clusters were ionized, see figure 2.3(a). Ionization of the silver clusters, of up to 20 atoms, was achieved by means of photo-ionization, see section 2.2.

Wucher (1993) found that ionizing larger clusters was more effective when using an F_2 excimer laser with a wavelength of 157 nm, than when using a ArF excimer laser with a wavelength of 193 nm. The wavelength is important as this infuences the choice of laser to be used.

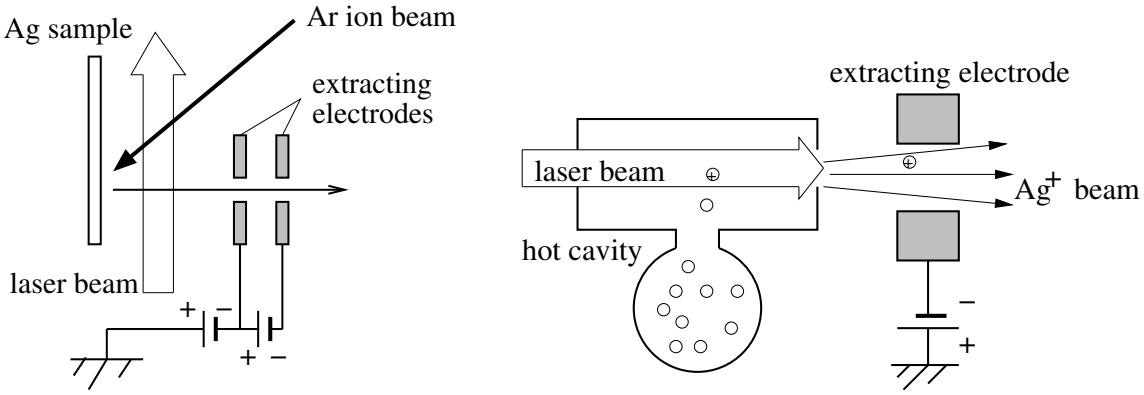

(a) Sputtered silver cluster (Wucher, 1993)

(b) Hot cavity (Alkhazov *et al.*, 1991)

Figure 2.3: Laser ion sources

In the case of a hot cavity, a sample metal is evaporated, whereafter the metal atoms are ionized by multi-resonance photo-ionization (Alkhazov *et al.*, 1991). The evaporation process is done in a hot cavity at a temperature of 2500 K, see figure 2.3(b). Mishin *et al.* (1993) altered the experimental setup of Alkhazov *et al.* (1991) and performed a three step photo-ionization process of silver atoms, see section 2.2. The wavelengths of the lasers are 328.1 nm, 546.6 nm and 510 nm.

Three step ionization can be used for selective ionization, after which laser isomer separation is possible (Fedoseyev *et al.*, 2000). Silver atoms with various mass numbers can be created by this means with the intention of γ-ray decay investigation (Fedoseyev *et al.*, 2000). The silver ions generated by the three step photo-ionization are extracted by means of the extracting electrodes. According to Mishin *et al.* (1993), the strong thermionic emission inside the tube forms a negative charge well. This prevents the positively charged ions from striking the wall and returning to atom state.

2.1.5 Gas aggregation technique

Jackschath *et al.* (1992) used the gas aggregation technique to produce silver clusters for subsequent ionization by electron impact. Silver was vapourized in an argon atmosphere by heating a crucible, see figure 2.4(a). According to Schulze *et al.* (1984), the

cooling of the silver atoms would allow for the growth of embryonic particles. Their sizes would subsequently increase, primarily due to the absorption of atoms. According to Jackschath *et al.* (1992), cluster growth occurs due to homogeneous nucleation, which requires supersaturation. Supersaturation occurs when the partial pressure of the specie, i.e. the pressure of the gas which will condense, is higher than the saturation vapour pressure (Borra, 2006). Borra (2006) stated that above the critical cluster diameter, growth of the nuclei becomes favourable and irreversible.

After nucleation, the argon and silver mixture of the experimental setup is then transported through the aperture to the cryopump where almost all the argon is removed, see figure 2.4(a). The rotatable transparent target is kept at 4 K. According to Schulze *et al.* (1984), increasing the flow velocity increases the pressure, which in turn results in a drastic reduction of cluster size. A pressure profile along the system (in arbitrary units) is shown in figure 2.4(b).

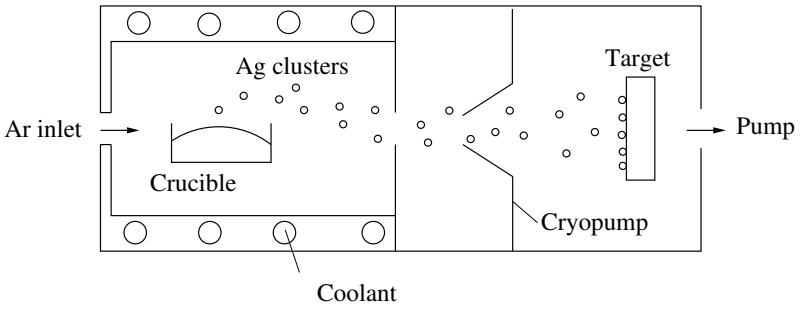

(a) The experimental setup as described by Schulze *et al.* (1984)

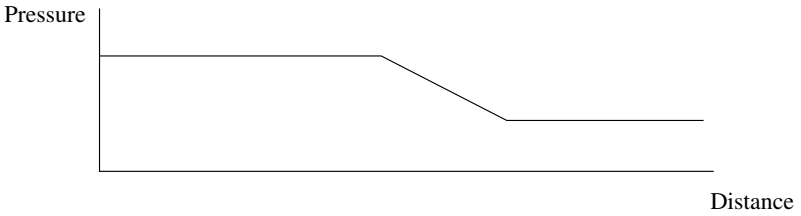

(b) Pressure profile

Figure 2.4: Gas aggregation technique (Schulze *et al.*, 1984)

Jackschath *et al.* (1992) made minor alterations to the technique employed by Schulze *et al.* (1984) to create clusters of up to 36 atoms for subsequent ionization by electron impact. Jackschath *et al.* (1992) concluded that increasing the cluster size decreases the energy required to ionize the particles.

2.2 Ionization

In the investigation of existing ion sources no ion source was found which can be used in helium at a pressure of 90 bar. Therefore, it was neccessary to investigate various means of ionizing atoms.

When the kinetic energy of an electron is higher than the ionization potential of the gas atom it is about to hit, the probability exists that ionization will take place (Llewellyn-Jones, 1966). It is also possible for electrons to raise the gas atoms' energy to a metastable state and then the atoms can be ionized by secondary electrons. Metastable states are excited atoms which are in a delicate state of equilibrium. Excited atoms are usually unstable and have relatively short life spans, in the region of 10^{-8} s. In comparison, metastable atoms have longer lifetimes, in the region of 10^{-1}s (Howatson, 1965). Due to the longer life span of the metastable atoms, they are easier to ionize by a secondary electron colliding with the metastable atom.

Other ionization processes include ion-atom collisions, atom-atom collisions, Penning ionization and photo-ionization (Llewellyn-Jones, 1966). Ion-atom collision is the transfer of a charge from the ion to the atom. Atom-atom collisions might create ionized particles if their relative velocities exceed twice their ionization velocity. When a metastable atom is struck by an atom and the energy of the metastable atom is more than the ionization energy of the atom, the atom can be ionized and the metastable atom returns to ground state. This is referred to as Penning ionization.

Photo-ionization has been successfully achieved under high pressures. Treschhalov *et al.* (1997) created a plasma in helium of 9 bar with photons of less energy than the ionizational potential of helium. This is possible due to multi-photon ionization, according to Gold and Bedd (1965). The three step ionization of silver and multi-resonance photo-ionization mentioned in section 2.1.4 is an example of this. The total number of ionizations due to multi-photon ionization is proportional to the atom concentration, the duration of the laser pulse and the volume of the focused zone (Ostrovskaya and Zaĭdel', 1973).

Recombination is when electrons or negative ions are captured by positive ions to form neutral atoms. With the return to neutral state the same deflection methods cannot be used on the particles. During this process the electron loses kinetic energy, which can be emitted as photons or transferred to third bodies (Llewellyn-Jones, 1966). The probability of recombination is increased with raised gas pressure (Howatson, 1965).

2.3 Gas discharge

A plasma is defined as a gas containing positive and negative particles but having no net charge (Howatson, 1965). It can be created by applying a voltage greater than the breakdown voltage of the gas between two electrodes (Scütze *et al.*, 1998), which Howatson (1965) calls as a gas discharge.

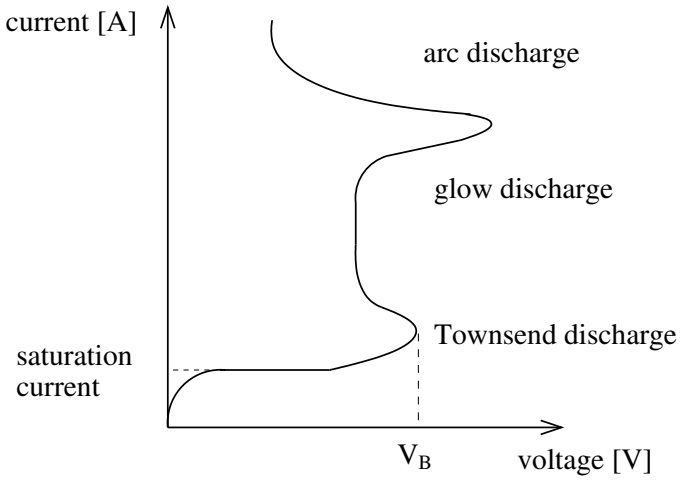

Figure 2.5: Types of gas discharges (Howatson, 1965)

According to Howatson (1965), discharges can be divided into three categories: Townsend discharge, glow discharge and arc discharge, see figure 2.5. At low electric fields a saturation current of 10^{-9} A flows between two electrodes due to positive and negative ions, which are formed by ultraviolet light, cosmic radiation and X-rays (Howatson, 1965). Increasing the voltage produces a Townsend discharge which carries current between 10^{-9} and 10^{-6} A. The Townsend discharge is formed by electrons, which are accelerated from the cathode to the anode, and these electrons ionize atoms during their course of travel (Howatson, 1965). Howatson (1965) stated that the number of electrons N_e crossing a plane at distance x from the cathode can be written as

$$N_e = N_0 e^{\alpha x} \tag{2.1}$$

where N_0 is the number of electrons leaving the cathode per second and α is Townsend's first ionization coefficient, which is defined as the number of ionizing collisions made by an electron travelling in an electric field. Howatson (1965) altered equation (2.1) to incorporate the secondary emission of electrons due to the bombardment of positive

ions, which produces the Townsend criterion

$$\gamma e^{\alpha d_{es}} = \gamma + 1 \tag{2.2}$$

where γ is the secondary electron emission coefficient and d_{es} is the distance between the two electrodes. The Townsend criterion requires that each primary electron produces at least one secondary electron which continues the process (Howatson, 1965). As the discharge does not require external radiation for ionization (Howatson, 1965), the discharge is self-sustaining.

Paschen conducted experiments and found that the breakdown potential of gasses are a function of pd_{es}, which is known as Paschen's law (Llewellyn-Jones, 1966). Using the same technique as employed by Scütze *et al.* (1998), see appendix A.6, Paschen's law for the breakdown voltage V_B of helium can be expressed as

$$V_B = \frac{pd_{es}B^2}{\left(\ln\left(pd_{es}A\right) - \ln\left[\ln\left(1+\frac{1}{\gamma}\right)\right]\right)^2} \tag{2.3}$$

According to Bondeson *et al.* (2002) the constants A and B are 8 and 16, respectively for helium.

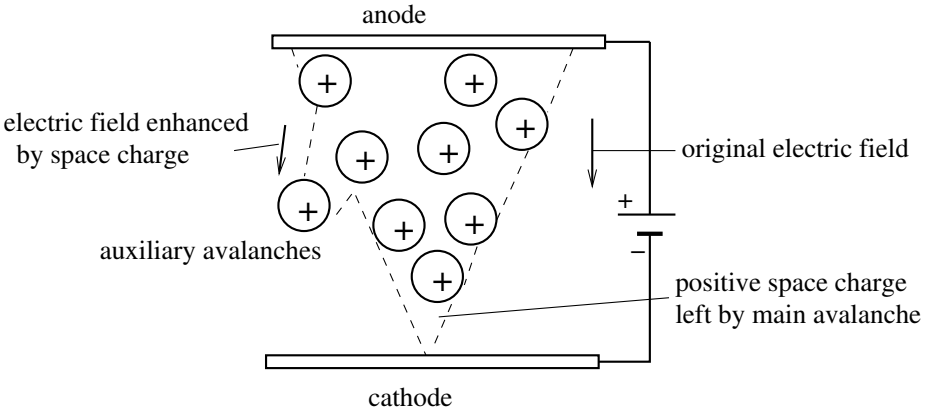

Figure 2.6: Formation of a streamer

Howatson (1965) stated that at very high values of pd_{es}, the Townsend criterion is not obeyed and hence Paschen's law is no longer valid. The streamer theory (Howatson, 1965) has been proposed as an alternative explanation for breakdown at high pressures. A streamer is the narrow luminous track occuring at the breakdown of a gas (Llewellyn-Jones, 1966), which starts at the anode and stretches towards the cathode (Howatson, 1965). Streamers are initiated by electrons which are accelerated from the

cathode to the anode, ionizing gas atoms in their path. As the positive gas atoms at the anode create a positive space charge, the strengthened electric field (which tapers towards the cathode) produces auxiliary avalanches. These avalanches are created by photo-ionization. When a streamer reaches the cathode secondary electrons are emitted due to positive ions bombarding the cathode.

According to Howatson (1965), at high pressure the voltage breakdown of the gas depends very little on the cathode material, which implies that the secondary electron emission coefficient is superfluous. Increasing $pd_{es} > 10\,000$ Torr cm (Llewellyn-Jones, 1966) slows the rate of the increase of voltage breakdown.

2.4 Laser ablation

Miller and Haglund (1998) state that laser ablation (LA) is a high yield photon sputtering process. Sputtering is the name given to beam induced ejection of particles from a surface. According to Kántor (2001), it is mostly used as a sample introduction method for MS or atomic emission spectrometry. However, according to Miller and Haglund (1998), it has various other uses such as microfabrication, colour printing and miscellaneous uses in the semiconductor industry.

The incident light from a laser is absorbed by the electrons, which are bound to the atoms in the sample. In the case of metals, the electron-lattice interactions are provided through thermal conductivity. This is the driving energy for nuclear motion which results in the ejection of atoms, ions and molecules from the surface, according to Miller (1994). In addition to this sputtering, a thermal wave propagates through the material surrounding the affected area. This, according to Miller and Haglund (1998), forms a corona.

The evaporated material expands and a plasma forms as a result of the high temperature (Bogaerts and Chen, 2005). The temperature drops during plume expansion, which is due to the transfer of energy from the more energetic metal atoms to the less energetic gas atoms through collision. These metal atoms undergo condensation, resulting in nanometer sized particles (Bogaerts and Chen, 2005).

A threshold value exists at which the LA process starts. Hence below threshold fluence F_{th}, no evaporation will occur. The equation is given by (Cabalín and Laserna, 1998)

$$F_{th} = \rho L_v \sqrt{a t_e} \tag{2.4}$$

where a is the thermal diffusitivity, L_v is the latent heat of evaporation and t_e is the laser pulse width. Cabalín and Laserna (1998) calculated a value for silver (at atmospheric pressures) to be 2.3 J/cm and compared it to tested values.

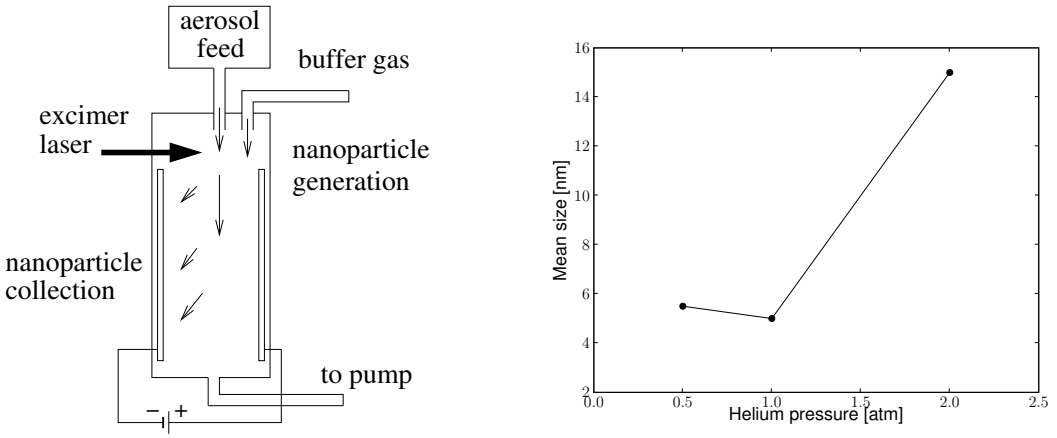

(a) Experimental setup of Nichols *et al.* (2000)

(b) Mean pariticle size vs pressure with a laser fluence of 2.4 J/cm^2 (Nichols *et al.*, 2000)

Figure 2.7: Nichols *et al.* (2000)'s experiment

Silver nanoparticles were produced by the process of laser ablation of microparticles (LAM) by Nichols *et al.* (2000). The aerosol feed of silver micorparticles and gas enter a chamber filled with a buffer gas, see figure 2.7(a). The gas and the buffer gas can be either helium, nitrogen or argon. A KrF excimer laser is used to ablate the microparticles, which forms nanoparticles. The nanoparticles are subsequently charged by photoelectric and thermal effects. After charging, the particles plated onto the electrodes. According to Nichols *et al.* (2000), the size distribution of nanoparticles which plate onto the carbon-coated electrodes varied due to the mobility of the particles. It was found that the size of the particles will vary with a variation in pressure, see figure 2.7(b).

2.5 Electrostatics of particles

This section investigates the electrostatics of particles. Possible means by which silver particles could receive a charge and the charge distribution within the particles will be discussed. Additionally, possible effects, such as the deflection and plate-out of the charged particles, will also be examined.

2.5.1 Contact charging of particles

Taylor and Secker (1994) state that when two different but electrically neutral materials come into contact with each other, charge will be transferred in order to bring the contacting materials into thermodynamic equilibrium. The charge will remain if they are separated quickly enough and the two materials remain isolated from earth.

According to the Sommerfeld's free electron theory, an electron energy occupied at 0 K at the highest quantum state is named Fermi energy E_f (Dekker, 1967). In order for electrons to be removed from the metal surface, the electron energy inside the metal has to be raised to the vacuum level. In the free electron model this represents the surface of the metal under vacuum conditions. The amount of energy between Fermi energy level and vacuum level is referred to as the work function ϕ and varies for different metals, see figure 2.8(a). The force that keeps the electrons at bay is called the image force, which can be explained by the polarized metal exerting an attractive force on the electron.

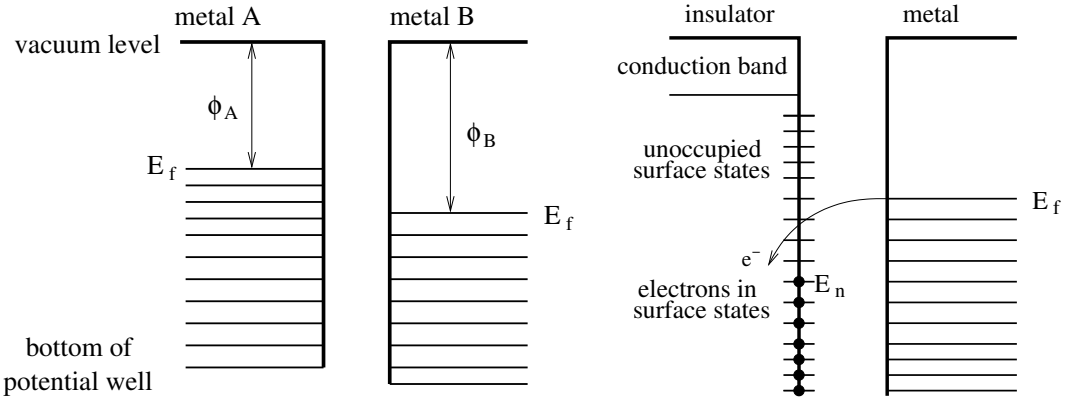

Figure 2.8: Contact charging (Taylor and Secker, 1994)

The charge transfer is explained by considering two metals (A and B) with metal A having a lower work function than metal B, $\phi_A < \phi_B$. When the two metals make contact, electrons in higher energy states in metal A transfer into lower energy levels in metal B by means of a tunneling mechanism (Taylor and Secker, 1994). This charge transfer only ceases when the Fermi level of metal A is the same as that of metal B. This leaves metal A slightly positively charged and metal B slightly negatively charged.

There are a number of theories concerning the charge transfer between semiconductors and conductors. According to Taylor and Secker (1994), one of these theories postulate

the existence of a surface state, see figure 2.8(b). These states may be extrinsic or intrinsic (Taylor and Secker, 1994). In the case of semiconductors, an intrinsic semiconductor is a single-crystal material, while an extrinsic semiconductor has impurities in the material (Neaman, 2001). All surface states below neutral energy level E_n are occupied by electrons while those above this level are empty (Taylor and Secker, 1994), see figure 2.8(b). If the electrons in the metal have more energy than the ones in the surface state of the insulator, then electrons move from the metal to the insulator until both of their energy levels are at equilibrium.

2.5.2 Charging by induction

When a particle with a low resisitivity ($\leq 10^8$ Ωm) moves between two electrodes, the charge within the particle is redistributed, see figure 2.9(a). This occurs in order to maintain a constant potential throughout the particle's volume (Taylor and Secker, 1994). The particle is then said to be polarized.

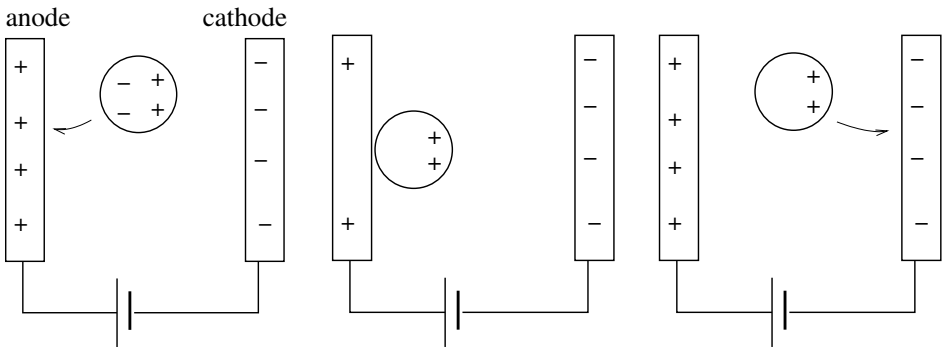

(a) Polarization of a particle in an electric field

(b) Charge transfer at the anode

(c) Charged particle moving towards cathode

Figure 2.9: The three stages of induction charging (Taylor and Secker, 1994)

If the polarized particle comes into contact with the anode, charge leaks from the particle to the electrode, see figure 2.9(b). This charge transfer continues until the charge of the particle is in equilibruim with that of the anode. The particle is left with excess positive charge. When this positive particle breaks away from the anode it accelerates towards the cathode, see figure 2.9(c). When the particle reaches the cathode, the cathode's negative charge is transfered to the particle until the charge in the particle is in equilibrium with that of the cathode. After breaking away, the particle is accelerated towards the anode. This process of movement between the two electrodes is repeated continuously (Taylor and Secker, 1994).

2.5.3 Dielectrophoresis

Kang *et al.* (2006) stated that the particle trajectory of polystyrene microparticles in liquid can be controlled by the use of dielectrophoresis (DEP). Therefore, DEP was investigated as a means of deflecting silver particles in a nonhomogeneous electric field.

As stated in the previous section, when a particle with low resistivity moves between two plates the particle is polarized. DEP is a phenomenon where a resultant force is created by a nonhomogeneous electric field acting on a particle with a dipole moment m. The dipole moment is created by a polarized particle in an electric field, see section 2.5.4 for more information.

Consider a polarized particle in a nonhomogeneous electric field, see figure 2.10(a). Performing a summation of the vector forces produces a resultant force, see figure 2.10(b)

$$\mathbf{F}_{DEP} = q\mathbf{E}(\mathbf{r}+\delta) - q\mathbf{E}(\mathbf{r}) \tag{2.5}$$

where q is the charge, $\mathbf{r}$ is the position of the particle in the electric field and δ is the distance between the positive and negative sides of the particle. Expanding $\mathbf{E}(\mathbf{r}+\delta)$ with the Taylor series, ignoring the second and higher order terms, leads to

$$\mathbf{E}(\mathbf{r}+\delta) = \mathbf{E}(\mathbf{r}) + \delta \cdot \nabla\mathbf{E}(\mathbf{r}) + ... \tag{2.6}$$

Replacing $\mathbf{E}(\mathbf{r}+\delta)$ in equation (2.5) with equation (2.6) results in

$$\mathbf{F}_{DEP} = q\delta \cdot \nabla\mathbf{E} \tag{2.7}$$

where $q\delta$ is the dipole moment which can be replaced by m, as it was created by the electric field, see section 2.5.4. Replacing $q\delta$ with m leads to the dielectrophoretic ap-

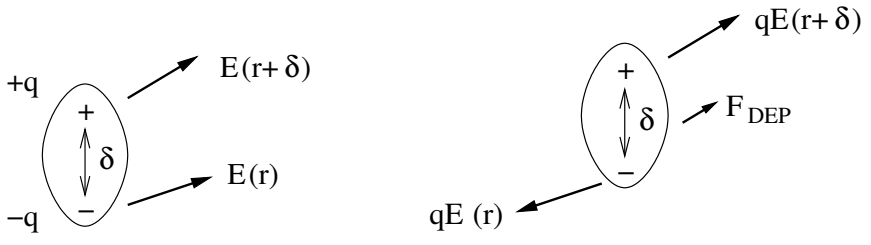

(a) The dipole moment created in a particle

(b) Forces acting on a particle with a dipole moment

Figure 2.10: Dipole moment in a nonhomogeneous electric field (Jones, 1995)

proximation (Jones, 1995),

$$\mathbf{F}_{DEP} = \mathbf{m} \cdot \nabla \mathbf{E} \tag{2.8}$$

The effective induced dipole moment for a spherical particle, see appendix A.3 for the derivation thereof, can be expressed as

$$\mathbf{m}_{ef} = 4\pi\varepsilon_{He} K_{CM} R^3 \mathbf{E} \tag{2.9}$$

where R is the radius of the particle, ε_{He} is the permittivity of the medium (which was taken as helium). The Clausius-Mossotti function (Jones, 1995) is

$$K_{CM} = \frac{\sigma_{Ag} - \sigma_{He}}{\sigma_{Ag} + 2\sigma_{He}} \tag{2.10}$$

where σ_{Ag} and σ_{He} are the conductivity of silver and helium, respectively. $\sigma_{Ag}/\sigma_{He} \rightarrow \infty$ due to the fact that $\sigma_{Ag} \gg \sigma_{He}$, which results in a K_{CM} equalling 1.

An investigation of the DEP force on a spherical silver particle is analysed in section 5.1. According to Jones (1995), dielectrophoresis is only applicable to particles in the range of 1 μm to 1 mm in diameter. The upper limit is imposed as it is based upon the definition of a particle. The lower limit is due to the strong influence of van der Waals forces and Brownian motion. However, as the polarizibility describes the response of the electron cloud in a particle to an electric field (Lide, 1996), particles smaller than 1 μm can still be polarized.

2.5.4 Atomic and molecular polarizabilities

As stated in the previous section, atoms and molecules, which are smaller tha 1 μm, can also be polarized. According to Hook and Hall (1996), the dipole moment of an isolated particle can be expressed as

$$\mathbf{m} = \alpha \mathbf{E} \tag{2.11}$$

where $\mathbf{E}$ is the electric field. According to Hook and Hall (1996), permanent electric dipole moments μ are due to molecules without centres of symmetry. As random thermal collisions increase with increase in temperature the tendency of the dipoles to line up with the electric field decreases, which decreases the influence of μ. This influence

can be seen in the total polarizability equation (Moore, 1957)

$$\alpha = \alpha_{at} + \frac{\mu^2}{3k_B T} \tag{2.12}$$

Pereiro and Baldomir (2007) determined the mean static polarizibility per atom α_{at} and found that the permanent electric dipole moment is negligible for silver clusters of up to 23 atoms.

Lide (1996) stated that electric dipole polarizibility is constant for different electric fields. It is therefore concluded that if an atom is in a nonhomogeneous electric field, it would experience a force similar to that of dielectrophoresis. Further investigation into the force experienced by the atom due to the static polarizibility is shown in section 5.2.

2.5.5 Particle interactions

The interactions of the particles which were observed in the experiments, see chapters 4 and 6, are investigated in this section. Firstly, the agglomeration of particles is discussed, which is followed by an examination of the atomization of droplets and particle chain formation.

Particles in suspension in air are continuously engaged in random movement, which is referred to as Brownian motion. This motion causes collisions and the impaction of small sized particles which forms the agglomeration, according to Parker (2003). As particles agglomerate, their velocity decreases, which subsequently reduces the possibility of further collisions.

Taylor and Secker (1994) state that a charged droplet experiences an electrostatic pressure p_{ec}, which attempts to break up the particle, while the forces keeping it together are surface tension. If the force due to p_{ec} is larger than the surface tension force, the droplet will be atomized.

The applied electric field induces dipoles in particles, which creates mutual electrostatic forces, which can be attractive or repulsive. Figure 2.11(a) shows how particles which are aligned parallel to the electric field are attracting each other, which creates particle chains. Figure 2.11(b) shows repulsion forces due to particles aligned perpendicular to an electric field. Based on the balance between electrostatic and thermal

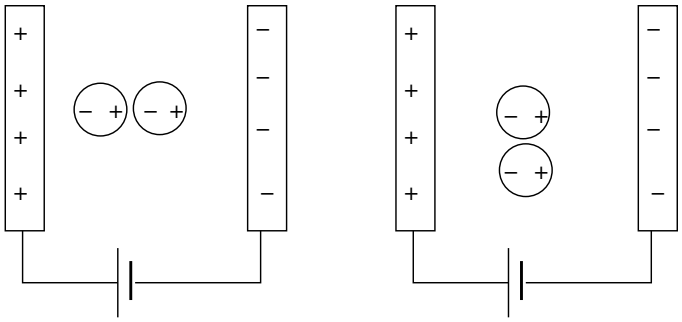

(a) Particles aligned parallel to the electric field

(b) Particles aligned perpendicular to the electric field

Figure 2.11: Attraction and repulsion force due to particles being aligned parallel or perpendicular to the electric field (Jones, 1995)

energy, a threshold electric field was determined (Jones, 1995)

$$E_{th} = \frac{1.7R^{-\frac{3}{2}}}{K_{CM}}\sqrt{\frac{k_B T}{\varepsilon_{He}}} \tag{2.13}$$

As particle chains which are formed in this way increase in length, the effective dipole moment m_{ef} is increased. A normalized moment per particle m_{ef}/N is considered, where N is the number of particles, which also increases as N increases (Jones, 1995). It is therefore concluded that particle chains increased the dielectrophoretic force acting on the particle.

2.5.6 Electrostatic contribution to adhesion

According to Jones (1995), the adhesion of particles to a surface is influenced by short-range van der Waals forces, surface tension (if moisture is present), mechanical deformation of the particle and the surface and electrostatic forces. Jones (1995) also states that the electrostatic force can be represented by three components for a non-conductive surface: an image, coulomb (which is repulsive) and dielectrophoresis force. In the case of a conducting particle lying on top of the conductive surface, the particle experiences a lifting force F_{lift}, see figure 2.12. This lifting force is the summation of the attractive image force, which is the first term in equation (2.14), and the repulsive coulomb force, which is the second term of

$$F_{lift} = 4\pi\varepsilon_{He}R^2\mathbf{E}^2\left(-\zeta(2)+\zeta(3)+\frac{1}{6}\right)+\frac{\pi^2}{6}4\pi\varepsilon_{He}R^2\mathbf{E}^2 \tag{2.14}$$

where ζ is the Riemann-zeta function (Jones, 1995). The repulsive coulomb force is due to a Maxwell charge which is induced within the particle (Jones, 1995).

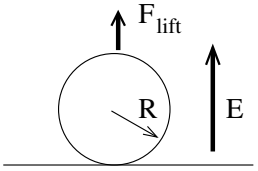

Figure 2.12: The the electostatic lifting force (Jones, 1995)

Peréz (2002) completed a generalised study on the electric force experienced by a conducting sphere close to a plane electrode which is subject to an external electric field. He concluded that when this sphere comes close enough to the electrode a discharge will occur between the electrode and sphere due to an increased electric field strength at the electrode. The sphere must remain in equipotential with the electrode and hence the amount of charge is (Peréz, 2002)

$$Q = \frac{\pi^2}{6}\varepsilon_{He}R^2\mathbf{E} \tag{2.15}$$

The well-known Lennard Jones potential represents the intermolecular potential between molecules (McQuirrie and Simon, 1997). According to McQuirrie and Simon (1997) the r^{-6} term accounts for the attraction potential between the particles at large distances. In the case of the two molecules having dipoles, or induced dipoles, this term is influenced by the dipole moment and the polarizibility of the particle (McQuirrie and Simon, 1997).

2.5.7 Electrostatic precipitators

Electrostatic precipitators (ESP) are used to remove dust particles from a flowing stream of gas by means of an electrostatic force. The sizes of these particles range from 0.01 to 100 μm, according to Parker (2003).

A high voltage is applied to the discharge electrode, see figure 2.13, which causes a corona discharge. A corona discharge is defined as a self-sustaining discharge in which the field-intensified ionization is localized over a portion of the distance between the electrodes (Devins *et al.*, 1963). The produced ions then attach themselves to passing dust particles by means of field and diffusion charging, whereafter the particles migrate to the collection electrode and subsequently plate-out on the surface of the

collection electrode. A mechanical hammer is used to remove the particles when the collected particles' level reaches a predetermined value. This process is termed rapping (Mizuno, 2000). The particles fall into a hopper and are then removed.

The localized field-intensified ionization of a corona discharge is created by one electrode with a radius of a much smaller curvature than the other electrode (Devins *et al.*, 1963), which creates a nonhomogeneous electric field.

There are two types of corona discharges, namely positive and negative. In the latter corona, the electrode with a small radius is negative. Electrons move away from the cathode while ionizing particles in their path, see figure 2.13. These positive ions, as well as photons, will strike the cathode and emit secondary electrons. The slow moving electrons will be captured by electro-negative oxygen molecules, according to Devins *et al.* (1963). The build up of the negative space charge around the discharge electrode will decrease the electric field and cause the discharge to extinguish itself (Devins *et al.*, 1963). This entire process is repeated as long as a voltage is applied (Devins *et al.*, 1963).

In the positive corona, a positive space charge is formed around the anode, according to Chang *et al.* (1991). When the ion density is large enough a positive streamer is formed. This propagation of ions is due to photo-ionization. These streamers which are formed have a much greater active volume, or ionization zone, that the space charge of the negative corona (Chang *et al.*, 1991). Mizuno (2000) states that the negative corona's flashover voltage, i.e. the breakdown voltage between the two electrodes, is higher than that of a positive corona, which leads to a larger margin of applied voltage.

When charged particles come into contact with the collection electrode, they are held to the plate by van der Waals and electrical attraction forces, according to Parker (2003). After contact the charge leaks to ground and the particles are only held to the plate by van der Waals forces, see section 2.5.2. After reaching the collection plate, the electrical and van der Waals forces act not only between the particles and the plates, but also between the various particles. According to Parker (2003), due to the cohesion of particles, particles of greater than 500 μm can be formed by agglomeration.

Collection efficiency is affected by various factors, one being dust resistivity ρ. According to Mizuno (2000), when $\rho < 10^2$ Ωm abnormal re-entrainment occurs. This phenomenon is the re-entry of collected dust into the electrode spacing, see figure 2.13. The positively charged particles which leave the surface regain their negative charge when they re-enter the ionization zone. Mizuno (2000) also stated that the collection efficiency of submicroparticles is low. According to Masuda *et al.* (2006) aggregated particles become re-entrained when the maximum bending stress which the particle

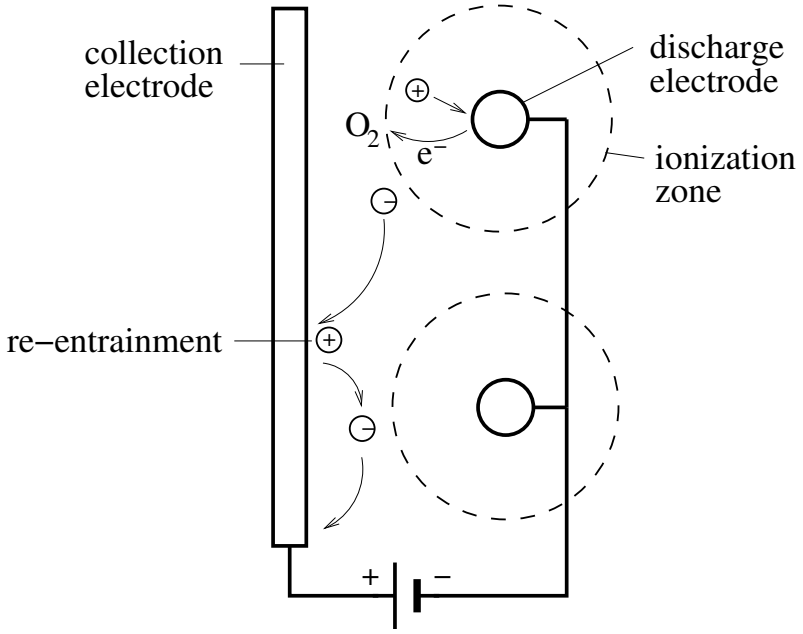

Figure 2.13: Schematic diagram of an electrostatic precipitator (Mizuno, 2000)

experiences is 3 times the wall shear stress (creep flow is assumed). The bending stress is due to the moment M_o, which the particle experiences due to drag on the particle.

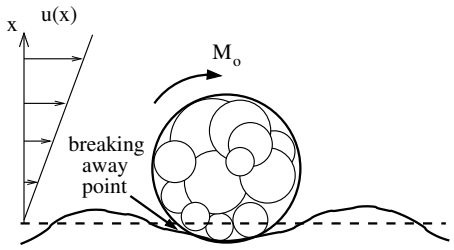

Figure 2.14: Re-entrainment of an aggregated particle (Masuda *et al.*, 2006)

To reduce re-entrainment, adhesive agents can be added to the surface of the collecting electrode. Another possibility is the use of a wet ESP, or alternatively, the collecting electrode can be brushed (Mizuno, 2000).

2.5.8 Field and diffusion charging

As stated in the previous section, particles in electrostatic precipitators are charged by field and/or diffusion charging. The equations explained in this section are used in section 6.3 to calculate the maximum charge on the silver particles.

In field charging the ions are transported along the electric field lines and subsequently attach themselves to a particle. Field charging is relevant to particles > 2 μm (Mizuno, 2000). The Pauthenier limit is the maximum charge on a spherical particle and can be expressed as (Taylor and Secker, 1994)

$$q_{field} = 4\pi\varepsilon_0 R \frac{3\varepsilon}{\varepsilon + 2} E \tag{2.16}$$

where ε_0 and ε are the vacuum and the particle permittivity, while R is the radius of the particle and E is the electric field.

In diffusion charging the thermal energy of the ions is large, which implies that Brownian motion is also large. With this increased Brownian motion, the velocity is large enough to overcome the Coulomb repulsive force between the particle and ion. Further charging of the particle occurs (Taylor and Secker, 1994) until

$$q_{dif} = 6\pi\varepsilon_0 R \frac{k_B T}{e} \tag{2.17}$$

where k_B is Boltzmann's constant, T is the absolute temperature and e is the electron charge.

2.6 Conclusion

From the literature study presented in this chapter, the conclusion was drawn that no ion sources exists which can be used with helium pressure of 90 bar. Electrostatic precipitation is a technique used to remove particles in an atmospheric pressure gas stream, but requires charged particles to attach themselves to the particles which are to be deflected. The assumption has been made that only helium and silver are present in the helium stream and therefore electrostatic precipitation is not a viable solution as no oxygen is present. However, laser ablation of microparticles (LAM) provides a possible means of creating charged nanoparticles for subsequent deflection in an electric field. Dielectrophoresis (DEP) is a possible means of deflecting uncharged particles. LAM and DEP are the two processes which are to be investigated in detail in the following chapters as a means of scrubbing the helium of silver.

Chapter 3

Electron generation theories

As stated in the previous chapter, no ion sources were found that can be used with helium at a pressure of 90 bar, hence alternative customised methods of ionizing particles were investigated. This chapter describes the generation of electrons that can be used to ionize the silver in a secondary process. Three means of generating electrons are considered: thermionic emission, field emission and photoelectric emission.

The three methods of electron generation are based upon raising the electron energy or decreasing the work function. As previously stated in section 2.5.1 the work function ϕ is the amount of energy needed by an electron before it is able to escape from a metal. After the electrons are released from the metals they would then ionize the silver particles in the helium flight path as a secondary process. It is therefore important for the emitted electrons to have sufficient energy to ionize the silver particles.

3.1 Thermionic emission

Thermionic emission is the increase of electron energy in metals under elevated temperatures, which subsequently releases electrons. This process, as well as the energy of the released electron from the metal surface (in this case tungsten was used), are considered.

Dekker (1967) concluded that after thermionic emission the total average energy of the escaping electrons is

$$\langle E_e \rangle = 2k_B T \tag{3.1}$$

with a Maxwellian velocity distribution perpendicular to the surface. Using equation (3.1) the total average velocity of the emitted electrons from a metal surface heated

to 3600 K was calculated as $2 \times 8.617 \times 10^{-5}$ J/K $\times$3600 K = 0.62 eV. The calculated value is far less than the ionization potential of silver, which is 7.54 eV. Increasing the temperature is not viable as 3 600 K is close to the melting point of tungsten.

As the total average electron energy is far less than that what is required to ionize silver it is concluded that thermionic emission would not be a viable means of producing electrons for this purpose. It might be possible to produce single electrons due to the Maxwellian distribution, but the slower moving electrons would recombine with the silver ions. The recombining of the ions with the electons would render the ions ineffective for the purpose of deflection.

3.2 Field and cold emission

When an electric field is applied accross two electrodes it is possible that electrons may be emitted from the surface of the cathode (Howatson, 1965). This process is better known as field emission. The lowering of the effective work function by an external electric field E, which would allow emission of electrons, is known as the Schottky effect (Howatson, 1965) and can be seen as $\Delta\phi$ in figure 3.1.

The potential energy of an electron is zero when it is far away from the uncharged metal surface (Dekker, 1967). The metal becomes polarized as the electron approaches the surface and the electron experiences an attractive force, also known as the image force. The potential energy of the electron due to the image force can be expressed as (Dekker, 1967)

$$E_{im} = -\frac{e^2}{4x} \tag{3.2}$$

where e is the electron charge and x is the distance from the metal surface (Dekker, 1967). The potential energy of the electron in the space between the electrodes, due to the external electric field, can be expressed as

$$E_{elec} = -eEx \tag{3.3}$$

Adding equations (3.2) and (3.3) results in an equation for the total potential energy of the electron

$$E_e = -eEx - \frac{e^2}{4x} \tag{3.4}$$

The Fermi energy level E_f, as well as the work function ϕ of tungsten is shown in figure 3.1. To determine the maximum change in the work function $\Delta\phi_{max}$, the derivative of

equation (3.4) is set equal to zero. This results in

$$\Delta\phi = -e(eE)^{\frac{1}{2}} \tag{3.5}$$

An applied electric field of 10^3 V/cm results in a $\Delta\phi \simeq 0.01$ eV according to Llewellyn-

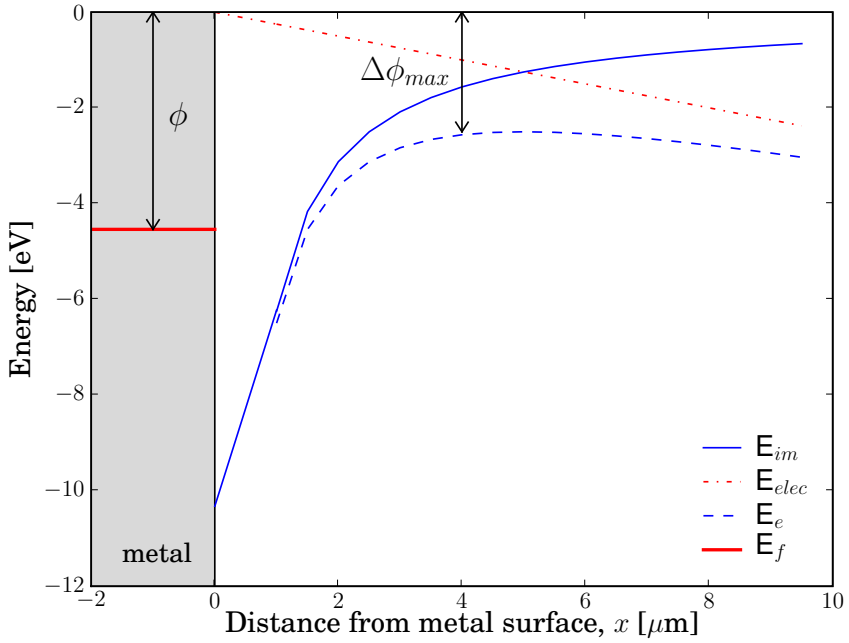

Figure 3.1: The Schottky effect

Jones (1966). This value is too small to affect the outcome of field emission as the work functions of most metals range between 4 and 5 eV. When the applied electric field is in excess of 10^6 V/cm cold emission occurs. In cold emission electrons tunnel through the potential barrier. The reason for this tunnelling can be explained in terms of quantum mechanics, according to Howatson (1965). If the electric field of 10^6 V/cm is applied to the electrodes a discharge between the two electrodes would occur as the voltage breakdown for helium is 4.398×10^3 V/cm (see table A.2). It is therefore concluded that field emission would not raise the electron energy enough by itself to ionize silver.

3.3 Photoelectric emission

Photoelectric emission can be described as the process whereby photons impinging on a metal surface raise the Fermi energy level sufficiently to emit electrons from

the surface. According to Howatson (1965), incoming photons with energies greater than threshold frequency $f_{th} = e\phi/\hbar$ will emit electrons from metals as raising the frequency would raise the energy of the emitted electrons. F_2 lasers provides the highest level of energy per quanta for commercially obtainable equipment. The F_2 laser produces photons with a wavelength of 157 nm and energy of 7.9 eV. This energy is sufficient to emit electrons from most metals and ionize silver atoms, but does not emit electrons with sufficient energy to ionize silver in a secondary process.

3.4 Electron emission in helium

The three previous sections describe electron sources that can produce electrons in a vacuum but not in helium under high pressure. Hirsch (2005) worked with low gas pressure and concluded that the gas molecules will penetrate the electrodes. These gas molecules, as well as those just outside the electron emitter, will become polarized. This will subsequently affect the emission, due to the change in the configuration of the lattice of the metal. The value of the reflection coefficient depends on the height and the shape of the potential barrier, see section 3.2, at the surface. The polarized gas molecules affect both of these factors. Hirsch (2005) concluded that this will have a small effect on pure metals. He formulated that $\Delta\phi = -ln(\zeta)k_BT/e$ where ζ is the current ratio. Tests were done by Hirsch (2005) at pressures up to 8×10^{-4} mbar and $\Delta\phi$ was found to be up to 0.15 eV for helium. For values greater than 2×10^{-4} mbar, the increase in $\Delta\phi$ appears to remain constant (Hirsch, 2005). The small variation in ϕ would only slightly influence the current emitted under vacuum conditions.

3.5 Conclusion

From the calculations done in the four sections mentioned above it is concluded that thermionic, field and photoelectric emission cannot be used to create electrons with sufficient energy to ionize silver in a helium environment.

The use of an F_2 laser to photo-ionize silver is possible, see section 3.3. Multiphoto-ionization is also a possible means of ionizing silver, see section 2.2. Nichols *et al.* (2000) successfully used laser ablation of microparticles (LAM) to produce silver nanoparticles in helium and plated them onto an electrode. LAM was investigated and an experiment based on this method is proposed in the next chapter.

Chapter 4

Microparticle tests

In the two previous chapters laser ablation of microparticles (LAM) was proposed as a means of creating and deflecting nanoparticles, as electrons could not be generated with sufficient energy to ionize silver in a helium stream. Two sets of experiments were conducted to determine the deflection of silver particles in an electric field. The first set of experiments are described in this chapter. These experiments involved the deflection of industrially produced silver microparticles manufactured by Inframat Advanced Materials (Inframat Advaced Materials, 2002) in helium. The first set of experiments is based on the results obtained by Nichols *et al.* (2000), see section 2.4. In the second set of experiments, see chapter 6, the silver particles were created by an arc discharge and deflected by dielectrophoresis and electrostatic forces.

4.1 Filter insertion test results

Figure 4.1 is a photograph of the test vessel used in the experiments. This test vessel's cut out view is displayed in figure 4.2(a) while a schematic of the flow paths is displayed in figure 4.2(b). The helium flow path, which starts at the helium tank, passes through the system and exits at point 2. The system is designed to create a plasma in helium with the use of a laser. This plasma atomizes and ionizes silver when it enters the plasma whereafter it is deflected towards the cathode.

From figures 4.2(a) and 4.2(b) it is evident that helium has two flow paths, primary and secondary. The secondary flow path channels helium through a filter arrangement whereby silver microparticles can be introduced into the primary flow path. The primaty flow path starts at 1 and ends at 2 and these two points are indicated in figure

Figure 4.1: The test vessel on its stand next to the helium tank

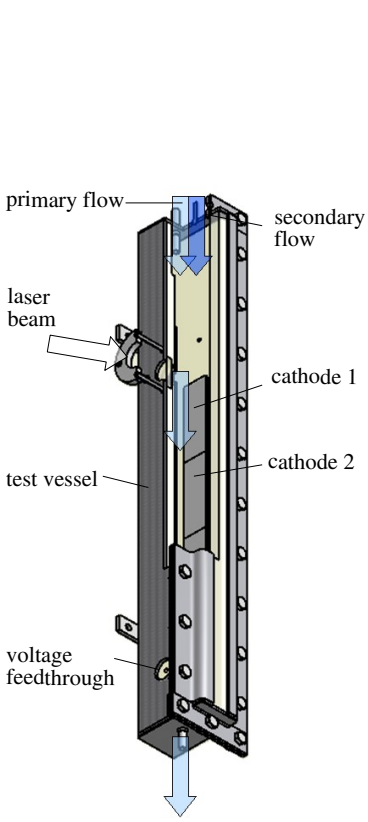

(a) A cutout view of the test vessel

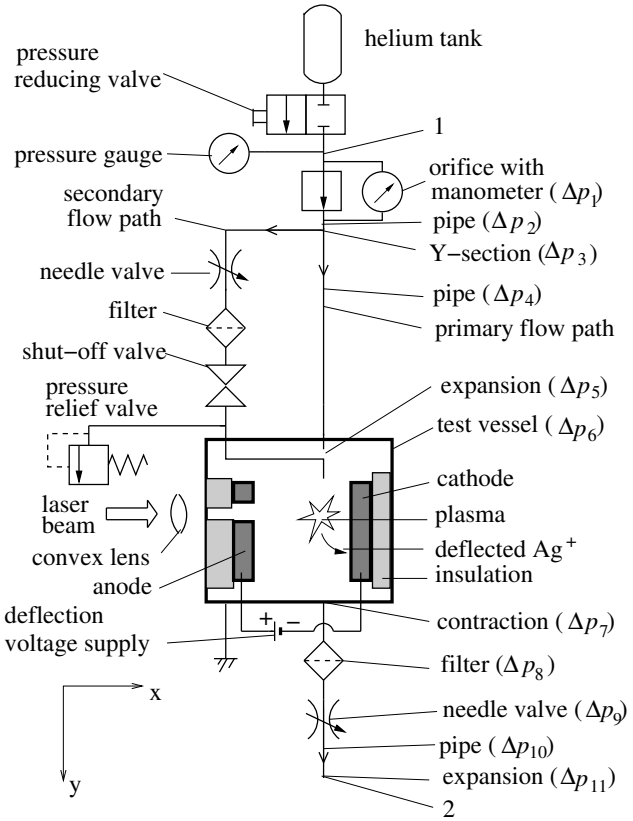

(b) A schematic of the flow paths

Figure 4.2: Microparticle test apparatus setup

4.2(b). The elements in the primary flow path were used to determine the mass flow rate of the system, which is displayed in appendix B.1. The near-spherical silver particles are in powder form with diameters between 5-7 μm, with 99.95% purity. The silver microparticles were inserted between the filter and the shut-off valve in the secondary flow path. The converged laser light would be used to create a plasma. When the silver microparticles enter the plasma of ionized helium, they are then ionized. The ionized silver particles are then attracted towards the cathode and plate-out on its surface.

Both electrodes have a length of 228 mm and consist of three separate elements, each with a length of 76 mm. The anode's elements are named anode 1 to anode 3 and similarly, the cathode's elements are named cathode 1 to cathode 3. Each element consists of a glass microscope slide covered with heavy weight aluminum foil. A high voltage supply, ORTEC model 456 serial number 3153, was connected to the electrodes by two feedthroughs, which allows the chamber to remain under pressure and the vessel to be grounded.

The gap between the cathode and the anode is 25 mm. A value of 2.5 kV was the maximum voltage applied over the two electrodes. The voltage breakdown of 9.033 kV was calculated for the the 25 mm electrode spacing, see table A.2. Using 2.5 kV provides a safety factor of 3.6, which was calculated by 9.033 kV/2.5 kV = 3.6.

In the primary flow path the mass flow rate of the helium was determined by means of a calibrated orifice, as explained in appendix B.1. The 1 and 2 marked in figure 4.2(b) represents the start and the end of the primary flow path. Each element marked with Δp in brackets was used in the mass flow rate calculations. The filter at the end of the primary flow path prevented the use of high mass flow rates and a value of 3.884x10^{-5} kg/s was obtained from calculations, see appendix B.1.

The efficacy of the insertion mechanism of the filter insertion test was evaluated by doing experiments without the use of the XeCl laser. This was neccesary as the use of the laser is expensive and time consuming. Therefore, it is advisable to sort out any problems with the appartus before using the laser. The XeCl was proposed as the Physics Department of the University of Stellenbosch does not have a F_2 laser, see section 2.1.4. Each removable electrode element was individually weighed using a Precisa 40S-200A scale before and after the experiment to obtain the amount of silver which plated out onto each removable element. The results of filter insertion test are shown in table 4.1. The second column of this table is the amount inserted into the system. The cathode and anode columns are the amounts collected on these electrodes. The following two columns are the percentage collected on the cathode and anode. Acc is the total amount accounted for as a percentage of the amount inserted, i.e. Acc

is the summation of amounts collected on the anode, cathode and filter divided by the amount inserted.

Table 4.1: Filter insertion test results

test no	inserted [g]	anode [g]	cathode [g]	anode %	cathode %	Acc %
1	0.0818	0.0000	0.0007	0.0	0.9	18.5
2	1.1094	0.0007	0.0006	0.1	0.1	2.8
3	1.1167	0.0008	0.0020	0.1	0.2	32.6
4	0.0109	-0.0002	0.0007	-1.8	6.4	95.4
5	0.1042	0.0006	0.0021	0.6	2.0	30.3

It is clear from table 4.1 that only a low percentage of the total amount of silver inserted was accounted for. This is due to the silver microparticles plating out on the shut-off valve and piping of the system. An alternative method was thus required for more accurate results and a mixing chamber was devised.

4.2 Mixing chamber test

The use of a mixing chamber was postulated as a potential solution to the problem stated in the previous section. However, to implement this solution several alterations to the microparticle test apparatus were necessary. The secondary flow, see figure 4.3, now passes through the mixing chamber. The entry hole in the mixing chamber has a smaller diameter than the pipe which forces the helium to flow at a faster rate. The higher velocity and the angle of entry of the helium allows it to pick up silver particles and deposit them into the primary flow path. The directing pipe directs the flow of the secondary flow path into the centre of the primary flow path. An additional alteration was made: the orifice with the manometer was placed at the exit, as this would ensure that water could not enter the system if the helium flow rate was in excess of that which the manometer could measure.

The results of the mixing chamber test are displayed in table 4.2. Th test cloumn is the test number while the voltage column is the voltage applied over the anode and cathode. The inserted column of this table is the amount of silver inserted into the system. The cathode and anode columns are the amounts collected on the these electrodes. The following two columns are the percentage collected on the cathode and anode, respectively. This percentage was calculated by dividing the cathode and anode columns by the amount accounted for. Acc is the total amount accounted for as a percentage

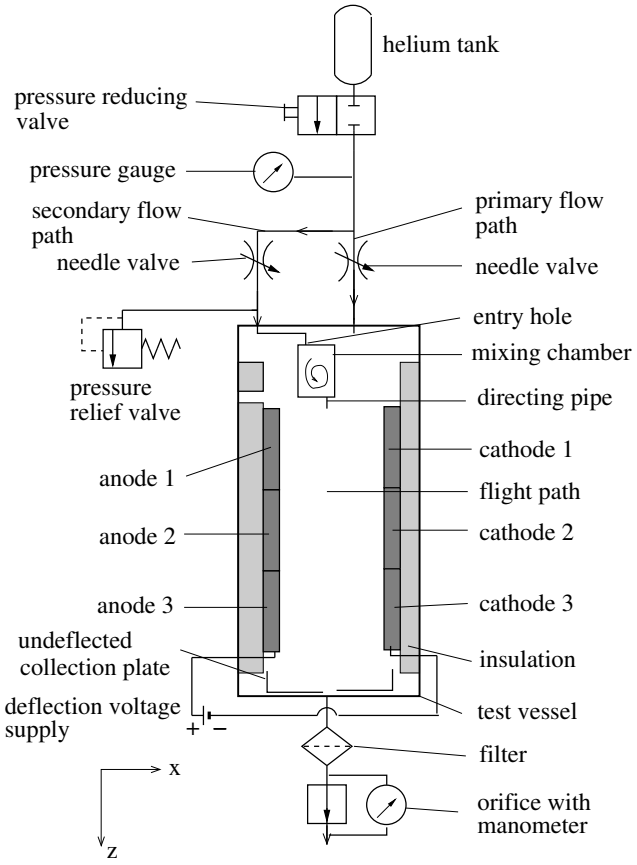

Figure 4.3: The mixing chamber setup

of the amount inserted, i.e. Acc is the summation of amounts collected on the anode, cathode, undeflected collecting plate and filter divided by the amount inserted. It was found that some of silver microparticles accumulated around the directing pipe as the seal between directing pipe and the mixing chamber did not seal properly. Some of the silver also fell to the undeflected collection plate during setup, before the needle valves were opened to begin the test. This loss of silver was due to the tightening of the bolts which held the cover plate to the test vessel. The velocity column is the helium flow rate, while the remaining columns are the amounts which plated out on each element of the two electrodes.

Table 4.2: Deflection of microparticles with mixing chamber test

test	voltage [V]	inserted [mg]	anode [mg]	cathode [mg]	anode %	cathode %	Acc for %	Velocity [mm/s]	anode 1 [mg]	anode 2 [mg]	anode 3 [mg]	cathode 1 [mg]	cathode 2 [mg]	cathode 3 [mg]
1	500	8.7	-0.2	1.5	-2.3	17.4	98.9	48.145	0.0	0.2	-0.4	0.7	0.4	0.4
2	2500	16.4	0.7	1.3	5.5	10.2	78.0	26.854	0.2	0.5	0.0	0.4	0.3	0.6
3	1000	106.7	-0.2	1.2	-0.2	1.3	88.4	39.310	0.0	-0.2	0.0	0.6	0.2	0.4
4	1000	143.9	0.4	4.3	0.3	3.4	88.7	20.300	0.1	0.0	0.3	1.9	2.0	0.4
5	1000	86.4	1.3	3.6	2.0	5.5	76.4	26.854	0.3	0.4	0.6	2.0	1.0	0.6
6	1000	19.3	1.1	0.8	6.5	4.7	87.6	22.696	0.4	0.2	0.5	0.5	0.1	0.2
7	1000	20.4	0.4	1.2	2.4	7.2	81.9	40.600	0.1	0.0	0.3	0.6	0.3	0.3
8	0	325.6	0.6	9.4	0.2	3.5	81.6	0.000	0.4	0.4	-0.2	1.9	7.0	0.5
9	0	2.4	0.1	0.6	4.5	27.3	91.7	21.531	-0.1	0.1	0.1	0.0	0.4	0.2
10	0	22.1	0.1	0.0	0.6	0.0	77.8	25.375	0.1	0.0	0.0	0.2	0.0	-0.2
11	0	10.4	0.3	-0.2	5.7	-3.8	51.0	24.862	0.2	0.1	0.0	0.0	-0.1	-0.1
12	0	73.1	0.4	0.5	0.6	0.7	94.7	40.600	0.1	0.3	0.0	0.1	0.2	0.2
13	0	92.6	0.4	0.4	0.5	0.5	84.8	38.650	0.2	0.0	0.2	0.2	0.0	0.2
14	0	23.2	0.4	0.2	2.2	1.1	78.4	35.885	0.2	0.1	0.1	0.2	0.0	0.0
15	2000	16.1	0.7	0.6	6.4	5.5	67.7	47.607	0.2	0.2	0.3	0.3	0.1	0.2
16	2000	10.7	0.3	0.6	6.7	13.3	42.1	33.663	-0.1	0.1	0.3	0.3	0.3	0.0
17	2000	54.7	0.7	1.4	1.7	3.3	77.3	34.420	0.1	0.0	0.6	0.8	0.1	0.5
18	2000	44.0	0.8	0.6	2.3	1.7	80.0	32.889	0.7	0.0	0.1	0.0	0.3	0.3
19	2000	10.8	0.5	0.6	5.9	7.1	78.7	35.885	0.3	-0.1	0.3	0.0	0.1	0.5
20	2000	12.6	0.2	1.0	2.0	9.9	80.2	35.160	0.2	-0.2	0.2	0.4	0.3	0.3
21	2000	16.2	0.4	0.9	3.3	7.3	75.9	38.650	0.2	0.1	0.1	0.0	0.6	0.3
22	2000	59.3	0.8	0.9	1.7	1.9	79.3	38.650	0.2	0.3	0.3	0.3	0.3	0.3
23	1000	9.1	0.6	0.0	16.7	0.0	39.6	32.889	0.2	0.2	0.2	0.0	0.0	0.0
24	1000	45.6	0.5	0.0	1.7	0.0	65.1	32.097	0.1	0.2	0.2	0.0	0.0	0.0
25	1000	106.9	0.7	0.0	0.7	0.0	88.3	38.650	0.2	0.2	0.3	0.0	0.0	0.0
26	1000	295.1	1.4	0.0	0.6	0.0	81.1	37.293	0.4	0.5	0.5	0.0	0.0	0.0
27	1000	42.8	1.0	0.0	3.4	0.0	69.4	31.284	-0.2	0.9	0.3	0.0	0.0	0.0
28	1000	6.8	0.6	0.0	9.5	0.0	92.6	31.284	0.2	0.3	0.1	0.0	0.0	0.0
29	1000	139.3	0.0	1.0	0.0	0.8	87.6	30.450	0.0	0.0	0.0	0.4	0.3	0.3
30	1000	245.2	0.0	0.9	0.0	0.4	92.4	26.854	0.0	0.0	0.0	0.2	0.4	0.3
31	1000	15.5	0.0	0.6	0.0	4.9	78.7	29.592	0.0	0.0	0.0	0.6	0.3	-0.3
32	0	5.8	0.1	0.2	3.1	6.2	55.2	0.000	0.0	0.2	-0.1	0.3	-0.2	0.1
33	0	4.1	0.1	0.0	3.3	0.0	73.2	0.000	0.2	-0.2	0.1	0.2	-0.3	0.1
34	0	19.7	-0.4	0.2	-2.2	1.1	91.4	0.000	0.0	-0.1	-0.3	0.0	0.0	0.2
35	0	14.9	-0.4	-0.1	-3.2	-0.8	83.2	0.000	-0.1	0.0	-0.3	0.1	0.0	-0.2
36	0	18.3	0.1	-0.3	0.6	-1.9	84.7	0.000	0.4	-0.1	-0.2	0.1	-0.2	-0.2
37	0	17.0	0.6	-0.6	4.3	-4.3	82.4	0.000	0.3	0.2	0.1	-0.2	-0.2	-0.2

Statistical methods were applied to the results of table 4.2 in order to determine the presence, or absence, of any meaningful trends. The sample mean $\overline{x}$ and sample standard deviation S_x were calculated by use of the following equations (Figliola and Beasley, 2000).

$$\overline{x} = \frac{1}{N}\sum_{i=1}^{N} x_i \tag{4.1}$$

$$S_x^2 = \frac{1}{N-1}\sum_{i=1}^{N}(x_i - \overline{x})^2 \tag{4.2}$$

The voltage column of table 4.3 is the applied voltage between the anode and cathode, while the N column represents the number of tests completed. The anode and cathode columns are the percentage of weight deposited on each element. The pretest check is utilised in an attempt to quantify the amount of silver which falls to the bottom and the sides of the test vessel during setup. Hence, the pretest column is the amount of silver which never had the opportunity to deflect during the tests. It was decided to implement a lower limit on the tests due to microparticles falling to the bottom of the test vessel before the test is initiated. Every test needed more than 10 mg inserted to meet the criteria of a successful test and to qualify for use in the results calculations.

Table 4.3: Sample mean and standard deviation of the mixing chamber test

Voltage kV	N	Acc %	anode %	cathode %	pretest [g]
Pretest check					
0	6	78.33 ± 12.76	0.99 ± 3.13	0.06 ± 3.55	13.30 ± 29.89
Homogeous field					
0	6	78.05 ± 14.61	1.63 ± 2.10	0.35 ± 2.37	
1	5	84.59 ± 5.37	2.19 ± 2.65	4.40 ± 2.23	
2	8	72.64 ± 13.00	3.73 ± 2.21	6.26 ± 4.03	
Nonhomogeous field					
1	4	75.98 ± 10.63	1.59 ± 1.28	-	
1	3	86.22 ± 6.93	-	2.05 ± 2.50	

It is evident from table 4.3 that a very small percentage of sliver plates out onto the collecting electrodes. Increasing the voltage from 1 kV to 2 kV increases the percentage of microparticles collected on the anode and cathode by 1.4 and 1.7 times, respectively. Additionally, there appears to be a tendency for the particles to adhere to the aluminum cathode rather than the aluminium anode. In the case of a homogeneous field the tendency to adhere to the cathode is calculated by dividing the percentage collected

on the cathode by the percentage collected on the anode, $\frac{4.4\%}{2.19\%} = 2$ and $\frac{6.26\%}{3.73\%} = 1.67$, while in the case of a nonhomogeneous field this decreases to $\frac{2.05\%}{1.59\%} = 1.3$. The sample mean for each element (under the influence of a homogeneous electric field), which is shown in table 4.4, does not indicate an increase in tendency in the amount detected per electrode element.

Table 4.4: The sample mean of each element of the mixing chamber test

voltage	anode 1	anode 2	anode 3	cathode 1	cathode 2	cathode 3
0 V	0.20	0.16	0.02	0.52	1.44	0.14
1kV	0.18	0.08	0.34	1.12	0.72	0.38
2kV	0.28	0.12	0.28	0.28	0.28	0.32

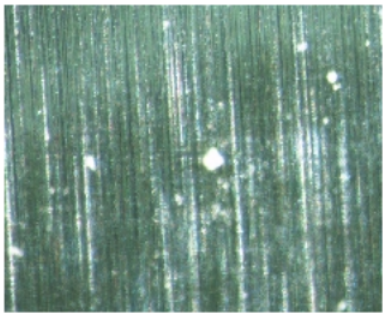

Figure 4.4: Agglomeration of particles seen on cathode 2 of test 9

An agglomeration of particles was observed, see section 2.5.5, which can be seen on cathode 2 of test 9 in figure 4.4. The vertical stripes are indentations in the aluminium foil which are due to the foil manufacturing process. When applying a high potential over these particles, they are atomized, see section 2.5.5. This can be seen on the cathode and anode of test 2 in figures 4.5 and 4.6. These two figures illustrate that the same number of particles collect on the cathode as well as the anode.

Under further investigation of the deposited particles, particle chains (see section 2.5.5) were found. This is, however, difficult to display as the chain is formed in the direction it is viewed from, hence only the top part of the chain can be seen. Changing the focus of the microscope makes these chains visible, see figure 4.7. The chain formation which was detected on the electrodes is supported by the theoretical model (see section 2.5.5). If equation (2.13) is used with a particle with a radius of 3 μm, temperature of 293.15 K and K_{CM} of 1 ($1.7(3 \times 10^{-6})^{-\frac{3}{2}}\sqrt{1.38 \times 10^{-23} \times 293.15/1.000065 \times 8.854 \times 10^{-12}}$), a value of 6.995 kV/m is calculated for the electric field threshold, which would allow chain formation, see section 2.5.5. This value is less than the 40 kV/m that was typically applied during tests, hence chain formation is supported by theory.

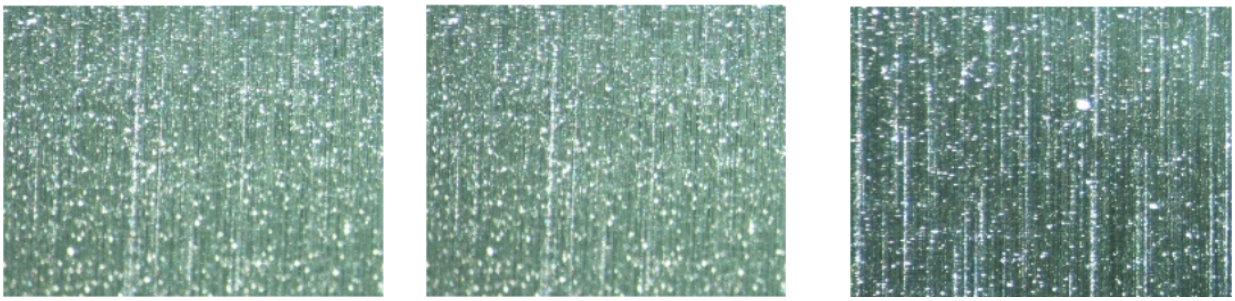

(a) cathode 1 (b) cathode 2 (c) cathode 3

Figure 4.5: Silver microparticles that atomized in an electric field and plated out on the cathode

(a) anode 1 (b) anode 2 (c) anode 3

Figure 4.6: Silver microparticles that atomized in an electric field and plated out on the anode

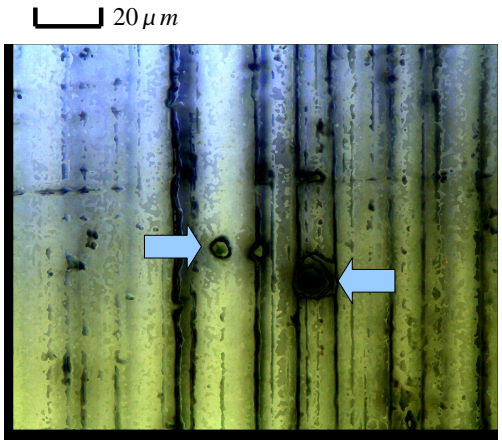

Figure 4.7: Various microscope images taken at different focal heights from the surface of a particle, which have been overlapped to create a 3D image

4.3 Conclusion

Laser ablation of microparticle (LAM) would charge particles in the plasma and which would then readily be deflected in an electric field. It was unclear whether these charged particles would not just return to uncharged state, but Nichols *et al.* (2000) suggest that this does not occur. A laser was never used as problems were encountered with the filter insertion techniques and deflection was effected without the use of a laser.

It was found that that the insertion mechanism (in the filter insertion test) does not operate as desired. Therefore a mixing chamber test was devised. In this test it was found that the microparticles plated out on both the positive and negative electrodes of the mixing chamber test. The probability of the presence of both positively and negatively charged particles in the apparatus is small, though not impossible. Bipolar charging of particles are possible as the work functions of aluminium and copper used in the mixing chamber would allow for positive and negative contact charge of silver particles (see section 2.5.1). A more viable explanation for particles deflecting to both sides is that a dielectrophoretic force is present.

From the experiments and the calculations (which are shown in section 5.1) it was found that the apparatus used in this chapter was not long enough to successfully deflect all the microparticles by means of dielectrophoresis. Decreasing the velocity would not be a viable solution as the values seen in table 4.2 are already far less than the desired 120 m/s. Alterations to the apparatus were thus needed, which are described in chapter 6, to obtain measurable results.

Chapter 5

Deflection models

This chapter is used to describe two different deflection models for the deflection of silver particles in a flowing stream of helium. The first model is a deterministic deflection model, which is governed by the equations of state, coulombic and dielectrophoretic forces. This deflection model describes the deflection of the microparticles in the two experiments, see chapters 4 and 6, by use of a continuum of fluid dynamics.

The second deflection model (a stochastic model) is governed by the probability of collisions and the forces are created due to the electrostatic potential of an ion and the polarizability of atoms. This deflection model describes the motion of single atoms or clusters as they collide with helium atoms.

5.1 Deterministic deflection model

Dielectrophoresis can be used to seperate silver particles from helium in a nonhomogeneous electric field. This seperation is accomplished because there is a difference in permittivity, conductivity and size between the silver and the helium, see section 2.5.3. The deterministic deflection model is based on principles used by Kadaksham *et al.* (2006) and is compared with the experimental results in chapters 4 and 6.

Figure 5.1(a) displays the coordinate system used in the simulations and the experiment. The direction in which the helium stream flows is y, the electrodes are oriented along the z-axis and the distance between the two electrodes is given by X. The 25 mm wide flat plate type electrode and 5 wide mm flat plate type electrode are displayed in this figure.

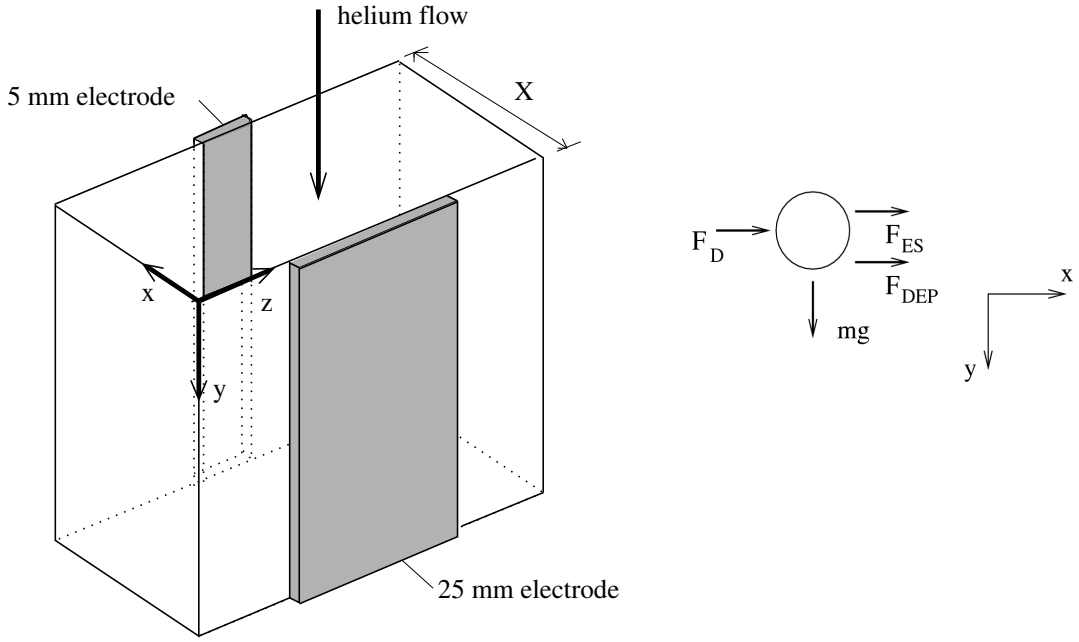

(a) The coordinate system (b) The free body force diagram

Figure 5.1: The coordinate system and the free body force diagram used in the experiments and the simulations

Consider the sum of the applied forces $\mathbf{F}_{app}$ of the free body force diagram shown in figure 5.1(b)

$$\mathbf{F}_{app} = \mathbf{F}_g + \mathbf{F}_{DEP} + \mathbf{F}_{ES} + \mathbf{F}_D \tag{5.1}$$

where $\mathbf{F}_g$ is the gravitational force, $\mathbf{E}_{DEP}$ is the dielectrophoretic force, $\mathbf{F}_{ES}$ is the electrostatic or coulombic force and $\mathbf{F}_D$ is the drag force. The coulombic force can be expressed as (Taylor and Secker, 1994)

$$\mathbf{F}_{ES} = q\mathbf{E} \tag{5.2}$$

In the case of the Reynolds number ($Re = \rho \mathbf{v}_{rel} d_p / \mu$) of the particle being less than 0.5, Stokes' law for the drag force on a sphere is applicable (Crowe *et al.*, 2001)

$$\mathbf{F}_D = \frac{6\pi\mu R\mathbf{v}_{rel}}{C_m} \tag{5.3}$$

where $\mathbf{v}_{rel}$ is the particle's velocity relative to the helium's velocity. When the Knudsen number $\lambda/2R$ tends to zero, the helium in which the particle is immersed is no longer continuous and must be treated as consisting of discrete particles. Due to this phenomonen Stokes' law needs to be corrected by the Cunningham correction factor

(Parker, 2003)

$$C_m = 1 + 1.246\frac{\lambda}{R} + 0.42\frac{\lambda}{R}\exp\left(\frac{-0.87R}{\lambda}\right) \tag{5.4}$$

To be able to calculate the dielectrophoretic force F_{DEP} in equation (5.1) the electric field in the space between the two electrodes must be calculated. A $x-z$ plane (see figure 5.1) of the experiment is discretized into N_x x-elements and N_z z-elements. As the length in the y direction is quite long in relation to the width, the variation in the dielectrophoretic force in the y-direction would be small. The same assumption was made by Chen *et al.* (2005). The electric potential ϕ of each discretized control volume was determined by applying the Laplace equation (Chen *et al.*, 2005)

$$\frac{\partial^2\phi}{\partial x^2} + \frac{\partial^2\phi}{\partial z^2} = 0 \tag{5.5}$$

To solve this equation the central differential approximation proposed by Lindfield and Penny (2000) was used.

$$\nabla\phi_i = \frac{-\phi_l + \phi_r}{2l} \tag{5.6}$$

$$\nabla^2\phi_i = \frac{\phi_l - 2\phi_i + \phi_r}{l^2} + \frac{\phi_a - 2\phi_i + \phi_b}{H^2} \tag{5.7}$$

The subscripts are explained in figure 5.2. The electric potentials V_A and V_C, see figure

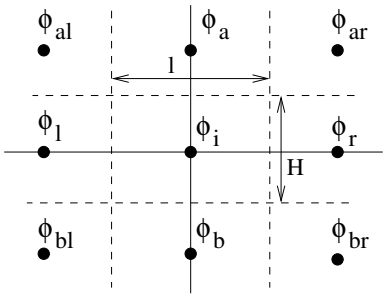

Figure 5.2: The subscripts (Lindfield and Penny, 2000)

5.3(a), have specific electric values ($\phi = V_C$ and $\phi = V_A$). Applying these Dirichlet boundary conditions, ϕ_i may be solved. For other boundaries, which were insulated, the Neumann boundary values are used, $\frac{\partial\phi}{\partial x} = 0$ or $\frac{\partial\phi}{\partial z} = 0$.

If an electric potential of 500 V applied to the two electrodes, V_A is 500 V and V_C is 0 V. If the potential is -500 V, V_A is 0 V and V_C is 500 V.

As the assumption is made that the electric field remains constant along the y-axis,

$\nabla \mathbf{E}^2$ is calculated by (Chen *et al.*, 2005)

$$\nabla \mathbf{E}^2 = \frac{\partial}{\partial x} E^2 \mathbf{i} + \frac{\partial}{\partial z} E^2 \mathbf{k} \tag{5.8}$$

$$= 2(E_x E_{xx} + E_y E_{yx})\mathbf{i} + 2(E_x E_{xy} + E_y E_{yy})\mathbf{k} \tag{5.9}$$

where $\mathbf{i}$ and $\mathbf{k}$ are unit vectors in the x and z directions respectively,

$$E_x = -\frac{\partial \phi}{\partial x}, \qquad E_z = -\frac{\partial \phi}{\partial z}, \qquad E_{xx} = \frac{\partial E_x}{\partial x},$$
$$E_{zz} = \frac{\partial E_z}{\partial z}, \qquad E_{xz} = \frac{\partial E_x}{\partial z}, \qquad E_{zx} = \frac{\partial E_z}{\partial x}$$

E_{xz} was approximated as by (Lindfield and Penny, 2000)

$$E_{xz} = \frac{\phi_{ar} - \phi_{al} - \phi_{br} + \phi_{bl}}{4Hl} \tag{5.10}$$

Equations (5.9) and (2.9) were inserted into equation (2.8) to produce the components of the dielectrophoretic force experienced by the silver particle, which varies per control volume, as

$$F_{DEP,x} = 4\pi\varepsilon_{He} K_{CM} R^3 \left(E_x E_{xx} + E_z E_{zx}\right) \tag{5.11}$$

$$F_{DEP,z} = 4\pi\varepsilon_{He} K_{CM} R^3 \left(E_x E_{xz} + E_z E_{zz}\right) \tag{5.12}$$

where $F_{DEP,x}$ and $F_{DEP,z}$ are the x and z components of the dielectrophoretic force. Note that $\mathbf{E} \cdot \nabla \mathbf{E} = \frac{1}{2}\nabla |\mathbf{E}^2|$ (Kang *et al.*, 2006) and hence the $\frac{1}{2}$ and the 2 in equation (5.9) cancel each other out. The dielectrophoretic force field of a silver nanoparticle

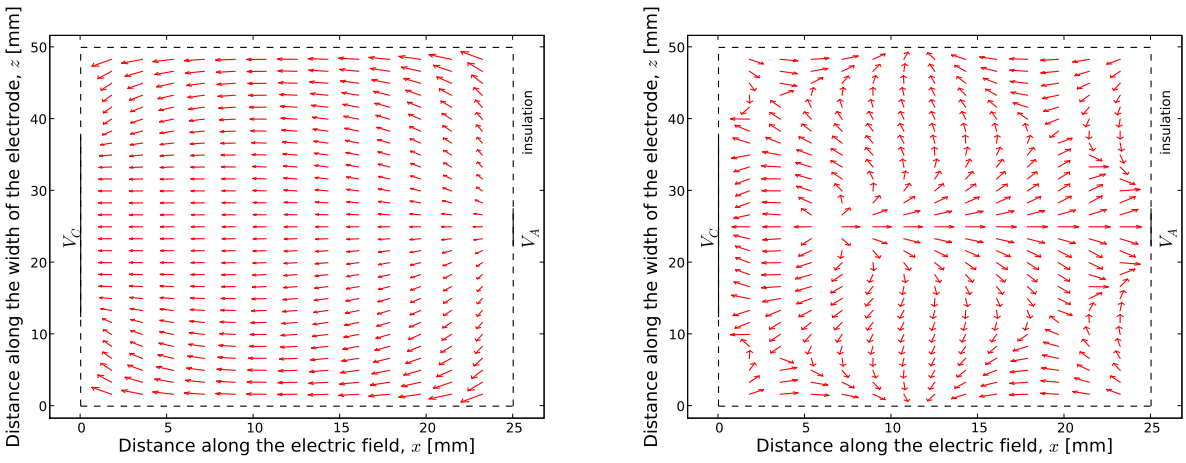

(a) The electric field

(b) The dielectrophoretic force field

Figure 5.3: Application of 500 V to the electrodes

with a radius of 10 nm under the influence of an electric potential of 500 V is plotted in figure 5.3(b). Note how the force field is a mirror image around the centre of the two electrodes, which is to be expected as the boundaries are mirror images. It is also seen that if the force field remains the same whether the applied voltage is positive or negative.

Increasing the number of control volumes does not influence the dielectrophoretic force, as can be seen in table 5.1. The N_x and N_z columns represent the number of x and z control volumes, while the remaining columns represent the dielectrophoretic force in the x-direction at the various x intervals. The z coordinate remains constant at 25 mm

Table 5.1: Comparing the dielectrophoretic force by varying the number of control volumes

N_x	N_z	$F_{DEP,x}$ at x = 5 mm [N]	$F_{DEP,x}$ at x = 10 mm [N]	$F_{DEP,x}$ at x = 15 mm [N]	$F_{DEP,x}$ at x = 20 mm [N]
31	31	-0.038133$\times 10^{-24}$	0.320000$\times 10^{-24}$	1.619563$\times 10^{-24}$	10.130922$\times 10^{-24}$
61	61	-0.070429$\times 10^{-24}$	0.312551$\times 10^{-24}$	1.652474$\times 10^{-24}$	9.387216$\times 10^{-24}$
121	121	-0.045458$\times 10^{-24}$	0.325802 $\times 10^{-24}$	1.657495 $\times 10^{-24}$	9.824418$\times 10^{-24}$
241	241	-0.034580$\times 10^{-24}$	0.330927$\times 10^{-24}$	1.657794$\times 10^{-24}$	10.053642$\times 10^{-24}$

The acceleration of the particles can be determined by means of the Langevin equation (Kadaksham *et al.*, 2004).

$$m_{Ag}\frac{d\mathbf{v}_p}{dt} = \mathbf{F}_{app} \tag{5.13}$$

where m_{Ag} is the mass of the silver particle.

Very small particles reach terminal velocity quite quickly. Kang *et al.* (2006) stated that if the characteristic time scale $m_p/6\pi\mu R$, where μ is the dynamic viscosity, is in order of magnitude smaller than the time scale of the experimental observation, the above assumption is valid. The terminal velocity of micro and nanoparticles are investigated in appendix A.4. When the particle reaches terminal velocity it no longer accelerates because the drag force is the same as the external applied forces which leads to

$$v_y = v_{He} + \frac{m_p g C_m}{6\pi\mu R} \tag{5.14}$$

$$v_x = \frac{(F_{DEP,x} + F_{ES,x})C_m}{6\pi\mu R} \tag{5.15}$$

$$v_z = \frac{(F_{DEP,z} + F_{ES,z})C_m}{6\pi\mu R} \tag{5.16}$$

where v_{He} is the velocity of the helium, which is calculated by means of equation (A.24). $F_{ES,x}$ and $F_{ES,z}$ is the coulombic force in the x and z directions respectively while $F_{DEP,x}$ and $F_{DEP,z}$ are the dielectrophotetic forces in the x and z directions respectively.

The position $p^i_{(x,y,z)}$ at time step i for the particles is calculated by means of

$$p^i_{(x,y,z)} = p^{i-1}_{(x,y,z)} + \mathbf{v}^{i-1}\Delta t \tag{5.17}$$

where Δt was taken as 10^{-5} s and $\mathbf{v}^{i-1}$ is the velocity of the particle at the previous time step. 10^{-5} s was chosen as this value is less than the characteristic time scale $\frac{10490\text{kg/m}^3 \times \frac{4}{3}(10^{-6}\text{m})^3}{6\pi \times 19.93 \times 10^{-6}\text{kg/ms} \times 10^{-6}\text{m}} = 11.696\ \mu$s, but does not effect the time necessary to calculate the deflection path.

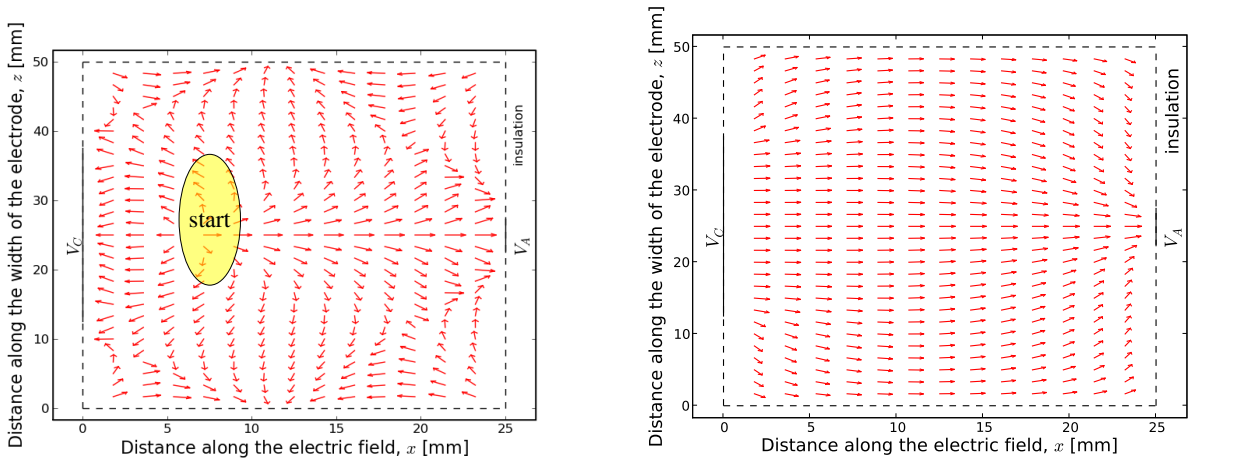

(a) The starting position of the silver particles

(b) The force field if the silver particles experiences a charge of one electron

Figure 5.4: The starting position of the silver particles and the force field acting on the charged silver particles

The silver particles were given random initial positions in the shaded region in figure 5.4(a) in the $x-z$ plane at y = 0. The random starting positions were generated using a normal distribution with $\overline{x}$ = 8 mm (σ = 2 mm) and $\overline{z}$ 12.5 (σ = 12.5 mm). These values were chosen as they correspond with the experimental starting positions of the particles, see chapter 6.

Figure 5.4(b) shows the combined coulombic and dielectrophoretic ($F_{app} = F_{DEP} - eE_x$) force field vectors that would act on a silver particle anywhere in the $x-z$ plane as a result of the nonhomogeneous electric field generated between the two electrodes. The silver particle has a radius of 10 nm and experiences an electric field due to an electric

potential of 500 V. Figure 5.3(b) displays F_{DEP} for the same conditions. The large difference in vector directions between the two figures are due to the eE_x component of the above mentioned equation (F_{DEP} = 4.448×10^{-25} N while F_{app} = 2.265×10^{-15} N). From figure 5.4(b) it is possible to see that negative charged particles will always move towards the anode as the force due to a single charge is a lot more than the dielectrophoretic force. It is therefore conluded that the coulombic force does not influence the particles deflection as they deflect to both electrodes.

To expedite comparsion to the first experimental setup the particle is considered to initiate at (x = 5 mm, y = 0 mm, z = 25 mm). Note that for the particle's radius of 3 μm the terminal velocity (or at least a value close to terminal velocity) is reached at a time of 3.158 ms, see section A.4. This is larger than the time step of 10 μs hence equations (5.14), (5.15) and (5.16) are no longer valid. The Langevin equation, equation (5.13), was used to determine the particle's velocity at each individual time step. If the applied voltage is 500 V and the helium bulk velocity is 0.0198 m/s, then after 4.6 s the silver particle's position changed from the initiated position to (x = 4.999995 mm, y = 140.000261 mm , z = 2.500000 mm). This indicated that the apparatus of helium flow path length 140 mm, as described in chapter 4, is not long enough to deflect the particles as the particle reached the end of the flight path without deflecting towards the cathode.

Sample calculations of these calculations are demonstrated in appendix D.1. From these calculations it was possible to see that dielectrophoresis would not be a suitable means of scrubbing microparticles as the dielectrophoretic force is smaller than the gravitational force.

5.2 Stochastic deflection model

The stochastic deflection model describes the movement of a single silver particle during time-based collisions with gas atoms. The stochastic deflection model described in this section is a two dimensional (2D) model based upon Cronje (2007)'s three dimensional (3D) model. In this model the collisions are assumed to be elastic, which implies that energy is only exchanged as translational kinetic energy (Howatson, 1965). This model is used to determine the deflection of an ion in a homogeneous electric field. This model is also used to determine the time it takes for a particle with a high initial velocity to be cooled down to ambient temperature and the deflection of an silver atom due to the polarization it experiences in a nonhomogeneous electric field.

It is well known that molecules in suspension are constantly in random motion as a result of collisions by molecules around it (Sears, 1964), called Brownian motion. In the time between these collisions the silver particle is accelerated due to an applied force $\mathbf{F}_{app}$, see section 5.1. In this section the applied force is

$$\mathbf{F}_{app} = \mathbf{F}_{ES} + \mathbf{F}_{DEP} \tag{5.18}$$

The differences between equations (5.1) and (5.18) are that gravity is ignored and the hydrodynamic drag force is incorporated into the random velocities of the helium atom in equation (5.18). The charge on the particle is considered to be that of one electron which is used in the coulombic force equation ($\mathbf{F}_{ES} = eE$) (Taylor and Secker, 1994).

As the stochastic deflection method is based upon collisions, it is necessary to acsertain the velocity of helium atoms to complete the momentum transfer calculations. The speed distribution of the particles can be expressed by the Maxwell-Botlzmans speed distribution (Sears, 1964)

$$f(v) = 4\pi \left(\frac{M}{2\pi RT}\right)^{\frac{3}{2}} v^2 \exp\left(\frac{-Mv^2}{2RT}\right) \tag{5.19}$$

where R is the universal gas constant and v is the speed of the particle. Cronje (2007) rewrote this distribution as a function of the most probable speed v_p of the particles by taking

$$v_p = \sqrt{\frac{2RT}{M}} \tag{5.20}$$

and inserting it into equation (5.19), which results in

$$f(v) = \frac{4}{\sqrt{\pi} v_p} \left(\frac{v}{v_p}\right)^2 \exp\left(-\left(\frac{v}{v_p}\right)^2\right) \tag{5.21}$$

Equation (5.21) and the cumulative distribution function, which is the numerical integration of equation (5.21), is shown in figure 5.5. Random numbers between 0 and 1 were generated and the corresponding value of the integrated equation was obtained with a search function. This value is then taken as the particle's velocity. In figure 5.5 an example is shown by taking 0.55 as the cumalitive distribution function, which provides 1220 m/s as the velocity of the helium. The direction in which it travels is taken randomly, $0 < \beta < 2\pi$. Therefore the helium's random velocity is known and the momentum during collisions can be calculated.

During a elastic collision momentum is only transferred along the line connecting the

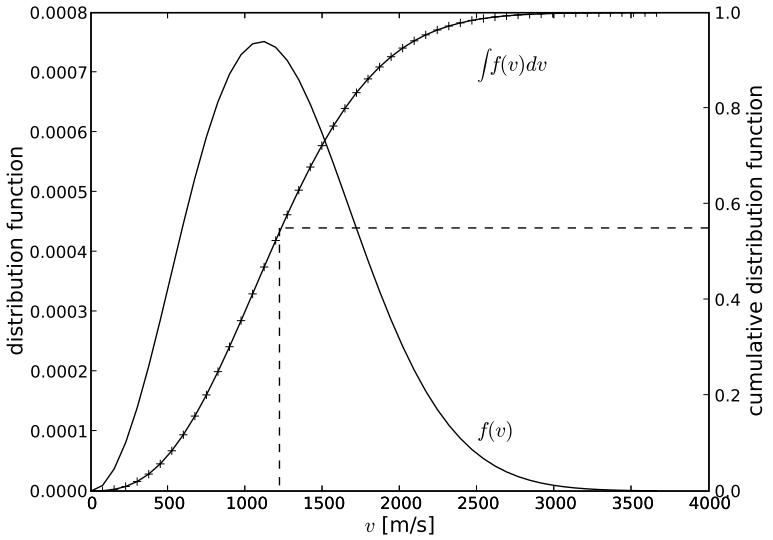

Figure 5.5: The Maxwell-Boltzmans speed distribution

two particles (seen as connecting line in figure 5.6), with all other perpendicular momentum components being conserved (Cronje, 2007). This necessitated the inclusion of a new axis system (x'-y') which is indicated in figure 5.6. From the one dimensional conservation of momentum and energy equation alongside the connecting line

$$v'_{He}m_{He} + v'_{Ag}m_{Ag} = V'_{He}m_{He} + V'_{Ag}m_{Ag} \tag{5.22}$$

$$\frac{1}{2}v'^2_{He}m_{He} + \frac{1}{2}v'^2_{Ag}m_{Ag} = \frac{1}{2}V'^2_{He}m_{He} + \frac{1}{2}V'^2_{Ag}m_{Ag} \tag{5.23}$$

where m is the mass, v' and V' are the velocities of the particle before and after collision. The velocities of the particles relative to silver before and after each collision, u' and U', can be expressed as

$$u'_{He} = v'_{He} - v'_{Ag} \tag{5.24}$$

$$u'_{Ag} = v'_{Ag} - v'_{Ag} = 0 \tag{5.25}$$

$$U'_{He} = V'_{He} - v'_{Ag} \tag{5.26}$$

$$U'_{Ag} = V'_{Ag} - v'_{Ag} = 0 \tag{5.27}$$

Rearranging equations (5.24) to (5.27) and then inserting them into equations (5.22) and (5.23) and solving simultaneously leads to the relative velocity of silver after collision,

i.e. the velocity gained by the silver particle during collision

$$U'_{Ag} = \frac{2m_{He}}{m_{He} + m_{Ag}} u'_{He} \tag{5.28}$$

The velocities of silver and helium relative to silver before collision can be obtained by

$$\mathbf{u}_{He} = \mathbf{v}_{He} - \mathbf{v}_{Ag} \tag{5.29}$$

$$\mathbf{u}_{Ag} = \mathbf{v}_{Ag} - \mathbf{v}_{Ag} = 0 \tag{5.30}$$

The incident angle ψ of $\mathbf{u}_{He}$ can be calculated by

$$\psi = \text{arctan2}(u_{He,z}, u_{He,x}) \tag{5.31}$$

where $u_{He,x}$ and $u_{He,z}$ are the x and z components of $\mathbf{u}_{He}$. If the impact plane is taken to be perpendicular to $\mathbf{u}_{He}$, the silver particle would experience more collisions on the side of the particle in the direction which it is moving. This produces a resistance to movement (Cronje, 2007), i.e. a drag force. The helium particle collides with the silver at an angle α, which is the angle between the incident $\mathbf{u}_{He}$ and the centreline connecting the two bodies. This angle was calculated by choosing a collision radius ($-c < r < c$, where c is the distance between the two particles' centres) and

$$\alpha = \arcsin\left(\frac{r}{c}\right) \tag{5.32}$$

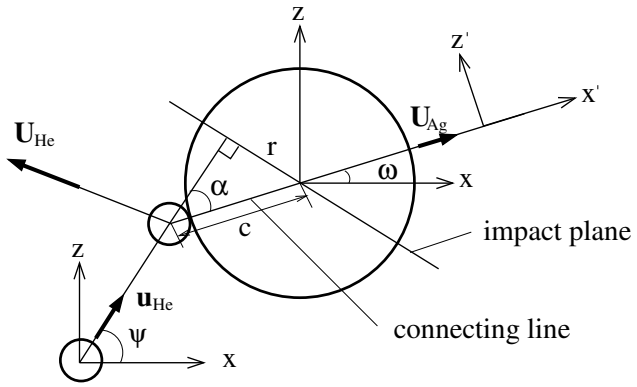

Figure 5.6: Collision between silver and helium atoms

As momentum is only transferred through this centreline connecting the two bodies, the velocity of the helium used in the one dimensional calculations of the silver is taken

as $\mathbf{u}_{He}cos(\alpha)$.

The time between collisions is taken as the mean free time τ of a silver atom in a helium environment (Cronje, 2007), which can be calculated as $\lambda/\overline{v}$. Sears (1964) stated that the relation between $\overline{v}$ and v_p is $\overline{v}$: $1.128v_p$. Taking λ as given by equation (A.12) and $\overline{v} = 1.128v_p$ results in

$$\tau = \frac{k_B T}{4\sqrt{2}\pi(R_{He} + R_{Ag})^2 p \times 1.128 v_p} \tag{5.33}$$

where R_{Ag} and R_{He} are the radius of the silver and helium atoms and p is the helium pressure. Cronje (2007)'s method for use of mean free time is slightly different, as he generated random mean free times by use of a mean free time distribution sampler object. The simulation time of 0.1 ms (a value obtained from Cronje (2007)) was achieved by multiple collisions until the summations of the mean free times equaled 0.1 ms.

The deflections obtained for the simulations were compared to Cronje (2007)'s work for the deflection of a single ion in table 5.2. The pressure and E columns are the size of the silver particle, pressure and electric field. The deflection columns display the results of Cronje (2007)'s model and the model proposed above, while the difference column is the difference between Cronje (2007)'s model and the 2D model, divided by Cronje (2007)'s model and is expressed as a percentage (Cronje (2007)-2D model / Cronje (2007)$\times$100%).

Table 5.2: Deflection comparison between the simulations and Cronje (2007)'s work

pressure	E	deflection [mm]		difference
	[V/m]	Cronje (2007)	2D model	[%]
1 atm	100 000	37.4	35.72	4.5
1 atm	50 000	18.7	17.69	5.4
90 bar	100 000	0.875	0.8165	6.7
90 bar	200 000	1.709	1.619	5.3

Cronje (2007) validated his results by comparing the velocities of the silver particles after collisions with the velocity distribution. The same is shown in figure 5.7 the velocity spectrum of the particles was divided into 50 bins, whereafter each velocity was added into one of these bins. The amount in each of these bins are plotted against the bin's velocity. The results do not have the same accuracy as Cronje (2007)'s results, but the binned velocities have a tendency to form a Maxwell distribution function. The random collisions of the silver with the helium results in the silver obeying its proper

velocity distribution. The simulation therefore converges to the physical state which is statistically expressed by the velocity distributions.

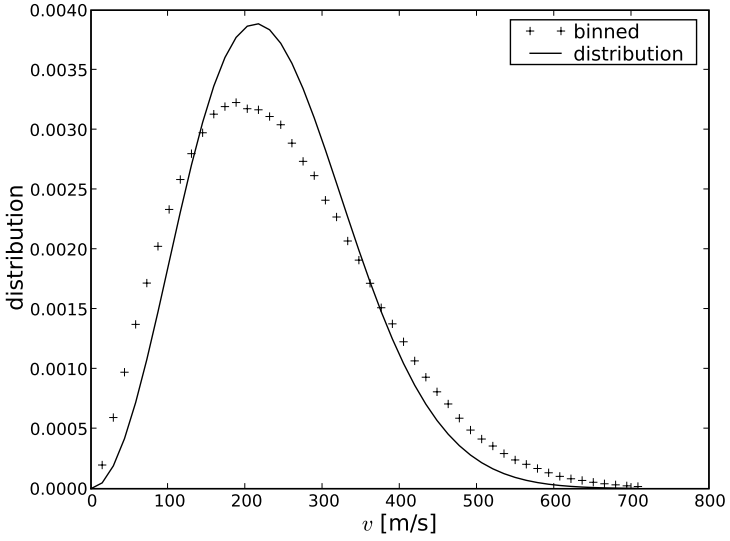

Figure 5.7: Velocities of silver particles after collisions

The stochastic model in turn was used to determine the distance which a particle travelled as it cooled down from plasma to ambient temperature. This cooling which a particle experiences simulates the cooling of silver particles which were created in the plasma in chapter 6. According to Lun (2008) silver is ejected at speeds of up to about 55 000 m/s from the plasma under vacuum. The assumption is made that this speed is the same for higher pressures but that the particles lose energy as they move away from the plasma due to collisions.

Table 5.3: The distance 55 000 m/s silver nanoparticles would travel in helium before cooling down to ambient temperature

particle radius	distance
0.5 nm	20.2 mm
1 nm	137 mm
2 nm	851 mm
5 nm	8.897 m

The distance which a silver particle would travel as it cooled down from 55 000 m/s is shown in table 5.3. From these distances and the fact that the inner diameter of the glass sleeve of the experiement (refer to chapter 6) is 18 mm, it was found that the larger

particles have too much momentum to be stopped by the helium before they reach the glass sleeve. These results do not correlate with experimental observations (see chapter 6) as 5 nm and larger particles were discovered on the deflection electrodes, see section 6.2. This implies that ejected silver atoms or custers increase their size by homogeneous nucleation with silver atoms. During homogeneous nucleation energy is released as radiation. Another explanation is that the assumption of larger particles being released at 55 000 m/s is not valid.

The stochastic model is also used to describe the deflection of a polarized atom in the nonhomogeneous electric field described in section 5.1. Due to this polarization the atom would theoretically be attracted to one electrode if the field was nonhomogeneous. The static average electric dipole polarizibility for ground state silver atoms has been theoretically calculated as 8.56×10^{-24} cm^3 (Lide, 1996). Replacing the m in equation (2.8) with equation (2.11), whereafter replacing ∇E^2 with $E_x E_{xx}$, which is done to ignore influences in the z direction, leads to

$$F_\alpha = \alpha E_x E_{xx} \tag{5.34}$$

to obtain the force on the particle due to the polarizability of the atom in a nonhomogeneous electric field. A force of 1.876×10^{-24} N ($8.56 \times 10^{-24}\text{cm}^3 \times 4\pi 8.854 \times 10^{-12}\text{F/m}(-14793\text{V/m})(-133175\text{V/m}^2)$) was calculated for the same nonhomogeneous electric field as used in section 5.1.

The force F_α, which was created due to the polarizability of the silver atom, is far less than the force which is created due to momentum transfer during collisions with the helium atoms. The most probable speed v_p of helium at 1 atm is calculated by means of equation (5.20) ($\sqrt{2 \times 8.31436 \times 293.15/(4/1000)}$ = 1103.994 m/s). This v_p is then used as the u'_{He} in equation (5.28), ($1103.994 \times 2 \times 4/(4 + 107)$ = 79.563 m/s) which is the velocity gained by the silver atoms. The change in velocity which F_α contributed was calculated by means of a rearranged version of equation (5.13), $1.876 \times 10^{-24} 107 \times 1.66 \times 10^{-27}/(1.922 \times 10^{-10})$ = 2.029 nm/s. The large difference between the two calculated velocities (79.563 m/s vs 2.029 nm/s) indicates that the particle's motion is far more dependant on the effect of Brownian motion than the force created by the polarizability of the atom.

The flight path of a silver atom which experiences Brownian motion due to colliding helium is displayed in figure 5.8(a). Figure 5.8(b) displayes the deflection of the same atom, with the same Brownian motion, but with a force due to the polarizability. From these two figures it is possible to see that there is virtually no increased deflection due

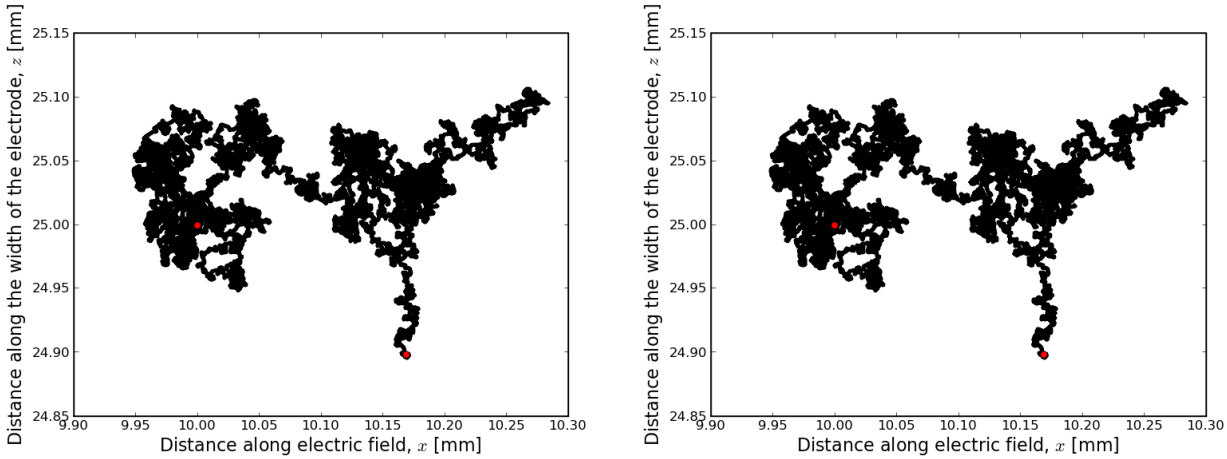

(a) The silver atom only experiencing Brownian motion

(b) The silver atom experiencing Brownian motion and a force due to the polarizability of the atom

Figure 5.8: The motion of a silver atom due to only Brownian motion, and due to Brownian motion and F_α (note that (a) and (b) are essentially identical as the effect of of polarizability is negligible)

to the force created by the polarizability of the atom. The deflection of the silver atom with the applied F_α after 0.1 ns is 10.1684152635 mm, while without the applied F_α it is 10.1684152593 mm. The deflection only differs in the eighth decimal value. This small difference in the distance traveled implies that the particles are far more likely to reach the surface of the electrodes due to Brownian motion than due to the F_α, from which it is concluded that F_α can be neglected.

5.3 Conclusion

In this chapter two deflection models were considered, namely the deterministic and stochastic deflection models. The latter was used to determine the deflection of single atoms while the former was used to determine the deflection microparticles.

From the deterministic deflection model it was found that sufficient deflection for the plate-out of silver particles with a radius of 3 μm cannot be accomplished by the experimental setup as described in chapter 4. It was also found that the gravitational force is far larger than the dielectrophoresis force, see appendix D.1, which signifies the ineffectiveness of dielectophoresis as a deflection means for microparticles.

From the results of the stochastic deflection model it was found that the deflection of ions are a possible means of scrubbing silver from helium. The same model was used to

determine the deflection due to the polarization of silver atoms in a nonhomogeneous electric field. From this deflection it was concluded that the silver's Brownian motion is far larger than the deflection. Therefore it is concluded that atoms cannot be deflected and successfully plate-out without being ionized.

In the nanometer sized particle range the deterministic deflection model can be used if it is incorporated with a Cunningham correction factor. However, the dielectrophoretic approximation is not valid in this range. Therefore the deflection in this size range cannot be determined.

Nichols *et al.* (2000) created silver nanoparticles by using laser ablation of microparticles and deflected them with ease in an electric field. Hence, silver nanoparticles were created in the next chapter by altering the experimental setup in chapter 4 to that described in chapter 6. These particles were deflected in a nonhomogeneous electric field.

Chapter 6

Arc discharge test

This chapter describes the changes made to the mixing chamber test apparatus (described and used in chapter 4) to create nanoparticles by means of the gas aggregation technique employed by Mahoney and Andres (1995). They used an arc to evaporate atoms from a metal, whereafter the atoms were cooled by collisions with gas atoms, which induced homogeneous nucleation and nanoparticle formation. This technique differs slightly from the gas aggreation technique explained in section 2.1.5 as the silver is evaporated by means of an arc, as opposed to Joule heating of the metal.

The creation of silver nanoparticles for the arc discharge test is based on the work done by Nichols *et al.* (2000), in which silver nanoparticles were successfully deposited onto an electrode. From the results of the mixing chamber test (section 4.2) and the results of the deterministic model (section 5.2) it was found that the apparatus as used in chapter 4 is not long enough to successfully deflect silver microparticles. A possible solution would be to create smaller silver particles for deflection in a nonhomogeneous electric field, as they have less mass and would therefore be more easily deflected. The influence of van der Waals forces on the dielectrophoresis forces of nanoparticles are also unknown, see section 2.5.3. Hence, the forces acting on the particle cannot be calculated, which makes the deterministic deflection model ineffective.

The changes made to the apparatus can be seen in figure 6.1. The convex lens and quartz glass in figure 4.3 were replaced with a high voltage feedthrough, which provides power to the arcing device through an insulated passage in the wall of the test vessel. The arcing device is shown in figure 6.2. The discharge holder was designed to insulate the two electodes from each other, see figure 6.1. An additional alteration was the removal of the filter at the exit, which became redundant as the particles created by this method are too small to be captured by the filter.

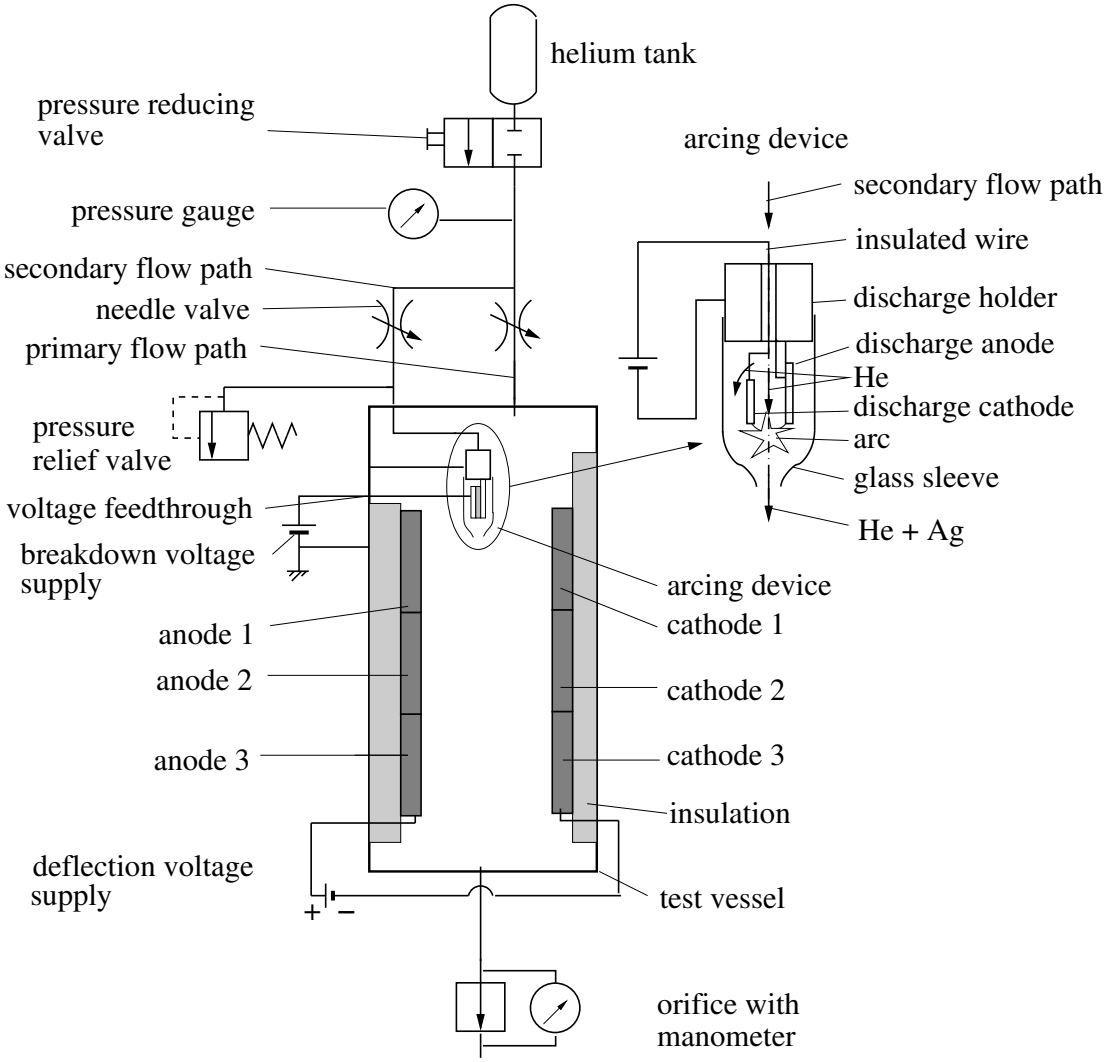

Figure 6.1: A schematic of the arc discharge experiment and the discharge holder

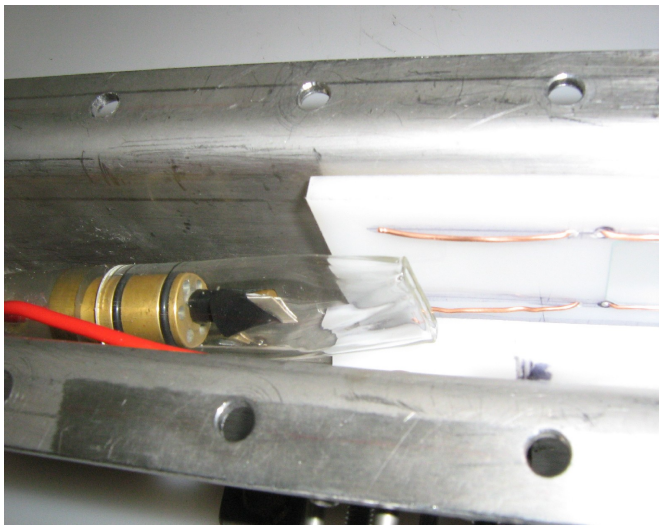

Figure 6.2: A photograph of the arcing device

6.1 Breakdown voltage supply

The schematic of the breakdown voltage supply, which was used to create the arc between the discharge anode and cathode, is shown in figure 6.3. To achieve breakdown between two electrodes with a gap of $\pm$ 1 mm between them, a voltage of 771 V is required, see appendix A.6.

When the nMOS (IRF840) transistor (see figure 6.3) is turned on ($V_{GS} > V_{TN}$ = 2 V) by an oscilloscope's 8 V sin wave, there is a current i_P that runs through the primary windings. The inductor core flux increases, according to Mohan *et al.* (1995). When the transistor is switched off, the energy stored in the inductor core causes the current i_d to flow through the secondary winding. The term flyback is derived from the saw-tooth profile of the changing i_d.

The rate at which the voltage in the flyback converter is increased can be written in the form

$$\frac{V_o}{V_P} = \frac{N_S D}{N_P(1-D)} \tag{6.1}$$

where D is the duty cycle, V_P and V_S are the primary and secondary voltages, while N_S and N_P are the number of primary and secondary windings (Mohan *et al.*, 1995).

When the transistor is in on-mode, i_P increases as the current flowing through the

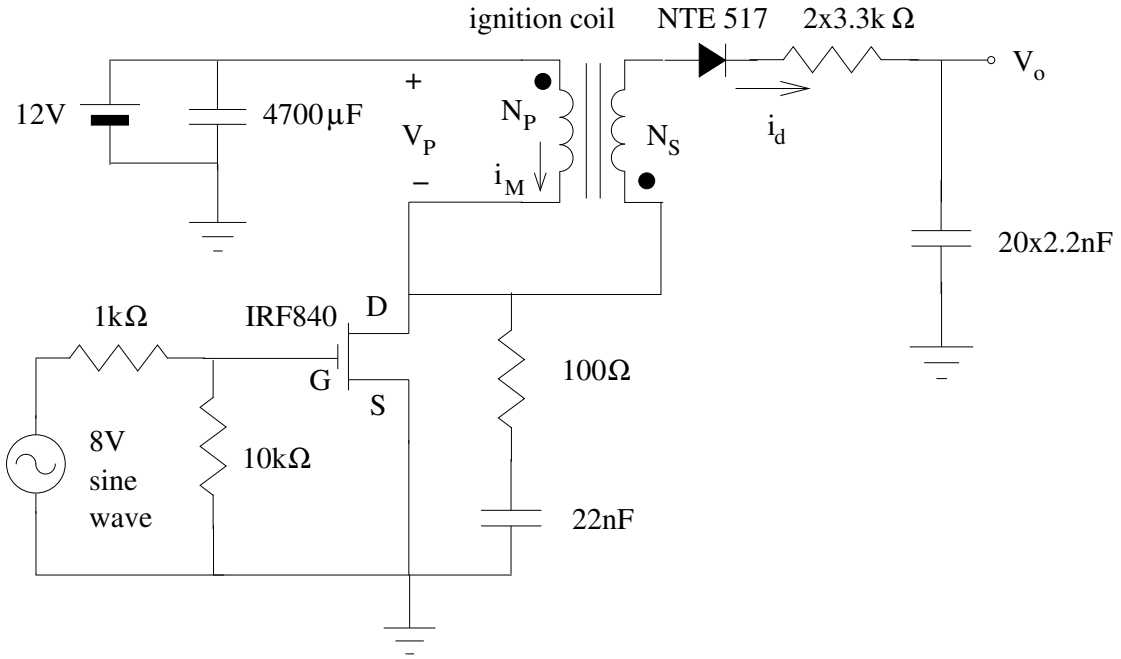

Figure 6.3: The schematic of the flyback converter breakdown voltage supply (Lun, 2008)

coil increases. To avoid damage to the transistor the on-mode time duration, or the maximum time it can be in on-mode, can be calculated by using the equation (Guru and Hüsyin, 2005)

$$V = L\frac{di}{dt} \tag{6.2}$$

where L is the inductance of the primary coil, which was measured with a L/C meter (Escort ELC-BLD, serial number 99100134) as 3.99 mH. In this experiment the continuous drain current (which passes through the transistor) of 3 A was designed for, as opposed to the rated maximum of 8 A, which leads to a safety factor of 8/3 = 2.67. Applying the voltage of 12 V to a rearranged version of equation (6.2) results in the maximum on-mode time duration of 1 ms ($3 \times 3.99 \times 10^{-3}/12$ = 1 ms). This on-mode time duration is the lower frequency limit ($1/10^{-3}$ = 1 kHz) of the sine wave.

According to Guru and Hüsyin (2005) a time varying current $i_M(t)$ running through a number of windings induces a time varying magnetic field. According to Faraday's law of induction the electromotive force (emf) produced in the coil can be written as (Guru and Hüsyin, 2005)

$$e = N\frac{d\phi}{dt} \tag{6.3}$$

where N is the number of turns in the coil and ϕ is the magnetic flux. This emf creates a current in the coil, which tends to oppose the variations in the original time varying current (Guru and Hüsyin, 2005). A back emf is created when the transistor is switched from on- to off-mode. This back emf creates a voltage spike in the primary and secondary windings. To ensure that the voltage spike does not damage the transitor, a transistor with a high absolute drain to source voltage V_{DS} or a snubber can be employed. Both were implemented. The snubber employed in figure 6.3 is the 100 Ω resistor and the 22 nF capacitor placed in series, which suppresses the rapid increase in voltage across the transistor.

It was found that the air gap in the core influences the output voltage V_o when the frequency is varied. This is due to Faraday's law of induction, where the emf is related to the induced voltage (Guru and Hüsyin, 2005). Switching between on- and off-modes in the transistor too quickly causes electrical hysteresis either in the air gap and/or the steel, which reduces the performance of the transformer. The lag between V_P and V_S, which is created by the hysteresis, causes the electrical energy to be dissipated into heat energy. This heat energy could be detected as there was a higher temperature in the ignition coil casing (which could be detected by hand) when operating at higher frequencies than when operating at the suggested frequencies. To determine the effect of this loss caused by hysteresis, the voltage gain (output over the input voltages) for

various frequencies was measured and plotted in figure 6.4(a).

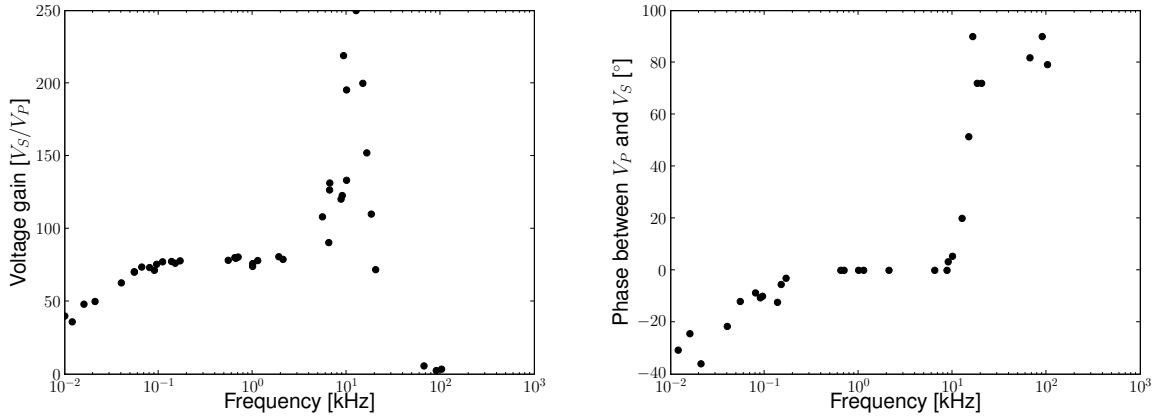

(a) Frequency vs voltage gain (V_P/V_S) (b) Frequency vs phase between V_P and V_S

Figure 6.4: Operation frequencies of the flyback converter

The upper frequency limit was determined by the frequency vs phase graph, see figure 6.4(b). It was found that V_P lags V_S by 90° at frequencies above 10 kHz, which corresponds to an efficiency loss. It is therefore suggested that the function generator should be operated between 1 and 10 kHz.

Taylor and Secker (1994) state that the energy stored in a capacitor can be expressed as

$$E_{cap} = \frac{1}{2} C V_o^2 \tag{6.4}$$

where C is the capacitance and V_o is the output voltage. More silver can be released by applying a more energetic arc. The energy of the arc can be increased by increasing the voltage or the capacitance. Increasing the breakdown voltage can be achieved by increasing the gap between the discharge electrodes. Increasing the capacitance can be achieved by an increase in capacitor capacitance. However, the change in capacitance influences the time required to charge a capacitor, which can be expressed as 5 RC, where R is the output resistors' resistance. Decreasing the resistance would decrease the time necessary to charge the capacitor. However, there is a lower limit as the diode (NTE 517) can only handle a reverse surge current (shown as -i_d in figure 6.3) of 100 mA. The resistors (2×3.3 kΩ) and capacitors (20×2.2 nF) that were finally chosen, in order to optimise the amount of silver ejected, were as a result of experimentation.

6.2 The observations of the plated silver particles

The observations of the plated silver particles in the arc discharge test are discussed in this section. Changes made to the electrodes used in the mixing chamber test are also explained. The observations are critically analysed, whereafter a hypothesis is proposed to explain why the particles plate-out with higher efficacy than can be explained by dielectrophoresis (DEP) in section 5.1.

Initially tests were done with deflection electrodes made of microscope glass slides covered with aluminium foil. After investigation under a microscope it was found that the surface roughness of the foil, as a result of the foil manufacturing process, is larger than 20 nm, as shown in figure 6.5. The 20 nm limit was imposed as some of the silver particles manufactured in the arc discharge test are smaller than this value. To overcome the previously stated problem the glass slides were ultrasonicly cleaned (to remove any dust particles) and plated with aluminium by Metglo (2009). The aluminium was evaporated under vacuum and plated onto the glass microscope slides.

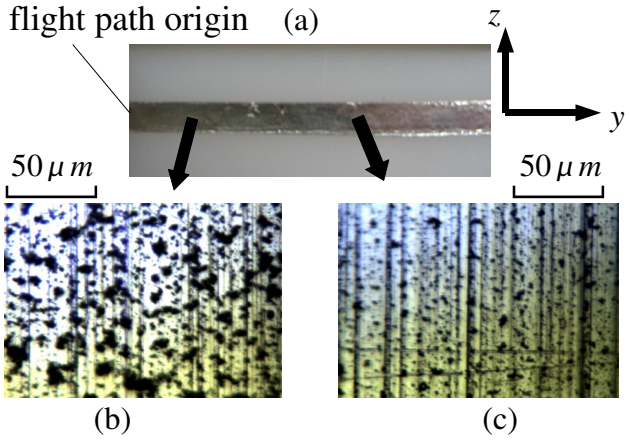

Figure 6.5: 5 mm electrode with microscope photos (magnification of 2660x)

The initial test ran for two hours with helium bulk velocity of 0.0161 m/s and an electric potential of 500 V. The silver which deposited onto the electrodes is displayed in figures 6.5 and 6.6. From these two figures it is evident that the plated particles are larger on the 5 mm wide electrode (anode in this case) than the 25 mm wide electrode (cathode). More particles plated out on the end nearest the flight path origin, see figures 6.5(a) and 6.6(a). This is due to the flowing helium being depleted of particles at the end of the flight path. Larger particles have also been found to deposit at the start of the flight path, which can be seen in figure 6.5(b). Smaller particles, see figure 6.5(c),

deposit further down the flight path. There is a clear difference in the size of the particles which collected on the anode (figure 6.5) to those which collected on the cathode (figure 6.6).

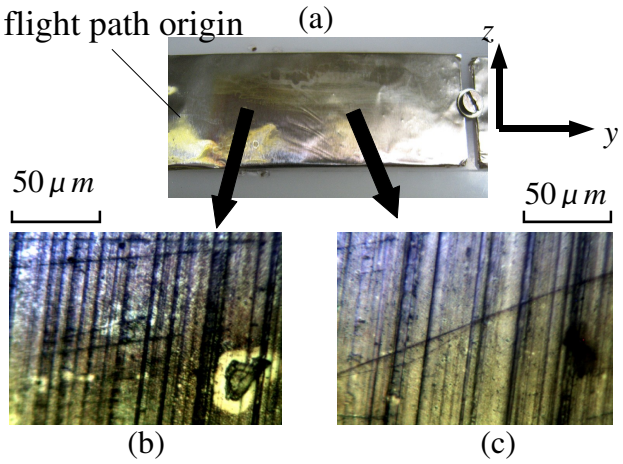

Figure 6.6: 25 mm electrode with microscope photos (magnification of 2660x)

An interesting phenomenon occurs when a large particle collected on the electrode, as seen in figure 6.6(b). This particle has an area around it in which no deposition of silver occured, which was termed a white spot. This can be explained by the large deposited particle creating a stronger localised electric field around it than its immediate surroundings, as it is conductive. The localised field creates a higher applied force field towards the large particle, on which the silver then collects.

(a) Colour variation of plated silver on the cathode of test 7

(b) Coagulation of particles to centre of 5mm electrode in test 2

Figure 6.7: Photographs of some electrodes

The most obvious indication that particles have plated out is the visually observed colour variations which they give to electrodes. Figure 6.7(a) displays the 25 mm wide electrode of test 7 and the colour of this electrode's silver plating is displayed in table 6.1. The particles are also seen to concentrate at the centre of the 5 mm electrode, see figure 6.7(b). This colour variation, which was observed after the tests, has been tabulated in table 6.1. In this table the potential column is the electric potential applied to the 25 mm gap, while the v_{He} is the helium bulk velocity. The type column states whether an alumnium foil or alumnium deposited glass slide was used. The remaining columns display the colour variations and percentages of the glass at a specific y (see figure 5.1 for explanation on the coordinate system) which is covered with that colour. From table 6.1 it is evident that for the same electric field and helium velocity, more particles collect on the anode. In such cases it also takes longer for particles to complete plating out, as more particles are attracted towards the anode.

Table 6.1: Colour variations of silver deposits

test no	potential [V]	v_{He} [m/s]	type	0 [mm]	10 [mm]	20 [mm]	30 [mm]	40 [mm]	50 [mm]	60 [mm]	70 [mm]	80 [mm]	90 [mm]	100 [mm]	110 [mm]	120 [mm]	130 [mm]	140 [mm]
Colour varations on 5 mm electrode																		
1	-300	0.0191		100%	100%	90%	80%	50%	40%	20%	10%	5%	5%					
2	300	0.0184			80%	80%	80%	60%	40%	20%	10%	5%						
3	-500	0.0198		80%	100%	100%	100%	100%	70%	80%	80%							
4	500	0.0198		50%	80%	80%	60%	20%	5%	5%								
5	-500	0.0296		100%	100%	100%	100%	80%	80%	20%	10%	80%	80%					
6	500	0.0317		80%	80%	80%	80%	80%	80%	80%	80%	80%	80%					
7	500	0.0323		60%	80%	80%	80%	80%	80%	60%	40%	20%	10%	5%	5%	5%	5%	
8	300	0.0331		10%	40%	60%	60%	40%	40%	20%	10%	10%						
9	500	0.0169			40%	60%	40%	20%	10%	5%								
14	500	0.0234			80%	80%	60%	40%	10%	5%								
Colour varations on 25 mm electrode																		
1	-300	0.0191	foil	80%	80%	80%	70%	50%	20%	80%	80%	80%	80%	60%				
2	300	0.0184	foil	80%	80%	80%	80%	100%	100%	100%	100%	100%	100%	100%	100%	100%	100%	100%
3	-500	0.0198	foil	80%	80%	80%	50%	10%	10%	5%								
4	500	0.0198	foil	80%	80%	90%	60%	70%	100%	80%	80%	80%	80%	80%	80%	60%	60%	60%
5	-500	0.0296	foil		20%	40%	60%	60%	40%	20%	10%	5%						
6	500	0.0317	foil	80%	80%	100%	100%	90%	90%	90%	90%	90%	90%	90%	90%	90%	90%	90%
7	500	0.0323	plated	80%	60%	50%	40%	100%	100%	100%	90%	80%	70%	60%	50%	50%	50%	50%
8	300	0.0331	plated	80%	80%	90%	100%	100%	100%	100%	100%	100%	100%	100%	100%	100%	100%	100%
9	500	0.0169	plated	80%	80%	90%	90%	90%	90%	90%								
10	300	0.0195	plated	80%	90%	100%	100%	100%	100%	100%	100%	100%	100%	100%	100%	100%	100%	100%
11	500	0.0162	plated	80%	80%	80%	20%	5%										
14	500	0.0234	foil	80%	80%	90%	100%	100%	100%	80%	80%	80%	80%	80%	80%	80%	80%	80%

Four microscope images of the aluminium deposited glass slide anode of test 11 are

displayed in figures 6.8(a) to (d). At y = 0 mm the columating glass sleeve ends (see figure 6.1) and the fligh path starts. In figure 6.8(a) (at y = -5) there is no plated silver (the black dots are dust particles). In figure 6.8(b) (at y = 10 mm) the plated silver appears black, which is indicated in table 6.1, with white spots. In figure 6.8(c) (at y = 25 mm) the colour is fading to a light black with larger white spots, while in figure 6.8(d) (at y = 35 mm) the colour has faded even more. It is clear from these microscope images, as well as figures 6.5 and 6.6, that the colour intensity of the plated silver is influenced by the amount and the size of the plated silver particles.

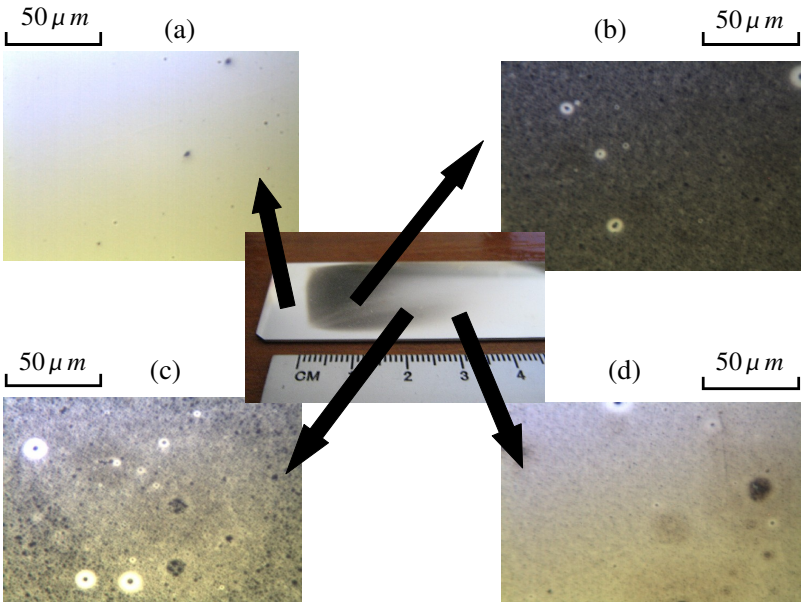

Figure 6.8: Microscope images of the 25 mm electrode of test 11

An atomic force microscope (AFM) was used for further investigation of the white spots in figure 6.8(c). An AFM 3D view is displayed in figure 6.9. The lower lying area is a white spot, while the elevated area in the centre is the black dot, which is where the most silver is attracted to. This attraction was due to the stronger localised force field around the plated particle.

Test 12 was considered unsuccessful as anode 1 lost its electric connection to anode 2. In some cases when 500 V or more was applied to the electrodes, the aluminium directly around the screw holding the electrode in place was stripped, which breaks the electrical connection. The removed aluminium is visible on the left electrode in figure 6.10(b). This removal of aluminium was the reason no more than 500 V per test for glass slides plated with aluminium was applied. In test 12 silver particles plated onto the connected cathode at the start of the flight path at y = 0 mm in figure 6.10(c) and the second anode which was connected at y = 70 mm in figure 6.10(b).

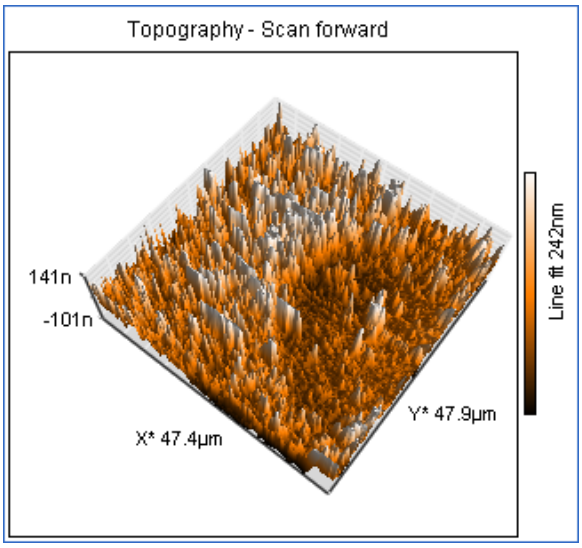

Figure 6.9: AFM 3D view of a white spot of figure 6.8(c)

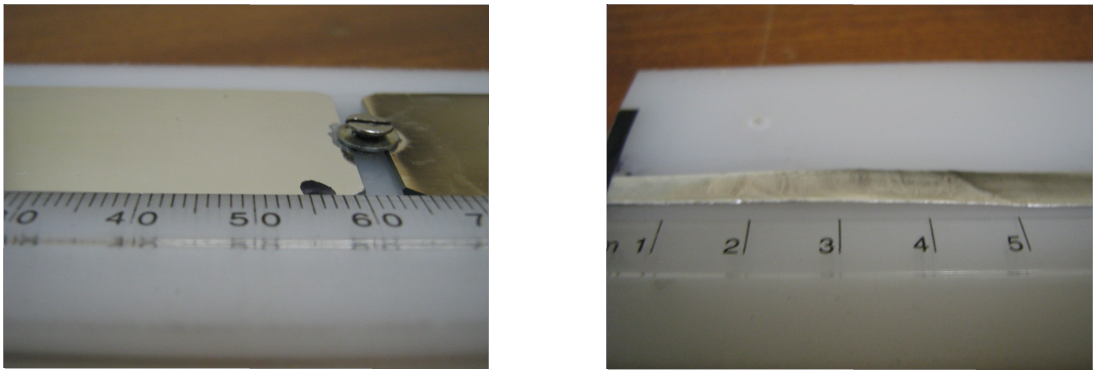

(a) 25 mm electrode, y = 30 - 70 mm

(b) 5 mm electrode, y = 0 - 60 mm

Figure 6.10: Test 12, electric potential of 500 V and v_{He} of 0.0181 m/s

The shapes (triangular ▷ or circular ○ as determined by the AFM can be seen in figure 6.12) of the particles, on the 25 mm electrode, as seen from the top are displayed in table 6.2. The typical height and width (in the size column) of the particles, which is defined in figure 6.11(b), were obtained from cross-sectional profiles of the plated silver. Note that width refers to the largest side of the triangle and the diameter of the circle. The shaded view of the cross-sectional profile of four spherical particles is displayed in figure 6.11(a). The shape variation (triangular to circular) does not appear to be influenced by any of the factors which were investigated, such as helium velocity and deflection electric field strength. It was found that the variation in the shape of the particles can occur in the same test, see figure 6.12. The triangular shapes (which are not uncommon as Zeng *et al.* (2008) manufactured them by means of wet chemistry)

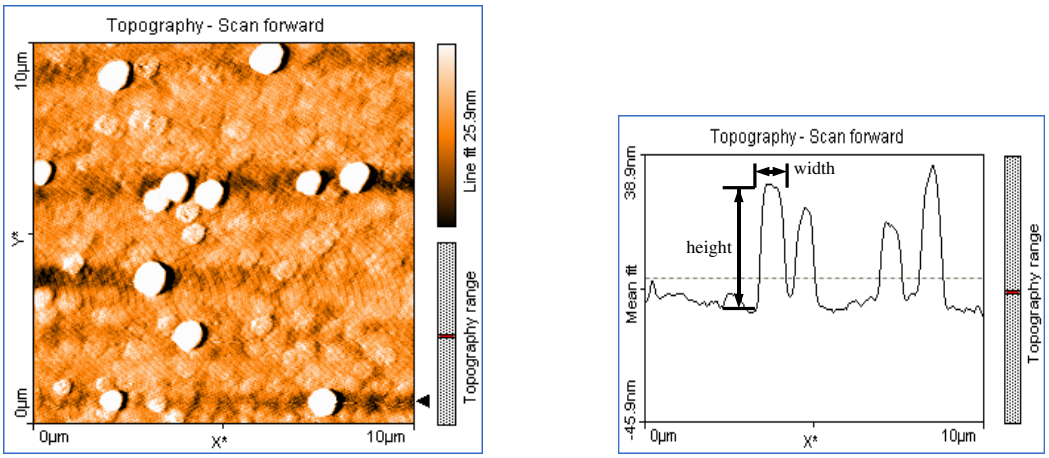

(a) Shaded view (b) Cross-sectional profile

Figure 6.11: Test 11 at y = 25 mm, electric potential of 500 V and v_{He} of 0.0162 m/s

always have one point directed to the direction from which the helium flows and two points in the direction opposing the flow. The width of the particles appears to be greater than the height (by a factor of at least 10), see table 6.2. This factor can be attributed to re-entrainment, which is explained in section 2.5.7. The particles which plated with their larger sides on top of the electrode experience a smaller moment due to the flowing helium than the particles which plated with their shorter sides on top of the electrode do. This smaller moment decreases the chance of re-entrainment.

Table 6.2: Shapes and sizes of particles collected on 25 mm electrode

test	potential	v_{He}		10 mm	25 mm	55 mm	80 mm	105 mm	130 mm
7	500	0.0323	height [nm]	25	30-60	20-30	30-60	50	20
			width [μm]	1-2	1-2	1-2	1-2	1-2	1-2
			shape	▷	▷	▷	▷	▷/○	○
8	300	0.0331	height [nm]	12-30	20	200-300	25-350	20-30	
			width [μm]	1-2	1-2	2-3	2-3	1-2	
			shape	▷	▷/○	▷	▷	▷	
9	500	0.0169	height [nm]	30-150	150-170	15			
			width [μm]	2-3	2-3	0.5-1			
			shape	▷	▷	▷			
10	300	0.0195	height [nm]	30-150	20-100	50-200	30-125		
			width [μm]	2-3	1-2	2-3	1-2		
11	500	0.0162	height [nm]	20-80	40-60				
			width [μm]	0.5-1	1-2				
			shape	○	○				

It was necessary to establish the thickness of the silver layer to determine if the particles agglomerated on the surface. The agglomeration of particles would aid re-entrainment, see section 2.5.7. The silver deposited aluminium plated glass slides were sent to the

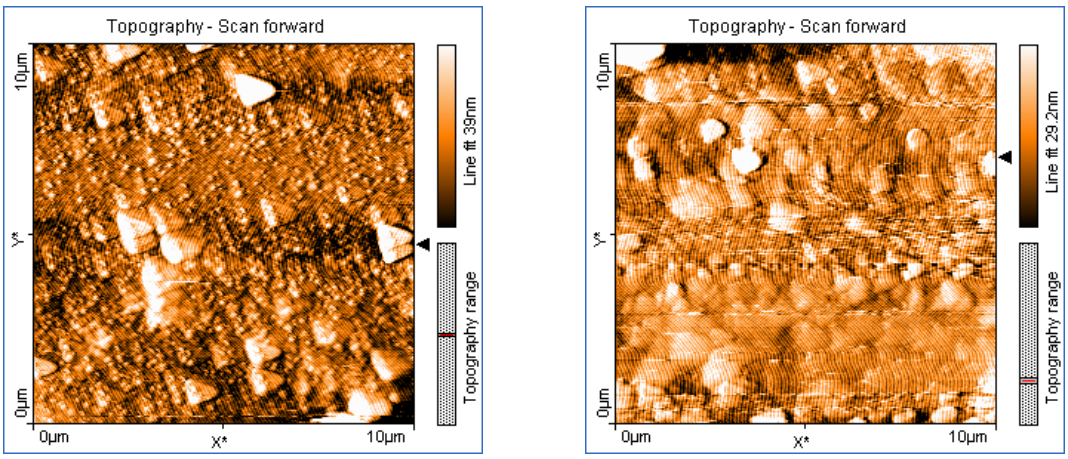

(a) Shaded view at y = 55 m (b) Shaded view at y = 130 mm

Figure 6.12: Test 7, electric potential of 500 V and v_{He} of 0.0323 m/s

National Metrology Institute of South Africa (NMISA) for analysis with the use of scanning X-ray photoelectron spectroscopy (SXPS) (Jordaan, 2009). Two of these analysed samples are displayed in figure 6.13. The sputter time represents the depth profile of the sample as the sample was irradiated by an X-ray beam. From these two figures it is possible to see that other atoms, such as carbon and oxygen, are also present on the glass slide. This brought forth the hypothesis that the particles were positively and negatively charged in and around the arc. This bipolar charging (Borra, 2006) is possible due to negative and positive ions forming from the atoms as is shown in figure 6.13. According to NMISA, helium and hydrogen are two elements which cannot be detected by SXPS, which implies that molecules containing helium and hydrogen might exist on the slides although they are not seen in figure 6.13.

After each experiment the silver of the discharge electrodes reacts with the air molecules when new collection electrodes are placed into the apparatus. This reaction forms a brown/black layer of silver(I)oxide, silver(II)oxide or possibly silver(II)carbonate. Lide (1996) states that these inorganic compounds are presented as gray powder, brown/black cubic crystals and yellow monoclinic crystals, respectively. These impurities would then be the first to ionize in the arc as they form the top layer of the electrode. Given the presence of these impurities an electrode spacing distance of 5 mm was used to create an arc. After cleaning the electrodes with acetone, the same voltage was applied and the distance of electrode spacing was reduced to 0.5 mm. The oxygen, carbon and possibly hydrogen reduces the breakdown voltage by having lower ionization potentials than helium.

The inorganic ionized molecules increase their size by ion-induced nucleation in and

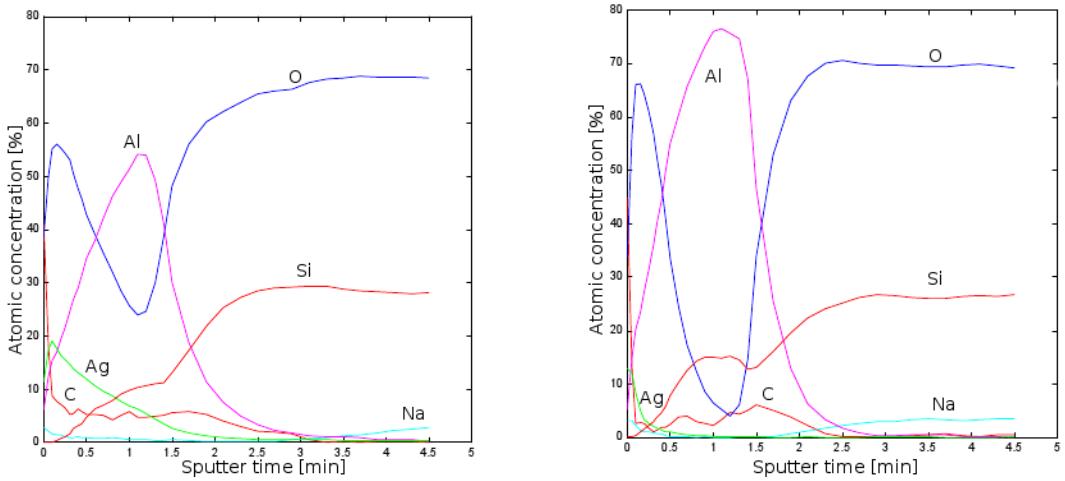

(a) Test 11 at y = 5 mm (b) Test 7 at y = 15 mm

Figure 6.13: SXPS depth profile provided by Jordaan (2009)

around the arc (Borra, 2006). They are further charged by field and/or diffusion charging, depending on the size of the particle. These charged particles are then transported by the flowing helium and deflected by an electrostatic force towards the deflection electrodes. As the arc removes the impurities from the discharge electrodes the silver particles become smaller and the inorganic ionized molecules are replaced by pure silver particles. Hence, larger particles are plated out first, followed by smaller particles, which then plate-out onto the initial deposited particles. The initial deposited particles create a localized electric field around them, which attracts the smaller particles towards them. The previously mentioned white spots in figures 6.6 and 6.8 illustrate this phenomenon.

In an alternating current atmospheric pressure Townsend-like discharges (ac APTD) the particles are immersed in alternating positive ion and electron clouds (Borra, 2006). Hence removing the impurities would not force all particles to be charged positively. As the positive ions' mobility is smaller than that of the electrons, the time which the ions are immersed in the positive cloud is longer, which results in a higher probability of neutral particles gaining a positive charge (Borra, 2006).

6.3 Deflection of bipolar charged particles

As stated in section 2.5.8, particles can be charged by field and/or diffusion charging, depending on their size. This section discusses these two charging methods and the deflection of the charged particles in the nonhomogeneous electric field of the appara-

tus as used in this chapter.

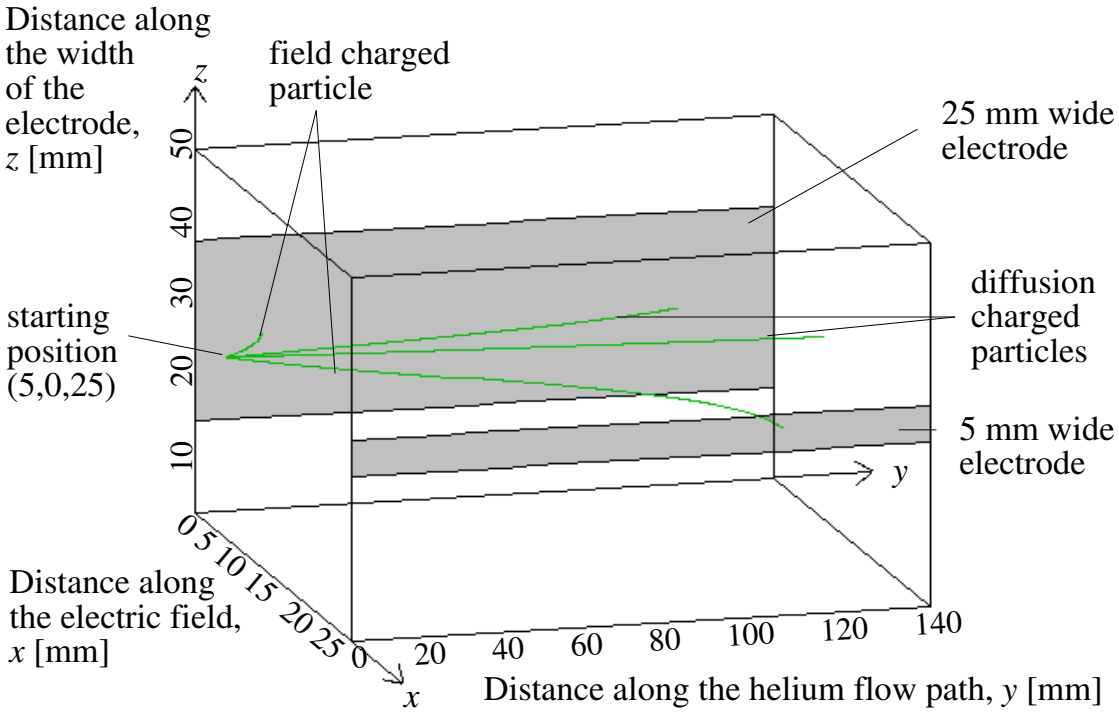

Figure 6.14: Flight path of 100 nm charged particles due to field or diffusion charging which is initiated at (5 mm, 0 mm, 25 mm)

The force on the particle can be calculated by multiplying the electric field strength of the various control volumes by equation (2.16) or (2.17). The force on the 100 nm articles at the starting position (as displayed in figure 6.14) due to field charging is $13060\text{V/m} \times 4\pi 8.854 \times 10^{-12}\text{F/m} \times 10^{-7}\text{m} \times 13060\text{V/m} = 1.898 \times 10^{-9}$ N, while the force due to diffusion charging is $13060\text{V/m} \times 6\pi 8.854 \times 10^{-12}\text{F/m} \times 10^{-7}\text{m} 1.38 \times 10^{-23}\text{J/K} 293.15\text{K} / 1.6 \times 10^{-19}\text{C} = 5.507 \times 10^{-15}$ N. The 100 nm particle was chosen as it can be charged by field and/or diffusion charging. The electric field is due to an electric potential of 500 V over the 25 mm flight path of the experiment in this chapter and is calculated as explained in appendix D.1.

Figure 6.14 shows the flight paths as calculated by the deterministic deflection model (see section 5.1) of 100 nm radius particles, which have been charged by field or diffusion charging. Note that it is assumed that the particles are deposited when they reach the last control volume, as the E_{xx} and hence F_{DEP} cannot be calculated for that control volume. E_{xx} cannot be calculated as there is no next control volume which can be used for equation (5.7). This also means that the particles which started away from the cen-

tre of the electric field (at z = 25 mm) do not reach the electodes. These particles do not experience the large z directional force of the last control volume, which would have concentrated the particles to the centre of the 5 mm wide electrode. The final positions of the deflected particles are shown in figures 6.15 to 6.20.

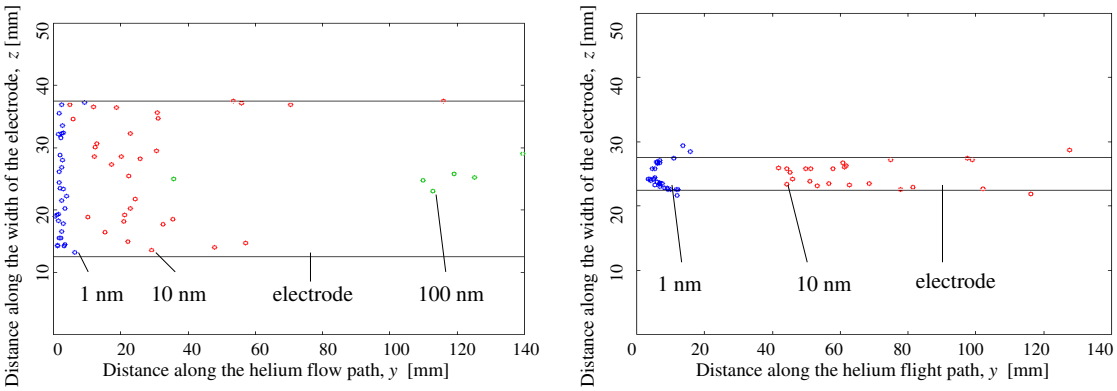

(a) 25 mm electrode (b) 5 mm electrode

Figure 6.15: Diffusion charging, electric potential of 500 V and v_{He} of 0.0198 m/s

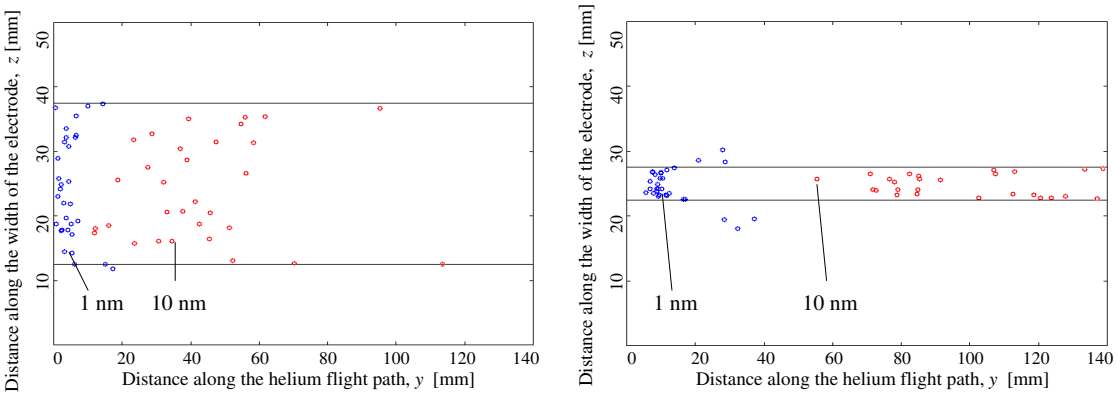

(a) 25 mm electrode (b) 5 mm electrode

Figure 6.16: Diffusion charging, electric potential of 500 V and v_{He} of 0.0320 m/s

From figures 6.15 to 6.17 it is possible to see that smaller particles would theoretically deposit sooner due to diffusion charging. With field charging (see figures 6.18 to 6.20) the exact oposite occurs, which is the same as was experienced in the experiments, see figure 6.5.

Table 6.3 displays the sample mean and standard deviation of the calculated results from the data given in figures 6.15 to 6.20. The method of calculating the sample mean and standard deviation is decribed in section 4.2. The charging column displays the

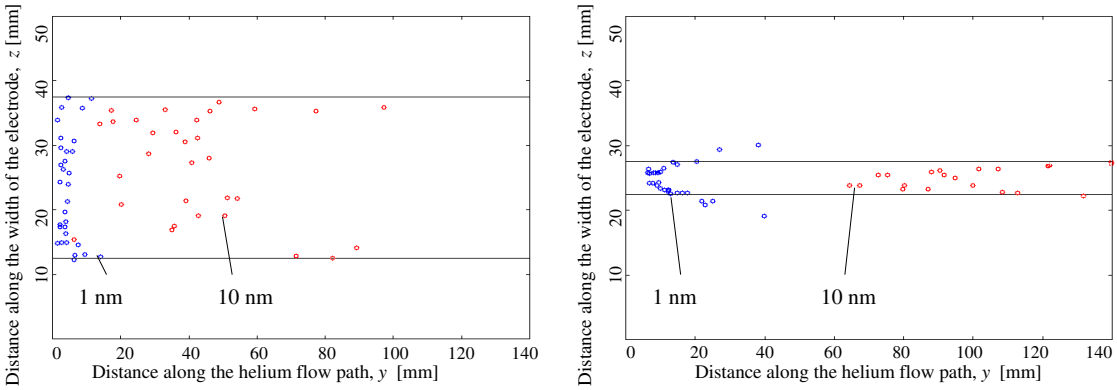

(a) 25 mm electrode (b) 5 mm electrode

Figure 6.17: Diffusion charging, electric potential of 300 V and v_{He} of 0.0198 m/s

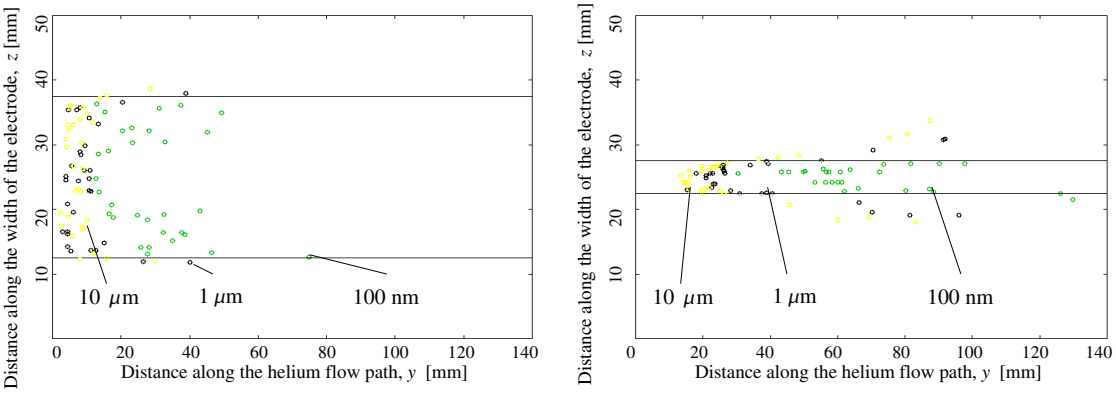

(a) 25 mm electrode (b) 5 mm electrode

Figure 6.18: Field charging, electric potential of 500 V and v_{He} of 0.0198 m/s

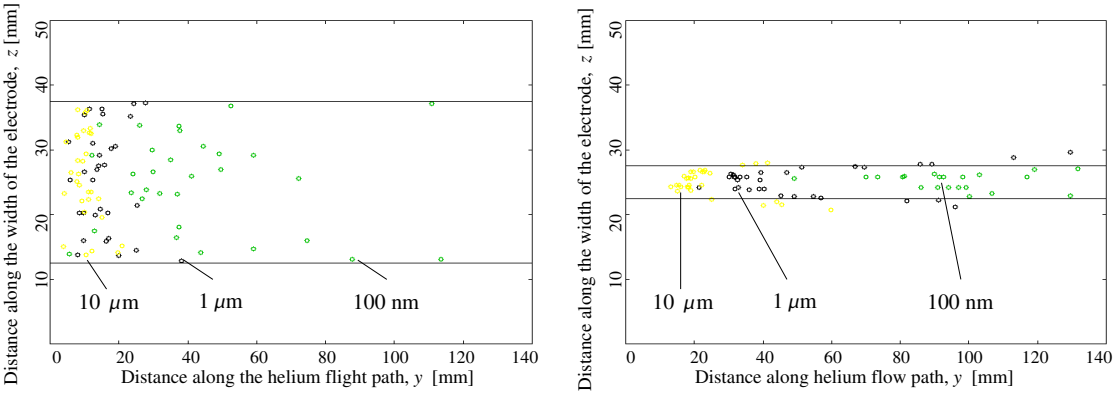

(a) 25 mm electrode (b) 5 mm electrode

Figure 6.19: Field charging, electric potential of 500 V and v_{He} of 0.0320 m/s

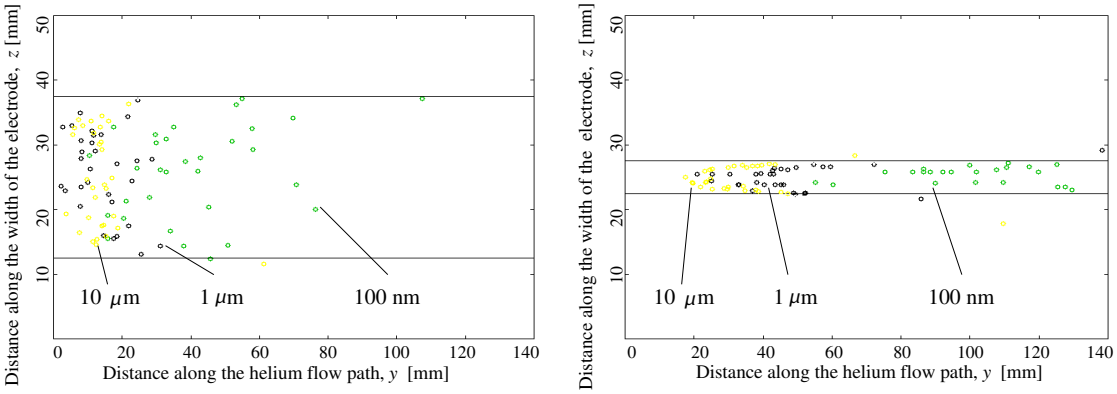

(a) 25 mm electrode (b) 5 mm electrode

Figure 6.20: Field charging, electric potential of 300 V and v_{He} of 0.0198 m/s

charging method, the particle size column displays the size of the particle, the potential column displays the electric potential which was applied to the 25 mm gap between the electrodes, while the last two columns display the sample mean and standard deviation of the particles which plated onto the 5 and 25 mm electrodes. The 100 nm particle was not incorporated in this section as it is believed that it gains charge by field and diffusion charging as it is in the size range between the two charging mechanism.

The calculated values reflected in figures 6.15 to 6.20 and table 6.3 were compared to the experimental results displayed in table 6.1. It was found that the 10 μm particles plate-out sooner than the 10 nm particles (17.156 mm vs 34.983 mm, see table 6.3) which correlates with what can be seen in figure 6.5. This difference in distance along the helium flow path is due to the different charging mechanisms. It was found that although the particles which plated out are in the same ballpark as the theoretically calculated ones, notable differences between the theoretical and physical results exist. According to the theoretical results particles would plate-out more quickly on the 25 mm electrode, because those particles have a shorter flight path. In the experimental case, the particles do the exact opposite. It is believed that the starting position which was assumed is incorrect as the particles might start closer to the 5 mm electrode in the experiment.

Kadaksham *et al.* (2004) stated that Brownian motion of particles becomes important for particle motion calculations in the case of sub-micrometer sized particles. The force due to Brownian motion can written as

$$F_{Br} = \xi \left(\frac{12\pi\mu R k_B T}{dt} \right)^{\frac{1}{2}} \tag{6.5}$$

Table 6.3: Sample mean and standard deviation of deflected field and diffusion charged particles

charging	particle size	voltage [V]	v_{He} [m/s]	25 mm electrode [mm]	5 mm electrode [mm]
Field	1 μm	300	0.0198	16.111 ± 0.058	43.997 ± 0.297
		500	0.0198	11.591 ± 0.047	30.738 ± 0.361
		500	0.0320	18.181 ± 0.118	48.553 ± 0.897
		-300	0.0198	19.163 ± 0.213	45.901 ± 0.568
		-500	0.0198	10.706 ± 0.036	36.591 ± 0.496
		-500	0.0320	16.779 ± 0.089	54.543 ± 0.924
	10 μm	300	0.0198	17.156 ± 0.053	41.061 ± 0.580
		500	0.0198	8.471 ± 0.013	28.191 ± 0.239
		500	0.0320	9.263 ± 0.015	31.189 ± 0.287
		-300	0.0198	16.786 ± 0.063	45.539 ± 0.722
		-500	0.0198	10.593 ± 0.028	28.190 ± 0.350
		-500	0.0320	11.575 ± 0.033	31.177 ± 0.418
Diffusion	1 nm	300	0.0198	4.371 ± 0.011	12.494 ± 0.067
		500	0.0198	2.848 ± 0.002	7.220 ± 0.019
		500	0.0320	4.603 ± 0.006	11.668 ± 0.049
		-300	0.0198	5.100 ± 0.018	12.091 ± 0.054
		-500	0.0198	2.791 ± 0.003	6.980 ± 0.013
		-500	0.0320	4.511 ± 0.007	11.281 ± 0.034
	10 nm	300	0.0198	34.983 ± 0.350	96.720 ± 1.023
		500	0.0198	22.992 ± 0.139	68.634 ± 0.888
		500	0.0320	37.041 ± 0.362	93.415 ± 0.939
		-300	0.0198	16.873 ± 0.063	45.539 ± 0.722
		-500	0.0198	10.593 ± 0.028	28.190 ± 0.350
		-500	0.0320	11.575 ± 0.033	31.177 ± 0.418

where ξ is a random vector with a Gaussian distribution, μ is the viscosity of the helium, R is the radius of the particle and dt is the numerical integration time step size. Using equation (6.5) by assuming $\xi = 1$, which would result in the largest Brownian force, produces a force of 9.916×10^{-15} N ($\sqrt{12\pi 19.93 \times 10^{-6} \times 10^{-7} 1.31 \times 10^{-23}/10^{-5}}$). This value is far larger than that the F_{DEP} force, see table 5.1. The Brownian motion force is in the same range as the coulombic force created by diffusion charging (5.5066×10^{-15} N) but smaller than the coulombic force created by field charging (1.898×10^{-9} N). Therefore, Brownian motion can influence the deflection of nanoparticles, especially if the force is only due to dielectrophoresis. Brownian motion can contribute as much as 64% ($\frac{9.9159 \times 10^{-15}}{9.9159 \times 10^{-15} + 5.5066 \times 10^{-15}} \times 100\% = 64.29\%$) of the deflection force when diffusion charging is considered, but does not have much effect on field charged particles. Note that the Brownian motion can influence the motion of particles, but does not necessarily define its motion as the time averaged force of Brownian

motion is equal to zero. It was therefore excluded from the deterministic deflection model calculations (see section 5.1).

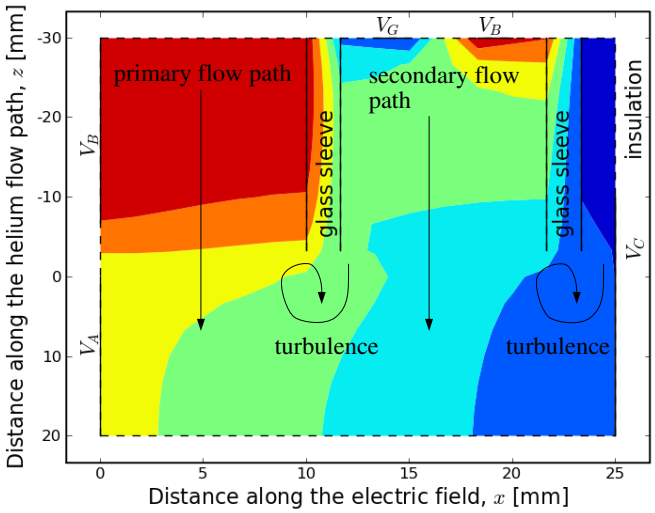

Figure 6.21: Electric potentials of x-y plane with deflection voltage of 500 V and breakdown voltage V_B of 900 V

A number of assumptions were made to simplify the calculations relating to the deflection of the silver particles. In the theoreticel model it is assumed that the the electric field remains constant throughout the y-axis. This is not the case, as the electric potentials in figure 6.21 is clearly not linear. This figure displays the variation in the electric field in the x-y plane. In the theoretical model it was assumed that the flow was fully developed laminar flow. In practice, fully developed laminar flow would only occur a way into the flow path. The flow through and around the glass sleeve, see figure 6.21, might influence the flight path of the particles. In the theoretical model particles are assumed to be charged up to their saturation charge and as this requires time, it might not always be the case in the experiments, as particles are not permanently in the ionization zone due to the flowing helium and an ac arc. In the theoretical model it was assumed that all the particles are spherical which is clearly not the case, as can be seen in figure 6.12 and table 6.2. It was also assumed that the particles are pure silver, which is not what is indicated in figure 6.13, as sodium, carbon and oxygen are also present. In the theoretical model it was also assumed that re-entrainment does not occur. In the experimental tests this assumption was found invalid as the width of the particles were always larger than the height, which can be explained by re-entrainment.

The comparison of the deterministic deflection model's theoretical values are compared with the experimental values and are shown in table 6.4. As observed in figures

6.5 and 6.6, larger particles collected on the anode, hence larger particles are charged positively while smaller particles are charged negatively. This observation was incorporated into the results as the field charged particles are collected on the anode while the diffusion charged particles collected on the cathode. The first column of table 6.4 is the voltage of the experimental test and the second column is the velocity of the experimental test. The experimental values were obtained from table 6.1 and are displayed in two columns, one for the 5 mm electrode and one for the 25 mm electrode. The theoretical values were obtained from the figures as stated in each cell, in some cases the 100 nm particles are excluded as they could receive charge from both charging mechanisms.

From table 6.4 it is clear that the deterministic deflection model provides favourable results when compared with the experimental results. In some cases the theoretical model had a high level of correlation with the experimental results, such as the 5 mm electrode of the 300 V test. The largest discrepancy between the experimental and theoretical results were when the theoretical results predicted that the particles would all plate-out at 140 mm, where they plated out at 70 mm, therefore giving an discrepancy of 50 %.

Table 6.4: Comparison of theoretical and experimental values

potential V	v_{He} [m/s]	experimental		theoretical	
		5 mm electrode	25 mm electrode	5 mm electrode	25 mm electrode
300	0.0184	80 mm	140 mm	80 mm figure 6.20(b)	100 mm figure 6.17(a)
-300	0.0191	90 mm	100 mm	140 mm figure 6.17(b)	80 mm figure 6.20(a)
500	0.0198	60 mm	140 mm	100 mm figure 6.18(b)	140 mm figure 6.15(a)
-500	0.0198	70 mm	60 mm	140 mm figure 6.15(b)	50 mm figure 6.18(a)
500	0.0317	90 mm	140 mm	140 mm figure 6.19(b)	110 mm figure 6.16(a)

6.4 Conclusion

This chapter discusses an experimental means of creating nano- to microparticles in a helium stream, whereafter they are deflected and deposited onto both deflection elec-

trodes. It was initially believed that the deflection of the nanoparticles was due to dielectrophoresis and this assumption was based on results obtained from chapter 4. With the use of an AFM it was found that some of these particles are microparticles. If silver microparticles are moving in a helium stream in a nonhomogeneous electric field, the dielectrophoresis approximation is valid and the deflection can be calculated. However, the deflection due to the dielectrophoresis force is far smaller than that which was experienced. Combining this with the fact that oxygen and carbon must have been in the plasma, an alternative hypothesis was proposed.

The alternative hypothesis suggests that particles are ejected from the surfaces of the electrodes in the ac arc discharge. The particles are then immersed in positive ion and/or electron clouds. These ejected particles increase their size by nucleation. Their charge is increased by field and/or diffusion charging, depending on the size of the particles. This hypothesis of bipolar charging is defended by a favourable comparison of with a 0 % descrepancy (theoretical vs experimental results) as shown in section 6.3. The largest error of 50 % necessitates more research be done, which is described in the following chapters, before an recommended model can be built.

Chapter 7

Discussions and conclusions

This chapter describes the thought process which was followed to achieve the objectives of this thesis as prescribed in chapter 1. The assumptions made and reasoning behind decisions taken are highlighted. The conclusions which were drawn during the exploration of particle deflection and plate-out dynamics are also summarised.

Cronje (2007) suggested that the deflection of ions in an electric field is more efficacious than the deflection of atoms in a magnetic field. The deflection would occur in helium. To investigate this phenomenon in more detail, an examination of silver ions sources in helium was needed. From the literature study, see chapter 2, the conclusion was drawn that no ion sources which can be used in helium of 90 bar could be found.

The creation of atoms at high pressure also presents a problem. Joule heating of the metal up to the required temperatures would be difficult, see appendix A.5. A possible solution of concentrating high energy on a small space could be achieved by use of laser ablation.

Nichols *et al.* (2000) successfully created silver nanoparticles by means of laser ablation of microparticles (LAM). They also deflected the particles by means of an electric field whereafter they plated out. This method was exactly what was required by the objectives. At this point the author was still unsure whether the particles would return to atom state due to recombination, see section 2.2. Experiments were attempted to conclude wether recombination would occur.

The first experiments which used microparticles, as described in chapter 4, was based upon Nichols *et al.* (2000)'s work. In these experiments it was found that some of the microparticles plated out onto the surface of the electrodes without the use of a laser. Dielectrophoresis (DEP) was proposed as a possible explanation. It was thought

that reducing the size of the particles might increase the deflection in a nonhomogeneous electric field. The creation of silver nanoparticles by means of a gas aggregation technique used by Mahoney and Andres (1995), which is explained in chapter 6, was attempted.

From the SXPS profiles of the arc discharge experiment, as described in chapter 6, it was found that not only silver and helium were present in the plasma. From this finding a hypothesis of bipolar charging was proposed. It was defended as particles plate-out with more efficacy than with DEP, which can be explained by field and diffusion charging. The arc discharge experiment can be called an electrostatic precipitator as particles were charged by the arc and subsequently plated out onto the deflection electrodes.

Equations (2.16) and (2.17) were used to calculate the charge on the particles. These equations require values for the electric field strength and the temperature, which are difficult to measure as both vary with time in the ac arc. The duration of this charging would also be indeterminable as the arc exists for too brief a period before it is extiguished, due to a lack of current produced by the flyback converter. The flyback converter was designed to create pulsed arcs. A constant arc would make measurements easier. Combined with the fact that the flow is not fully developed laminar flow and that the particles are not spherical, determining more accurate deflection would not be possible with the apparatus which was described in chapter 6. Re-entraiment was also never incorporated into the deterministic deflection model. Therefore further investigation into breakdown voltages, operating voltages, helium temperature, re-entrainment and charging time is required. Despite these problems, it can be concluded that the deterministic deflection model adequetely describes the deflection of the silver nano and microparticles therefore initial engineering design considerations for a scale model can be made.

From the literature study it is clear that after silver is vapourized in a gas environment it creates particles (clusters or even nanoparticles) due to homogeneous nucleation. Contradicting this, Bäumer (1990) stated that most of the released solid fission products are transported in their atomic or molecular form. Bäumer (1990) also stated that there are dust bound activities with a typical grain size of 0.76 μm diameter, which can easily be charged by means of field charging. Therefore further research is advised to determine whether the ^{110m}Ag which plated onto the primary circuit components (see chapter 1) was due to single atoms, ions, clusters, nano- or microparticles. After this research has been concluded, the correct charging technique can be designed for.

Chapter 8

Recommendations

This chapter proposes a method of electrostatic precipitation (ESP) where particles are charged in helium, whereafter they are deflected in an electric field. This technique would not only deflect silver, but any other particles as well (such as the grafite particles with a diameter of 0.76 μm, see chapter 7). Field and diffusion charging were used in chapter 6 to charge particles for subsequent deflection in an electric field. It is suggested that these mechanisms be used to meet the PBMR objective, see chapter 1. Both techniques are proposed as it is unclear which size range of particles would be present in the PBMR helium stream, see chapter 7. The charging should occur in an ionization zone, which should be created by a positive corona. The positive corona is advised as it produces a constant ionization zone and the positive particles (which will be created by Penning ionization and ion-atom collisions due to metastable and ionized helium as well as photo-ionizing of particles) will be attracted towards the collection electrode.

The charging transfer due to Penning ionization, ion-atom collisions and photo-ionization can also charge the radio-active particles, which are transported in their atomic and molecular form. It is believed that these particles would then attach themselves to larger particles by means of diffusion or field charging. Further investigation into this phenomenon is necessary as a means of removing atoms and molecules from the helium stream.

In the proposed PBMR the piping directly at the the exit of the reactor is 1173.15 K, which would create therminonic emission from the piping surface. It is therefore suggested that the helium be tapped off into a cooler section for scrubbing as the thermionic emission would cause a negative charge well, which would deter charged particles from plating out. This cooler section will be known as the deflection section.

There are a number of ways in which the electrodes can be placed in the deflection

section to create a corona for the charging of particles. In an attempt to reduce the pressure drop over the electrodes, a number of electrodes can be placed in parallel as shown in figure 8.1(a). Due to the different lengths of the plates a corona will be formed. The ionization zone can be seen in figure 8.1(b). The colour variations in this figure represents the electric field strength variations as a function of the maximum value of the electric field strength, blue being the smallest while red being the largest electric field strength. It is suggested that a computational fluid dynamic of this model and others should be created (one example would be the use of guide vanes in a bend as Crowe *et al.* (2001) stated that the loss coefficient in a mitre bend decreases from 1.1 to 0.2 with the use of guide vanes) in an attempt to reduce the frictional flow helium loss.

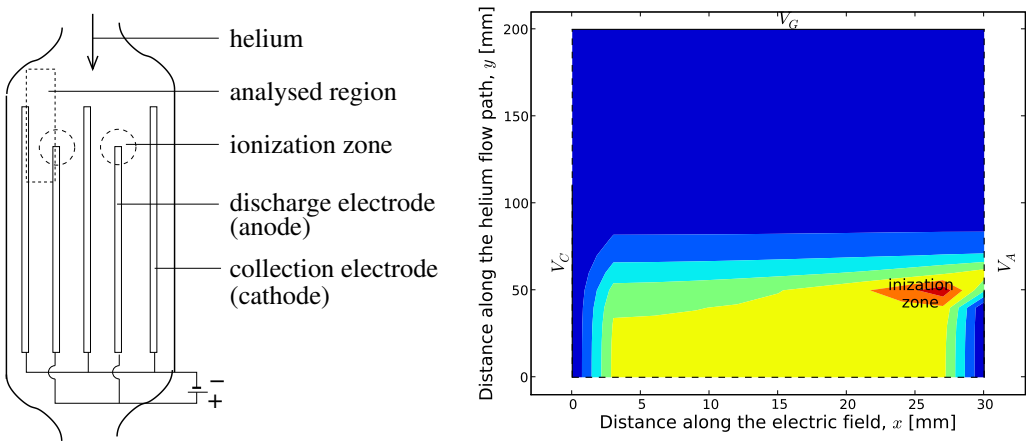

(a) Cascade of deflection electrodes (b) The electric field of the analysed region

Figure 8.1: Cascade of deflection electrodes in deflection section

A problem which will occur with the above mentioned solution is that electrostatic precipitator efficiency would decrease, as the plates cannot be cooled effectively and the ionization zone is small. A possible improvement which could be made is increasing the number of ionization zones by placing of a number of spherical electrodes between two collection electrodes on the side which can easily be cooled, see figure 8.2(a). However, this solution creates the problem of increased flow losses of the helium.

The entire suggestion is based upon the principle that the helium is ionized around the discharge electrode, and only around the discharge electrode. Impurities in the helium (which could include fission products) might influence the corona in such a way that breakdown between the anode and cathode might occur. Breakdown would eject atoms and clusters from the electrodes, thus increasing impurities in the helium as

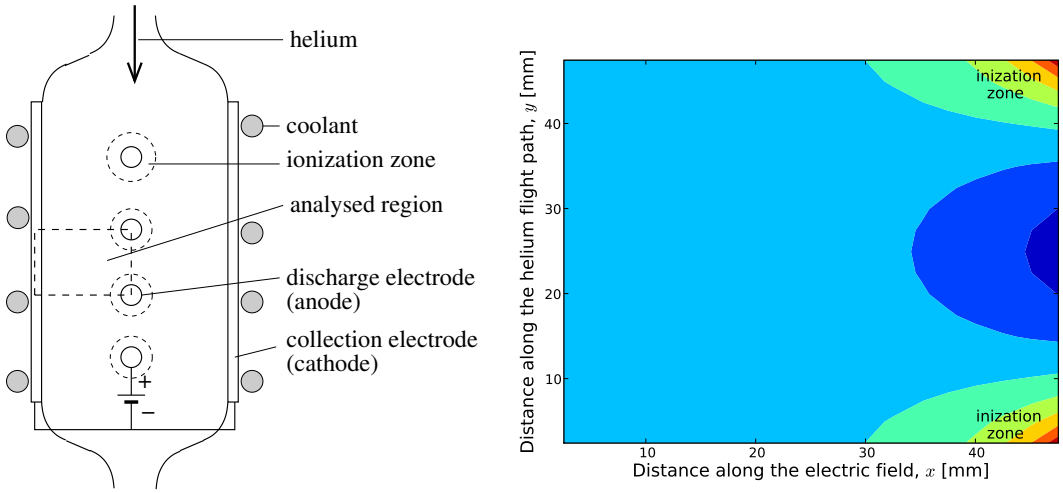

(a) Cascade of wires in the ESP

(b) The electric field of the analysed region

Figure 8.2: The wire and plate ESP

opposed to removing them. This ejection of particles would also decrease the surface of the electrodes. The arc which is formed would also be a waste of energy.

The exact voltage to be used is not known, because no information on electrostatic precipitation (ESP) at 90 bar was found. Paschen's law is not obeyed at very high pressures (see section 2.3) and the increased temperature influences the mean free path of the electrons (see equation (A.13)), thus the voltage breakdown equation used for low pressures and temperatures would not be valid. Another factor that might influence the breakdown voltage is the amount of impurities or fission products in the helium. Therefore, further investigation into breakdown and corona formation is required to accurately determine the required electric field for the charging of the particles.

If the electric field strength is known, the charge on the particles can be determined. After the charge is calculated, the length of the electrodes can be determined using the deterministic deflection model as described in section 5.1.

The temperature of the helium in the deflection section would most probably be influenced by the design parameters of the reactor. A scale model should be built, as suggested in chapter 7, which would validate the efficacy of plating out of particles at different temperatures.

Further investigation into the possible formation of negative ions due to halogens which are formed (Niu and Houk, 1996) because of fission products such as iodine (Sawa *et al.*, 2004) should be undertaken. Negative ions would be repulsed from the collection electrodes, thus decreasing the ESP's effectiveness.

Calculations can be made with the research findings and models presented in this thesis. Consider that the applied voltage between the two electrodes, of figure 8.2(a), is half that which is proposed by Pashen's law, which is equal to 108400 V over the 25 mm gap. Note that due to the nonhomogeneous electric field, the electric field will be greater in the areas around the discharge electrodes, creating a corona. The velocity of the helium can be decreased to 30 m/s by increasing the pipe diameter of the deflection section by twice the original size. The assumption is made that the temperature of this section is kept at 700 K (it is still not known whether this value would decrease the negative charge well enough to allow deposition of charged particles). Using these values for the electric field, temperature and helium velocity, the maximum charge on a 1 μm radius particle due to field charging is 1.45×10^{-15} C (calculated by means of equation (2.16)), while the maximum charge on a 10 nm radius particle is 1.008×10^{-19} due to diffusion charging (calculated by means of equation (2.17)). Using equation (5.15) and assuming that the dielectrophoresis force is negligible and that the deflection region's electric field is homogeneous, the velocity of the particle towards the collection electrode v_x can be calculated. The v_x for the field charged particle is 4.76 m/s while the v_x for the diffusion charged particle is 21.79 m/s. Therefore, the particles would reach the collection electrode at y equal to 0.1574 m ($30 \times 0.025/4.76 = 0.1574$ m $30 \times 0.025/21.79 = 0.03442$ m) and 0.03442 m. Therefore it is suggested to have a deflection flight path of at least 1 m, so as to ensure that partially charged particles, and those which have only been charged in the following ionization zones, also have the chance to deflect and plate-out.

It is thus recommended that a scale model of an ESP in helium at temperatures which can be varied be built. With this scale model, tests can be done to determine the uncertainties which have been highlighted in this chapter before the ESP can be implemented in the PBMR.

Appendix A

Sundry derivations from basic principles

This appendix is used to derive a number of equations using first order analysis or basic principles. The ideal gas law was used to determine the mean free path of molecules and electrons. These derived equations are used in chapter 3. The velocity profile between two flat plates was determined as the velocity profile varies in a duct and was needed in section 5.1. The dielectrophoretic derivation explains and motivates the assumptions made in deriving equation (2.9). The validity of the assumption, made in section 5.1, that particles reach their terminal velocity quickly was investigated. The vapour pressure of silver at various pressures was determined to ascertain whether it would be possible to emit silver as a gas by means of Joule heating. Finally, it was necessary to establish the breakdown of helium, given that this is essential to create an arc, see section 6.1.

A.1 Mean free path

The mean free path λ of molecules and electrons are determined in this section. The equations derived are used in the two deflection models as described in chapter 5.

A.1.1 Kinetic theory of gases

The kinetic theory of gases is used to determine λ in section A.1.3. The ideal gas law (Sears, 1964) explains the relationship between pressure p, volume V, absolute temper-

ature T and the number of moles n of the gas. It is expressed as

$$pV = nRT \tag{A.1}$$

A mole of any material will contain an Avogadro's number of molecules. Thus, the number of molecules per m^3 can be determined by the equation

$$N_m = \frac{nN_A}{V} \tag{A.2}$$

Equation (A.1) can be rewritten as $n = \frac{pV}{RT}$. If this is inserted into equation (A.2), it leads to

$$N_m = \frac{N_A P}{RT} \tag{A.3}$$

as the volumes cancel each other out. $\frac{R}{N_A}$ can be replaced by k_B, Boltzmann's constant. Hence, equation (A.3) can also be written as,

$$N_m = \frac{P}{k_B T} \tag{A.4}$$

A.1.2 Relative velocities

Due to Brownian motion each molecule's movement is relative to another molecule. Thus relative velocities have to be considered when working with velocities. If there are two molecules with velocities $\mathbf{v}_1$ and $\mathbf{v}_2$, the magnitude of their relative velocities can be expressed as

$$v_{rel} = \sqrt{\mathbf{v}_{rel} \cdot \mathbf{v}_{rel}} \tag{A.5}$$

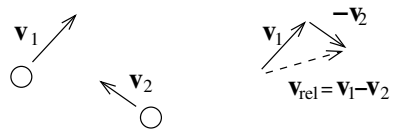

Figure A.1: Random molecular velocities

Inserting $\mathbf{v}_{rel} = \mathbf{v}_1 - \mathbf{v}_2$, as shown in figure A.1, into equation (A.5) leads to

$$v_{rel} = \sqrt{(\mathbf{v}_1 - \mathbf{v}_2) \cdot (\mathbf{v}_1 - \mathbf{v}_2)}$$
$$v_{rel} = \sqrt{\mathbf{v}_1 \cdot \mathbf{v}_2 - 2\mathbf{v}_1 \cdot \mathbf{v}_2 + \mathbf{v}_1 \cdot \mathbf{v}_2}$$

Taking the average,

$$\overline{v}_{rel} = \sqrt{\overline{\mathbf{v}_1 \cdot \mathbf{v}_2} - 2\overline{\mathbf{v}_1 \cdot \mathbf{v}_2} + \overline{\mathbf{v}_1 \cdot \mathbf{v}_2}} \tag{A.6}$$

but since $\mathbf{v}_1$ and $\mathbf{v}_2$ are random and uncorrelated, $\mathbf{v}_1 \cdot \mathbf{v}_2 = 0$ and when inserted into equation (A.6) leads to

$$\overline{v}_{rel} = \sqrt{\overline{\mathbf{v}}_1^2 + \overline{\mathbf{v}}_2^2} \tag{A.7}$$

since the average velocity is applicable to both molecules, this becomes

$$\overline{v}_{rel} = \sqrt{2}\,\overline{\mathbf{v}} \tag{A.8}$$

A.1.3 Mean free path of equally sized molecules

The mean free path λ is the distance travelled by a particle before striking a surrounding particles. If it is assumed that all molecules are spheres (with diameter d) and that collisions are perfectly elastic, the collision cross-section of the moving molecule can be calculated as

$$\sigma = \pi d^2 \tag{A.9}$$

It is assumed that inside a motionless gas a particle has a velocity v at any instance. In a time step t, the moving molecule travels a distance vt while colliding several times. If there are N_m molecules per unit volume, the number of collisions made per time step t is

$$\sigma N_m v t \tag{A.10}$$

The mean free path can be calculated as the distance travelled divided by the number of collisions during the time of travel, hence

$$\lambda = \frac{\overline{v}t}{\sigma N_m \overline{v}t} = \frac{1}{\sigma N_m} \tag{A.11}$$

Relative velocities are present and the particles are of equal size, hence $\overline{v}$ of equation (A.11) can be replaced with $\overline{v}_{rel}$ of equation (A.8). Replacing σ in equation (A.11) with equation (A.9) and N_m with equation (A.3) leads to

$$\lambda = \frac{RT}{\sqrt{2}\pi d^2 N_A p} \tag{A.12}$$

A.1.4 Electron mean free path

The radius of an electron can be ignored as it is very small. Thus, the centre-to-centre distance becomes $d/2$ instead of d. This leads to a σ of $\pi d^2/4$. Also, the velocity of an electron is much greater than that of an atom, thus the velocity of the atom is ignored. Taking these two assumptions into account leads to

$$\lambda_e = \frac{4RT}{\pi d^2 N_A P} \tag{A.13}$$

A.2 Velocity Profile

This section contains the derivation of the velocity profile used in section 5.1. It is based on a model proposed by Mills (1999) for a fully developed laminar flow velocity profile in a tube.

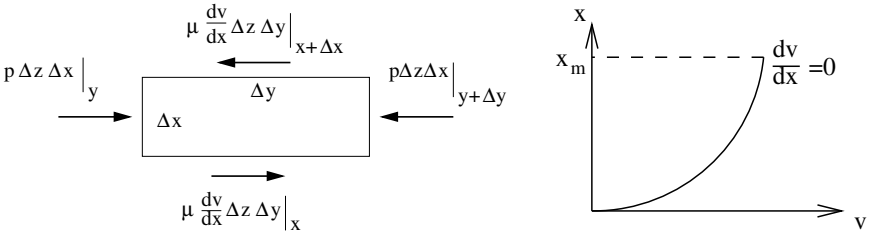

(a) Force balance on a fluid element (Mills, 1999)

(b) Parabolic velocity profile

Figure A.2: Velocity profile derivation figures

The force balance on the fluid element in figure A.2(a) is written as

$$p\Delta x\Delta z|_y - p\Delta x\Delta z|_{y+\Delta y} + \mu\frac{dv}{dx}\Delta z\Delta y|_{x+\Delta x} - \mu\frac{dv}{dx}\Delta z\Delta y|_x = 0 \tag{A.14}$$

Dividing equation (A.14) by $\Delta x\Delta y\Delta z$, letting Δx, $\Delta y \to 0$ and implementing Taylor's rule (Mills, 1999) leads to

$$\frac{\partial p}{\partial y} = \frac{\partial}{\partial x}\left(\mu\frac{\partial v}{\partial x}\right) \tag{A.15}$$

The two boundary conditions, see figure A.2(b), are known

$$x = x_m : \frac{dv}{dx} = 0 \tag{A.16}$$

$$x = 0 : v = 0 \tag{A.17}$$

In equation (A.16) x_m is the middle of the distance between the two deflection electrodes. As the boundaries are a mirror image around this centre, it is assumed that the velocity profile is also a mirror image around this centre. Integrating equation (A.15) and then applying the first boundary condition (equation (A.16)) to obtain the first constant

$$x\frac{\partial p}{\partial y} + C_1 = \mu\frac{\partial v}{\partial x} \tag{A.18}$$

$$C_1 = -x_m\frac{\partial p}{\partial y} \tag{A.19}$$

Integrating equation (A.15) a second time leads to

$$\frac{x^2}{2}\frac{\partial p}{\partial y} - x_m x\frac{\partial p}{\partial y} + C_2 = \mu v \tag{A.20}$$

In this case $C_2 = 0$ when the second boundary condition, equation (A.17), is implemented. Rewriting equation (A.20) leads to

$$v(x) = \frac{x_m^2}{2\mu}\left(-\frac{\partial p}{\partial y}\right)\left[\frac{2x}{x_m} - \frac{x^2}{x_m^2}\right] \tag{A.21}$$

The bulk velocity is the area-weighted average velocity (Mills, 1999) and can be determined by

$$v_b = \frac{1}{x_m \Delta z}\int_0^{x_m} v\Delta z dx \tag{A.22}$$

where Δz is the distance into the z-direction. The integration of that equation produces

$$v_b = \frac{1}{2\mu}\left(-\frac{\partial p}{\partial y}\right)\frac{2x_m^3}{2} \tag{A.23}$$

Inserting equation (A.23) into equation (A.21) and rearranging it gives a velocity profile as a function of the distance x from the surface of the plate as

$$v(x) = v_b\frac{3}{2}\left(\frac{2x}{x_m} - \frac{x^2}{x_m^2}\right) \tag{A.24}$$

A.3 Dielectrophoresis derivations

This section is used to determine the effective dipole moment acting on a spherical particle. This derivation was obtained by Jones (1995) and provides a better understanding of the physics behind dielectrophoresis. If a spherical particle of silver with

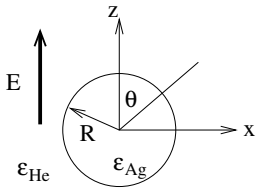

Figure A.3: Spherical silver particle of radius R and permittivity ε_{Ag} immersed in helium and subjected to a uniform electric field (Jones, 1995)

radius R and permittivity ε_{Ag}, see figure A.3, is placed in helium with a permittivity ε_{He} and is subjected to a homogeneous electric field E, the charge distribution within the particle will vary. If the assumption is made that the charge of nearby particles does not influence the charge distribution, the electric potential outside ϕ_1 and inside ϕ_2 the particle can be determined.

$$\phi_1(r,\theta) = -Ercos\theta + \frac{Acos\theta}{r^2} \quad , r > R \tag{A.25}$$

$$\phi_2(r,\theta) = -Brcos\theta \quad , r < R \tag{A.26}$$

where θ and r are the polar coordinates. The first term of equation (A.25) is the imposed uniform electrostatic field. The second term is the particle's induced dipole charge. The electric potential is the same at the surface, which leads to the boundary value of $\phi_1(r = R,\theta) = \phi_2(r = R,\theta)$. Applying this boundary condition to equations (A.25) and (A.26) leads to

$$-Ercos\theta + \frac{Acos\theta}{r^2} = -Brcos\theta \tag{A.27}$$

The flux density is defined as the density of the flux lines passing through a specific point (Taylor and Secker, 1994), it must be continuous across a boundary which leads to (Jones, 1995)

$$\varepsilon_{He}\frac{-\partial\phi_1}{\partial r} = \varepsilon_{Ag}\frac{-\partial\phi_2}{\partial r} \tag{A.28}$$

Inserting this into the differentiated form of equations (A.25) and (A.26) leads to

$$\left(-Ecos\theta + \frac{2Acos\theta}{r^3}\right)\varepsilon_{He} = \varepsilon_{Ag}(-Bcos\theta) \tag{A.29}$$

Solving equations (A.27) and (A.29) simultaneously leads to the factor $A = \frac{\varepsilon_{Ag} - \varepsilon_{He}}{\varepsilon_{Ag} - 2\varepsilon_{He}} R^3 E$. An effective dipole moment obtained from Jones (1995) is

$$m_{ef} = 4\pi\varepsilon_{He} A \tag{A.30}$$

Inserting the factor A into equation (A.30) while letting $K_{CM} = \frac{\varepsilon_{Ag} - \varepsilon_{He}}{\varepsilon_{Ag} - 2\varepsilon_{He}}$ leads to the effective dipole moment given by

$$m_{ef} = 4\pi\varepsilon_{He} K_{CM} R^3 E \tag{A.31}$$

A.4 Terminal velocity

This section is used to determine the terminal velocity and time needed for a particle subject to a constant acceleration to reach its terminal velocity. The terminal velocity of the particle is used in the calculational procedure in section 5.1.

If a particle experiences a constant acceleration, for example gravitational acceleration, it accelerates and the drag force increases as the velocity increases. This increase occurs until the particle reaches terminal velocity where the drag force is equal to the acceleration force (Crowe *et al.*, 2001).

Replacing the applied force in the Langevin equation (equation (5.13)) with a gravitational acceleration minus the hydrodynamic drag force leads to

$$m_p \frac{dv_p}{dt} = F_g - F_H \tag{A.32}$$

If the assumption is made that the Reynolds number is less than 0.5, Stokes drag froce can be assumed, see equation (5.3). The time the particle takes to reach a drag force of 95 % of the gravitational force can be calculated by rearranging equation (A.32) and integrating

$$\frac{m_p}{6\pi\mu R} \int_0^{\frac{0.95F_g}{6\pi\mu R}} dv_p = \int_0^{t_t} dt$$

where t_t is the time neccesary for the particle's drag force to reach 0.95 % of its accelerational force or in other words, the time required to nearly reach terminal velocity. This leads to

$$t_t = 3\frac{m_p}{6\pi\mu R} \tag{A.33}$$

Table A.1: Values of t_t for different particle radii

R	t_t
2 nm	1.40357919 ns
20 nm	140.357919 ns
200 nm	0.140357919 μs
3 μm	3.15805319 ms

According to equation (A.33) t_t is not influenced by the magnitude of the force. A few values of t_t are tablulated in table A.1.

A.5 Vapour pressure of silver

When the vapour pressure of a liquid equals the external pressure, the liquid escapes vigorously into the surroundings (Atkins, 1998) and is termed boiling. This is important as the silver would vapourize at the vapour pressure temperature. The Clausius-Clapeyron equation for the variation of vapour pressure with respect to temperature can be expressed as (Atkins, 1998)

$$p_v = p_v^* \exp \frac{\Delta_{vap} H}{R} \left(\frac{1}{T} - \frac{1}{T^*} \right) \tag{A.34}$$

where p_v^* is the vapour pressure at the temperature T^*, p_v is the vapour pressure at T,

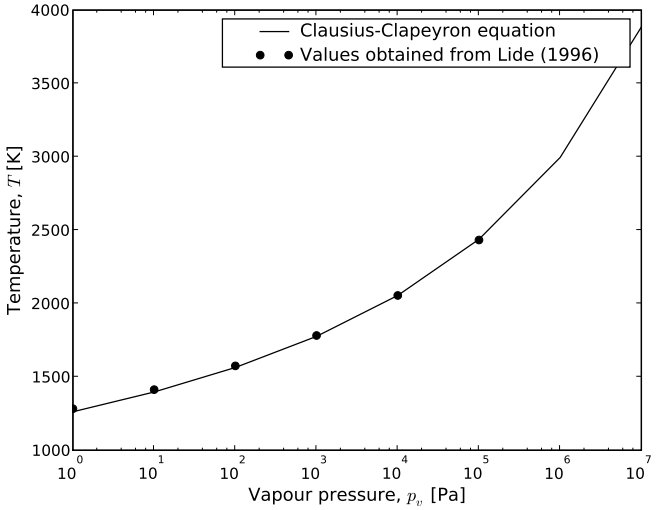

Figure A.4: Vapour pressure of silver

R is the gas constant and $\Delta_{vap} H$ is the entropy of vapourization. Rearranging equation

(A.34) leads to

$$\frac{1}{T} = \frac{R}{\Delta_{vap}H}\ln\left(\frac{p_v}{p_v^*}\right) + \frac{1}{T^*} \tag{A.35}$$

The vapour pressure vs temperature of equation (A.35) is shown in figure A.4. Note that this is only an approximation but, as it is possible to see from figure A.4, known values (obtained from Lide (1996)) coincide with equation (A.35). The trend only continues until the critical temperature T_c, however there are no reliable estimates of T_c for silver, according to Lide (1996).

Equation (A.35) was used to calculate the vapour pressure temperature of silver at 90 bar, $1/(\frac{8.314\text{J/molK}}{250.58\times10^3\text{J/mol}}\ln\frac{9000000}{10000} - \frac{1}{1782.+273.15})$ = 3833.0967 K. The values for p^* and T^* were obtained from Lide (1996). As this would be rather diffucult to achieve with Joule heating, alternatives to Joule heating were investigated in chapter 2.

A.6 Voltage breakdown

Applying a voltage greater than the breakdown voltage V_B between two electrodes creates a discharge. Scütze *et al.* (1998) derived the breakdown voltage for a gas as

$$V_B = \frac{pd_{es}B}{\ln(pd_{es}A) - \ln\left[\ln\left(1+\frac{1}{\gamma}\right)\right]} \tag{A.36}$$

where p is the gas pressure in Pa, d_{es} is the electrode spacing in cm and γ is the secondary electron emission coefficient. Equation (A.36) was obtained by taking $\alpha = pA\exp(-Bp/E)$, where A and B are constants which are found experimentally. In the case of helium A and B are 8 and 16, respectively (Bondeson *et al.*, 2002) if

$$\alpha = pA\exp\left(-\frac{B\sqrt{p}}{\sqrt{E}}\right) \tag{A.37}$$

Hence, equation (A.36) is not valid for the values of A and B previously mentioned and a new Paschen's curve has to be derived.

In establishing the new Paschen's curve the first step is to divide Townsend's criterion, equation (2.2), by γ and then taking the ln on both sides

$$\exp(\alpha d_{es}) = 1 + \frac{1}{\gamma}$$
$$\alpha d_{es} = \ln\left(1+\frac{1}{\gamma}\right)$$

Replacing α with equation (A.37) produces

$$Apd_{es}\exp\left(-\frac{B\sqrt{p}}{\sqrt{E}}\right) = \ln\left(1+\frac{1}{\gamma}\right)$$
$$\exp\left(-\frac{B\sqrt{p}}{\sqrt{E}}\right) = \frac{\ln\left(1+\frac{1}{\gamma}\right)}{Apd_{es}}$$

Taking the ln on both sides whereafter rearranging leads to

$$-\frac{B\sqrt{p}}{\sqrt{E}} = \ln\left[ln\left(1+\frac{1}{\gamma}\right)\right] - \ln(Apd_{es})$$
$$E = \frac{B^2 p}{\left(\ln(Apd_{es}) - \ln\left[\ln\left(1+\frac{1}{\gamma}\right)\right]\right)^2}$$

If the electric field is ussumed to be constant, $E = \frac{V_B}{d_{es}}$ which leads to

$$V_B = \frac{pd_{es}B^2}{\left(\ln\left(pd_{es}A\right) - \ln\left[\ln\left(1+\frac{1}{\gamma}\right)\right]\right)^2} \tag{A.38}$$

It should be noted that γ only influences the voltage breakdown of helium at low values of pd_{es}. Therefore, the value obtained from Lide (1996) of γ = 1 for aluminium becomes superfluous, which supports claims made by Howatson (1965), see section 2.3. The value of 1 used for γ is also not the correct values as it is based upon electrons with a certain value, which is not the case in the experiments of chapters 4 and 6. It was necessary to ascertain the breakdown values as they were used in the design

Table A.2: Values of V_B for different d_{es} with p of 2 bar

d_{es} [mm]	V_B [V]
0.5	473.404
1	771.123
5	2562.926
10	4398.245
25	9033.189
1000	195979.048

procedures as described in sections 4.1 and 6.1. The necessary breakdown voltages at different electrode spacing distances are displayed in table A.2.

Appendix B

Orifice flow meter

A manometer was used to measure the pressure difference across an orifice in order to calculate the flow rate of the helium. The decision to use an orifice was based on convenience, as it is easily manufactured. The design of the flow meter and the determination of its flow-coefficient K are described in the following two sections, respectively. As K varies for different mass flow rates it is necessary to determine it for the desired mass flow rates.

B.1 The design of the orifice flow meter

This section is used to determine the orifice diameter of the orifice flow meter. This was done by determining the mass flow rate of the apparatus as describe in chapter 4 and using it to determine the orifice diameter.

The conservation of energy equation is applied across the entrance 1 and exit 2 of the primary flow path, shown in figure 4.2(b). The conservation of energy can be expressed as

$$\rho\frac{\dot{W}}{\dot{m}} = (p_2 - p_1) + \rho\frac{v_2^2 - v_1^2}{2} + \rho g(z_2 - z_1) + \rho(u_2 - u_1) \quad \text{[Pa]} \tag{B.1}$$

where $\dot{W}$ is the work done by the system, $\dot{m}$ is the mass flow rate, p_1 and p_2 are the pressures at the entrance and exit, respectively. The density of the gas ρ is assumed to be constant over the entire system. v_1 and v_2 are the velocity of the gas flowing at the entrance and the exit respectively and v_1 was taken as zero. The height difference $(z_2 - z_1)$ was also ignored. The change in the specific internal energy of the gas can be

expressed as

$$\rho(u_2 - u_1) = \sum_i \rho k_i \frac{v_i^2}{2} \tag{B.2}$$

where k_i is the loss coefficient for each individual element of the system and v_i is the velocity of the gas at the element i. The loss coefficient k used for each individual element is indicated in table B.2. The continuity equation is

$$v_p A_p = v_{ves} A_{ves} \tag{B.3}$$

where v_p and v_{ves} are the velocities of gas in the pipe and the vessel while A_p and A_{ves} are the cross-sectional areas of the same elements. Combining equations (B.1) and (B.2) with (B.3) produces

$$0 = p_2 - p_1 + \rho \frac{v_2^2}{2} \left(1 + \sum k_i + \sum \frac{f_i l_i}{d_p} + \frac{A_p}{A_{ves}} \frac{f_v l_v}{d_h} \right) + \Delta p_8 \tag{B.4}$$

where Δp_8 is the pressure drop over the filter. The manufacturer of the filter (Swagelok) supplied values of flow rates for specific pressure drops, which can be seen in table B.1.

Table B.1: The pressure drop vs flow rate of the filters manufactured by Swagelok

pressure drop	flow rate	
Δp [bar]	$\dot{m}$ [l/min]	$\dot{m}$ [kg/s]
0.34	1.1	3.098×10^{-6}
0.68	1.7	4.799×10^{-6}
1.00	3.4	9.576×10^{-6}

Python's polyfit function was used to determine the second order equation of the pressure drop over the filter from the values displayed in table B.1.

$$\Delta p_8 = 4.908 \times 10^{-6} - 1.047 \times 10^{-10} \dot{\mathrm{m}} + 1.51 \times 10^{-15} \dot{\mathrm{m}}^2 \tag{B.5}$$

The friction coefficients of each element, f_i in equation (B.4), were calculated using $f_i = 64/Re$ where Re is the Reynolds number which is valid for laminar flow according to Crowe *et al.* (2001). Equation (B.4) was used iteratively with varying pressures to obtain a mass flow rate of 3.884x10^{-5} kg/s. This value is plotted as a horizontal line in figure B.1. This mass flow rate leads to a Reynolds number of 139.35, which is less than the critical value of 2000. The assumption of laminar flow is thus correct. The loss

coefficients and element lengths, from table B.2, were used, with Δp the pressure loss for each element.

Table B.2: The loss coefficients of the elements in the primary flow path

Name	Position	k	l [m]	Δp [Pa]
Δp_1	Orifice	1.5		10256
Δp_2	Pipe		0.08	15
Δp_3	Y-section	0.4		0
Δp_4	Pipe		0.04	7
Δp_5	Expansion	1.0		1
Δp_6	Test vessel		0.50	54
Δp_7	Contraction	0.5		0
Δp_8	Filter			188260
Δp_9	Needle valve	10		16
Δp_{10}	Pipe		1.0	191
Δp_{11}	Expansion		1.0	1

Crowe *et al.* (2001) showed that the flow rate of gas can be calculated for an orifice by use of the equation

$$Q = Y_c K A_{or} \sqrt{2g\Delta h} \tag{B.6}$$

where Y_c is the compressibility factor, which was taken as 1 for incompressible flow was assumed, A_{or} is the area of the orifice and K is the flow coefficient taken as 0.58.

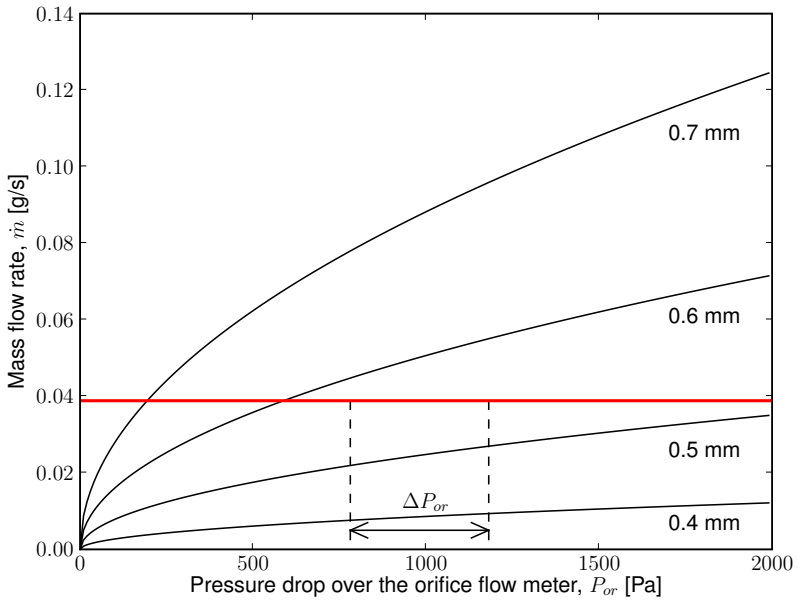

Figure B.1: The pressure drop vs flow rate for various sizes of the orifice

This value was obtained from Crowe *et al.* (2001). As there is a density difference between the air flowing over the orifice and the water in the measuring tube, the following equation is used

$$\Delta h = H\left(\frac{\rho_w}{\rho_g} - 1\right) \tag{B.7}$$

ρ_w and ρ_g are the densities of water and air, respectively and H is the height difference of the manometer. These values were taken at 20°C. Equation (B.6) is multiplied by the denisty to obtain the mass flow rate, which is plotted for different orifice diameters in figure B.1.

A value of 100 mm was used for H as this would be a easily readable value. The equation $P_{or} = (\rho_w - \rho_g)gH$ was used, (1000-0.1789)9.81×0.1 = 980 Pa, to calculate the designed pressure drop over the orifice. An allowable variation in the designed pressure drop over the orifice ΔP_{or} of ± 200 Pa is designed for. ΔP_{or} can be seen in figure B.1.

From the design requirements shown in figure B.1 and due to drill bit diameter constraints an orifice flow manometer of 0.5 mm was manufatured. In this section the flow coefficient of the orifice was taken as 1.5 (0.5 for contraction plus 1 for expansion). The flow coefficient varies for different flow rates, which was experimentally determined in the next section.

B.2 Orifice flow meter flow-coefficient determination

As previously mentioned, this section is used to calculate the flow coefficient for the orifice flow meter for different gas flow rates.

Water flowing into the measuring bucket under the influence of gravity creates a suction force which allows air to be drawn through the orifice, see figure B.2. The flowing air creates a pressure drop over the orifice which can be seen by the varying height of water H in the measuring tube. The volume V of water flowing into the measuring bucket is controlled by a needle valve and to ensure that varying pressure in the tank does not affect measurements, the measurements were only taken after H reached a steady state value.

The time t, the measuring bucket's volume as well as H were recorded and are shown in table B.3. It was found that for this specific setup, values for H smaller than 50 mm were difficult to measure as H osscilates. This is due to the variation in the pressure of the air in the tank. This is also a contributing factor to the values varying from the

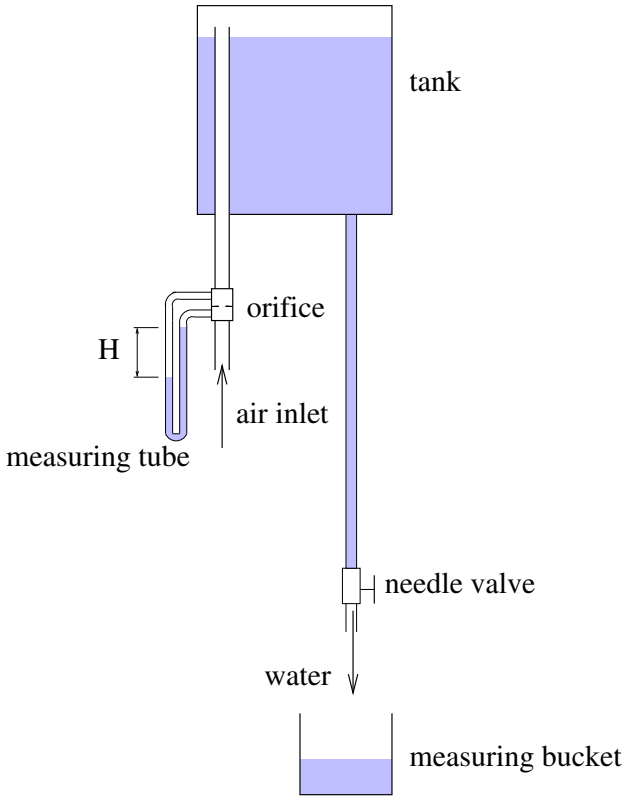

Figure B.2: Apparatus used to calculate the flow coefficient

Table B.3: The flow coefficient values

Test no	V [ml]	t [s]	H [mm]	Q_{exp} [dm^3/s]	K	error
1	1000.0	165.0	91.44	6.0606	0.7996	0.0259
2	1000.0	145.0	127.0	6.8966	0.772	0.0759
3	1000.0	328.0	27.94	3.0488	0.7276	0.0171
4	1000.0	211.0	58.42	4.7393	0.7822	0.0078
5	1000.0	180.0	73.66	5.5556	0.8166	0.0047
6	1000.0	155.0	106.68	6.4516	0.788	0.048
7	1000.0	60.0	558.8	16.6667	0.8895	0.2204
8	7224.0	420.0	584.2	17.2	0.8977	0.2264
9	1000.0	176.0	81.28	5.6818	0.7951	0.0203
10	600.0	229.0	20.32	2.6201	0.7333	0.0
11	1000.0	69.0	444.5	14.4928	0.8672	0.1844
12	1000.0	63.0	495.3	15.873	0.8998	0.1888
13	1000.0	109.0	190.5	9.1743	0.8386	0.0704
14	1000.0	102.0	203.2	9.8039	0.8677	0.0582
15	1000.0	73.0	355.6	13.6986	0.9164	0.1139

plotted graph, see figure B.3. The experimental flow rate Q_{exp}, which is displayed in table B.3, was calculated by dividing V by t.

Inserting equation (B.7) into equation (B.6), where the theoretical flow rate Q was replaced by the experimental flow rate Q_{exp}, leads to

$$Q_{exp} = Y_c K A_{or} \sqrt{2g\Delta h} \tag{B.8}$$

Rearranging this leads to the flow coefficient

$$K = \frac{Q_{exp}}{Y_c A_{or} \sqrt{2gh_d(\frac{\rho_w}{\rho_g} - 1)}} \tag{B.9}$$

which is displayed in table B.3. Y_c was taken as 1, see section B.1. The error column in table B.3 is the difference between this value and the one calculated by using equation (B.9).

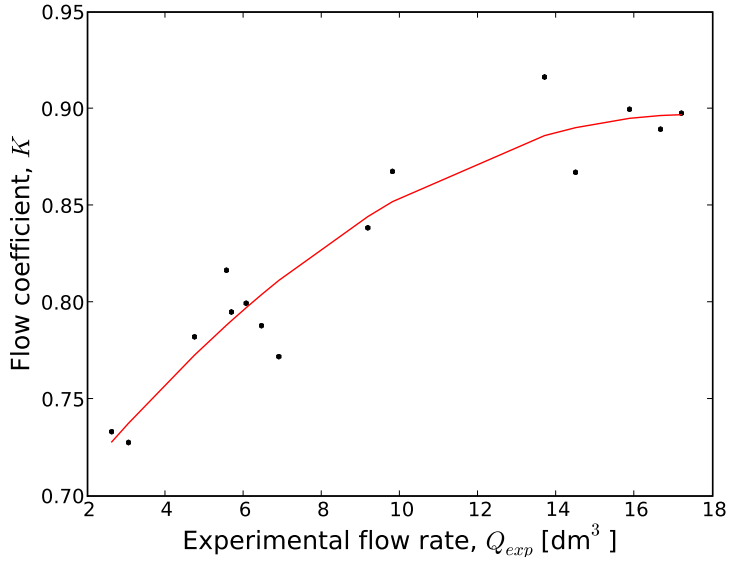

Figure B.3: Flow coefficient K vs the experimental flow rate Q_{exp}

Python's polyfit function (van Rossum, 2008) was used to determine a second order equation from the flow coefficient results shown in table B.3

$$K = 0.6629755 + 0.02681443Q_{exp} - 0.00076798Q_{exp}^2 \tag{B.10}$$

Equation (B.10) and the flow coefficient values of table B.3 are plotted in figure B.3. The flow coefficient K given by equation (B.10) was used in equation (B.6), which was used in chapters 4 and 6.

Appendix C

Safety and operational procedures

The safety and operational procedures of the three experiements (as described in chapter 4 and 6) are presented in this appendix. The safety procedures are valid for all three experiments, namely the two microparticle tests and the arc discharge test, while two separate operational procedures are given for the microparticle and arc discharge tests.

C.1 Safety procedures

All safety procedures, as stipulated by the Mechanical and Mechatronic Engineering Department for work in laboratories, were adhered to. A safety/hazard analysis was performed to indetify possible dangers of the experiments. A hazard can be defined as a possible source of danger which might influence the safety of personnel and equipment. In this section the potential hazards as well as their impacts are discussed and preventative measures which can be taken to minimise the hazards are discussed. In this chapter hazards are catogorized according to their impact.

Catastrophic hazard

- The high voltage power supply can create an electrical shock which can be deadly. This can be prevented by ensuring that the voltage supply is properly connected.
- Inside the voltage supply there are capacitors which store energy which can also create an electrical shock. This energy is only released when a short circuit is created between the two electrodes.

Critical hazard

- The test vessel can fail, which could lead to serious injury and damage to the equipment. A hydrostatic pressure test was done at 7 bar and the safety relief valve was set at a cracking pressure of 6 bar to protect against vessel failure.
- The helium supply should not be opened too quickly as this can cause the water in the manometer to spill. It is a well known fact that contact between electricity and water can have serious implications.

Marginal hazard

- The helium supply bottle can fall over and cause damage to the equipment. A preventative measure is to secure the bottle against the wall of the building with a chain.
- The deflection voltage may not create an arc as this can damage the oscilloscope and transistor in the breakdown voltage supply. The voltage applied should be less than 2.5 kV, see section 4.1.

Negligible hazard

- There could be a loss of helium due to the pipe connections not sealing, which can be prevented by ensuring that the piping is connected properly.
- The loss of silver, which is seen as a negligible hazard, can be reduced by the use of a filter at the end of the helium flight path.

C.2 Operational procedures for the microparticle tests

This is the procedure which was used in the microparticle tests. Both experiments as described in chapter 4 are operated by these procedures.

Setup procedures

- The insulation, voltage feedthroughs, quartz window and sight glass are to be connected as seen in figure 4.2 or figure 4.3, depending on the test.
- Measure the weight of each removable element (the three cathodes, the three anodes, the undeflected collecting plate, the bottom filter and either the mixing chamber or the section of the secondary flow path including the neede valve and the filter). Hereafter place the removable elements in their positions in the apparatus, see figure 4.2 or figure 4.3, depending on the test.
- Connect the vessel to the stand.

- The valves, piping, filters and connections of the apparatus are to be set up as indicated in figure 4.2 or figure 4.3.

Pretest check

- Ensure that the bottle is secured to the wall, ensure that all helium connections have been secured and open the laboratory window for ventilation.
- Ensure that all the electric connections are correctly connected.

Test Procedure

- Disconnect the secondary flow section (figure 4.2) from the main apparatus and insert a sample of silver between the filter and the shut-off valve. Purge the secondary flow section by connecting the shut-off valve to the helium tank via the pressure reducing valve. After the secondary flow section has been purged, close the two valves and connect them to the apparatus. In the mixing chamber test, this is ignored as the mixing chamber is inside the vessel.
- Purge the apparatus by connecting the pressure reducing valve to the system and allow helium to pass through the system. Helium is lighter than air, thus the helium will force all of the air from the apparatus through the exit at the bottom.
- Adjust the flow by changing the inlet pressure (by means of the pressure regulating valve) and adjust the needle valves.
- Switch on the voltage supply and adjust it to the required voltage.
- Open the secondary tube, by first opening the needle valve and then opening the shut-off valve.
- Run the test for the required time.
- Switch off the test in the following order: turn off the voltage supply and then turn off the helium supply at the bottle.
- Disconnect the voltage suppy from the apparatus and create a short circuit between the two electrodes.
- Remove the test vessel from the apparatus and remove the sight glass. Carefully remove the collecting electrodes and measure the weight of the elements mentioned. If needed, view under a microscope.

C.3 Operational procedures for the arc discharge test

These are the operational procedures used in the arc discharge test. The setup of this test is described in chapter 6.

Setup procedures

- Connect the two silver discharge electrodes to the electrode holder. Then connect the cover glass to the holder. Bolt the holder to the test vessel and connect the electrode to the top feedthrough.
- Secure the glass slide between the two electrodes on the insulator. Place the insulator in the vessel. Connect the two electrodes to the bottom feedthroughs. Connect the sight glass and bolt the lid to the test vessel.
- Secure against stand and connectthe helium pipe connections, pressure relief valve and orifice with manometer.
- Connect the discharge and deflection voltage sources.

Pretest checks

- Ensure that the bottle is secured to the wall, ensure that all helium connections have been secured and open the laboratory window for ventilation.
- Ensure that all the electric connections are correctly connected.

Test procedures

- Slowly open the pressure reducing valve and adjust the needle valves to obtain the required helium velocity.
- Switch on the high voltage supply. Check that there are no arcs between the deflection electrodes inside the vessel.
- Turn on the signal generator and the low voltage supply. Check that breakdown occurs between the arc discharge electrodes. Run the test for the required time.
- To discontinue the test, turn off the low voltage supply, the signal generator and the high voltage supply.
- Close the needle valves and the pressure reducing valve.
- Carefully remove the anode from the high voltage supply, only touching the insulated material. Make contact with the cathode. This will remove residual charge

stored in the capacitors of the voltage supply. Only then remove the cathode from the feedthrough. Do the same with the discharge electrodes.

- Remove the helium connections. Remove the test vessel from stand the and unbolt the lid.
- Carefully remove the insulator with glass slides and discharge electrodes and investigate the electrodes under a microscope.

Appendix D

Sample calculations

This appendix elaborates on the two deflection models, described in sections 5.1 and 5.2, as it contains the step by step numerical implementation of the models. Section D.1 contains the sample calculations using the deterministic deflection model to deflect a silver microparticle with the use of dielectrophoresis. Section D.2 contains the sample calculations using the stochastic deflection model to deflect a silver ion in a homogeneous electric field in helium.

D.1 Deterministic deflection model

This section contains a sample calculation of the deterministic deflection model as described in section 5.1. This deflection model is used to simulate the the experimental setup as described in section 4.2 by calculating the deflection of a silver particle with a radius of 3 μm in a nonhomogeneous field. Dielectrophoresis, drag and gravitational forces are are assumed to be the only forces acting on the particle.

As described in section 5.1 the x-z cross-section is divided into 31 N_x elements and 31 N_z elements. Thus H (see figure 5.2) is calculated as 0.8333 mm by solving 25 mm$/(N_x - 1)$ whereas l was calculated as 1.6667 mm by solving 50 mm$/(N_z - 1)$. A positive voltage of 500 V is applied to the two electrodes, which implies that V_C is taken as -1 V while V_A is taken as 500 V. The potential of -1 V, rather than 0 V, is used as the implementation of this Neumann boundary value is far simpler. The electric potential matrix is started at 0 and increases for each individual iteration. The electric potential values only change if they are not equal to -1 or 500.

Using the same methodology as Lindfield and Penny (2000), the one dimensional solu-

tion was converted into its two dimensonal equivalent given by equation (5.7). Equation (5.6) was converted to

$$\nabla\phi = \frac{r^2\phi_l + r^2\phi_r + \phi_a + \phi_b}{2(1+r^2)} \tag{D.1}$$

where $r = l/H$ = 2. In the case of a Neumann boundary condition on the left hand side, equation (D.1) becomes

$$\nabla\phi = \frac{r^2\phi_r + \phi_a + \phi_b}{2+r^2} \tag{D.2}$$

Table D.1: Some electric potentials after 1000 iterations

	i = 0	i = 1	i = 2
k = 5	64.5748 V	65.5445 V	67.3764 V
k = 4	72.5929 V	73.2500 V	74.5268 V
k = 3	78.1503 V	78.6469 V	79.6228 V

Table D.1 represents a number of electric potentials after 1000 iterations. Note that i and k refer to the control volume number in the x and z directions, respectively. Using equation (D.2) the next ϕ[k][i], where k = 4 and i = 0, can be calculated

$$\frac{2^2 \times 73.2500 + 64.5748 + 78.1503}{2+2^2} = 72.6272 \text{ V}$$

while using equation (D.1) ϕ[4][1] can be calculated

$$\frac{2^2 \times 72.5929 + 2^2 \times 74.5268 + 65.5445 + 78.6469}{2(1+2^2)} = 73.2845 \text{ V}$$

The process is repeated until the maximum difference between each individual element of the electric potential matrix and the electric potential matrix calculated after it, is smaller than 10^{-6}. Convergence of the boundary values and electric potential matrix size used in this section was obtained after 5982 iterations. The electric potential contours have been plotted by Python's contour function (van Rossum, 2008) in figure D.1. It is important to note that the electric field is symmetrical around z = 25 mm as the boundary conditions are mirror images around this line.

As few particles move through the area covered in table D.1 an area of more influence was used for the rest of the calculations. The results of the electric potentials of such an area after convergence are displayed in table D.2.

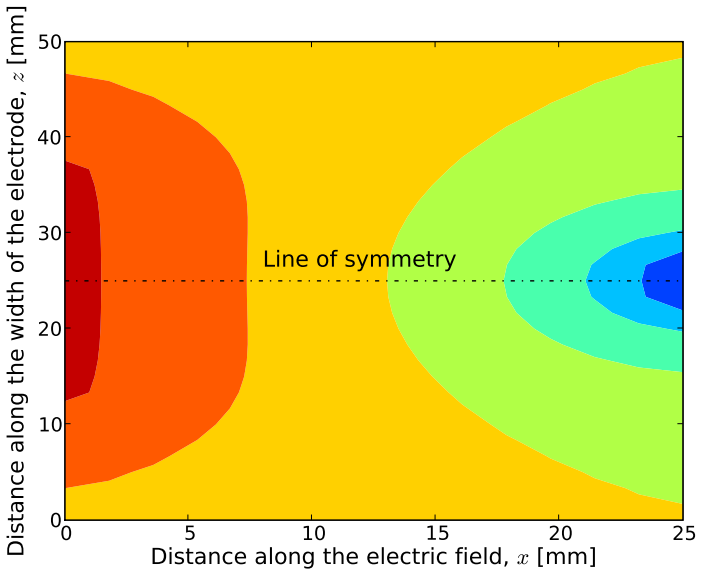

Figure D.1: The contours of electric potentials

Table D.2: Some electric potentials after convergence

	i = 5	i = 6	i = 7
k = 16	53.8943 V	64.7720 V	75.6205 V
k = 15	53.8421 V	64.7356 V	75.6108 V
k = 14	53.8943 V	64.7720 V	75.6205 V

The various components of ∇E^2, as described in equation (5.9), were calculated by using equations (5.6), (5.7) and (5.10). As the three previously mentioned equations are only applicable to variations in the x direction, a new set was developed in the z direction and implemented.

$$E_x[15][6] = \frac{-53.8421 + 75.6108}{2 \times 0.0008333} = 13061.1762 \text{ V/m}$$

$$E_{xx}[15][6] = \frac{53.8421 - 2 \times 64.7356 + 75.6108}{0.0008333^2} = -26238.3455 \text{ V/m}^2$$

$$E_z[15][6] = \frac{64.7720 - 64.7720}{2 \times 0.0016667} = 7.8442 \times 10^{-5} \text{ V/m}$$

$$E_{zz}[15][6] = \frac{64.7720 - 2 \times 64.7356 + 64.7720}{0.0016667^2} = 26238.8669 \text{ V/m}^2$$

$$E_{xz}[15][6] = \frac{75.6205 - 53.8943 - 75.6205 + 53.8943}{4 \times 0.0008333 \times 0.0016667} = -0.01395 \text{ V/m}^2$$

$$E_{zx}[15][6] = \frac{75.6205 - 75.6205 - 53.8943 + 53.8943}{4 \times 0.0008333 \times 0.0016667} = 0.01395 \text{ V/m}^2$$

Using equations (5.11) and (5.12) the dielectrophoretic force can be calculated as

$$\begin{aligned} F_{DEP,x}[15][6] &= 4\pi(1.000065 \times 8.85418 \times 10^{-12}\text{F/m})(3 \times 10^{-6}\text{m})^3 \times \\ &\quad \Big(13061.1762 \times (-26238.3455) + 7.8442 \times 10^{-5} \times 0.01395\Big) \\ &= -1.0296 \times 10^{-18}\ \text{N} \\ F_{DEP,z}[15][6] &= 4\pi(1.0000650 \times 8.85418 \times 10^{-12}\text{F/m})(3 \times 10^{-6}\text{m})^3 \times \\ &\quad \Big(13061.1762 \times (-0.013951) + 7.8442 \times 10^{-5} \times 26238.8669\Big) \\ &= -5.4127 \times 10^{-25}\ \text{N} \end{aligned}$$

The particle's deflection path can be calculated as the dielectrophoretic force field has been calculated and it is assumed that the particles are not charged. The velocity of helium at x is 0.005 m can be calculated by use of equation (A.24)

$$v_{He} = 0.0198\text{m/s} \times \frac{3}{2}\left(\frac{2 \times 0.005}{0.0125} - \left(\frac{0.005}{0.0125}\right)^2\right) = 0.019008\ \text{m/s}$$

The magnitude of the gravitational force in the y direction can be calculated as

$$F_g = 10490\text{kg/m}^3 \times \frac{4}{3}\pi(3 \times 10^{-6})^3 \times 9.81 = 11.6384 \times 10^{-12}\ \text{N}$$

The mean free path was calculated by means of equation (A.12) as

$$\lambda = \frac{1.3806504 \times 10^{-23}\text{J/K} \times 293.15\text{K}}{4\pi \times (0.098 \times 10^{-9}\text{m})^2 \times 98066.5\text{Pa}} = 241.8109\text{nm}$$

The Cunningham correction factor was calculated by means of equation (5.4) as

$$\begin{aligned} C_m &= 1 + \frac{1.246 \times 2 \times 241.8109 \times 10^{-9}}{2 \times 3 \times 10^{-6}} + \\ &\quad \frac{0.42 \times 2 \times 241.8109 \times 10^{-9}}{2 \times 3 \times 10^{-6}} \times exp\left(\frac{-0.87 \times 2 \times 3 \times 10^{-6}}{2 \times 241.8109 \times 10^{-9}}\right) \\ &= 1.100433 \end{aligned}$$

Due to the fact that the particle's t_t (which is equal to 3.16 ms, see section A.4) is larger than the dt of 10 μs, equations (5.15), (5.14), (5.16) are no longer valid as the particles have not reached terminal velocity. After 50 μs the v_x^i = -0.04264 nm/s, v_y^i = 19.4901 mm/s and v_z^i = -0.02242 pm/s. These values are inserted into a rearranged version of equation (5.13) as the velocity of the particle can still increase due to acceleration.

$$
\begin{aligned}
v_x^{i+1} &= -0.04264 \times 10^{-9}\text{m/s} + \frac{10 \times 10^{-6}\text{s}}{10490\text{kg/m}^3 \times \frac{4}{3}\pi(3 \times 10^{-6}\text{m})^3} \times \\
&\left(-1.0296 \times 10^{-18}\text{N} + \frac{0.04264 \times 10^{-9}\text{m/s} \times 6\pi(3 \times 10^{-6}\text{m})19.93 \times 10^{-6}\text{kg/ms}}{1.100433}\right) \\
&= -0.05096\ \text{nm/s} \\
v_y^{i+1} &= 19.4901 \times 10^{-3}\text{m/s} + \frac{10 \times 10^{-6}\text{s}}{10490\text{kg/m}^3 \times \frac{4}{3}\pi(3 \times 10^{-6})^3\text{m}} \times \\
&\left(11.6384 \times 10^{-12}\text{N} - \frac{(19.4901 \times 10^{-3} - 19.008 \times 10^{-3}) \times 6\pi(3 \times 10^{-6})19.93 \times 10^{-6}}{1.100433}\right) \\
&= 19.5840\ \text{mm/s} \\
v_z^{i+1} &= -0.02242 \times 10^{-15}\text{m/s} + \frac{10 \times 10^{-6}\text{s}}{10490\text{kg/m}^3 \times \frac{4}{3}\pi(3 \times 10^{-6}\text{m})^3} \times \\
&\left(-5.4127 \times 10^{-25}\text{N} + \frac{0.02242 \times 10^{-15}\text{m/s} \times 6\pi(3 \times 10^{-6}\text{m})19.93 \times 10^{-6}\text{kgm/s}}{1.100433}\right) \\
&= -0.02679\ \text{pm/s}
\end{aligned}
$$

The particle's current position, after 50 μs, is (x^i = 4.99999999999671 mm, y^i = 964.9467 nm , z^i = 25 mm) and was used in equation (5.17) to obtain the next position of the particle

$$
\begin{aligned}
x^{i+1} &= 4.99999999999671 \times 10^{-3} - 0.050960 \times 10^{-9} \times 10 \times 10^{-6} \\
&= 4.99999999999620\ \text{mm} \\
y^{i+1} &= 964.94672248 \times 10^{-9} + 19.584042 \times 10^{-3} \times 10 \times 10^{-6} \\
&= 1.16078714741\ \mu\text{ m} \\
z^{i+1} &= 25 - 0.026790 \times 10^{-15} \times 10 \times 10^{-6} \\
&= 25.0000000000\ \text{mm}
\end{aligned}
$$

Of particular interest is the fact that in the deterministic deflection model the velocity of the silver particle in the y direction is far greater than in the x direction. v_y^{i+1}/v_x^{i+1} is 3.843×10^8 which means that deflection due to the dielectrophoretic force is negligibly small at helium bulk velocity of 0.0198 m/s. The gravitational force of 11.6384×10^{-12} N is far larger than the dielectrophoresis force in the x direction of -1.0296×10^{-18} N. Therefore it can be concluded that dielectrophoresis is not a viable scrubbing method for silver microparticles.

D.2 Stochastic deflection model

This section is used for the sample calculations of the stochastic deflection model as described in section 5.2. The applied homogeneous electric field is 100 kV/m and the silver particle is assumed to be one ion.

After 1000 time steps the silver particle's x^i and z^i positions are 75.146 μm and -0.22279 μm. The velocity of the particle in the x and z-directions ($v^i_{Ag,x}$ and $v^i_{Ag,z}$) are 475.3932 m/s and 125.10001 m/s.

A random number of 0.0005933, a value between zero and the maximum value of the cumulative distribution function, was selected, see figure 5.5. It was found that this random number is between elements 5 and 6 of the cumulative distribution function by means of a search function, which was written by the author in Python (van Rossum, 2008). The random v_{He} was calculated by taking the sixth element's velocity which equals 457.4384 m/s. The incidence angle of this particle is randomly taken as 4.2583 rad.

With the use of equation (5.29) the relative velocity of the incident helium, where $u_{He,x}$ and $u_{He,z}$ is the x and z components, was calculated as

$$u_{He,x} = 457.4384 \times \cos(4.2583) - 475.393202682 = -676.0296 \text{ m/s}$$
$$u_{He,z} = 457.4384 \times \sin(4.2583) - 125.10001 = -536.1899 \text{ m/s}$$

The magnitude of u_{He} is 862.8532 m/s. Using equation (5.31)

$$\phi = \arctan2(-536.1899, -676.0296) = -2.471 \text{ rad}$$

Note that arctan2 was used as it produces a result of $-\pi < \phi < \pi$. From these calculations it is also clear that the helium is colliding head on with the silver.

The collision radius divided by the radius of the silver particle, r/c, was randomly selected as -0.2771. This value was then inserted into equation (5.32) to calculate

$$\alpha = \sin(-0.2771) = -0.2808 \text{ rad}$$

As the momentum is only transferred in one direction, the velocity of helium acting in this new coordinate system u'_{He} is taken as $u_{He}\cos(\alpha)$ which

$$u'_{He} = 862.8532 \times \cos(-0.2808) = 829.0431 \text{ m/s}$$

This is now used in equation (5.28) to determine the velocity gained due to the momentum transferred

$$U'_{Ag} = \frac{2 \times 4}{4 + 107} 829.0431 = 59.7508 \text{ m/s}$$

To convert this back to the original coordinate system ω is used, which is calculated as

$$\omega = \phi - \alpha = -2.19017971844 \text{ rad}$$

The relative velocity of silver can hence be calculated as

$$\begin{aligned} U_{Ag,x} &= 59.7508 \times \cos(-2.1901) = -34.6873 \text{ m/s} \\ U_{Ag,z} &= 59.7508 \times \sin(-2.1901) = -48.6513 \text{ m/s} \end{aligned}$$

This leads to the velocity of silver after collision

$$\begin{aligned} v^{i+1}_{Ag,x} &= 475.3932 - 34.6873 = 440.7058 \text{ m/s} \\ v^{i+1}_{Ag,z} &= 125.10001 - 48.6513 = 76.4486 \text{ m/s} \end{aligned}$$

Using a rearranged version of equation (5.13) the velocity gained between collisions can be calculated

$$v^{i+1}_{Ag,x} = 440.7058 + 1.6021 \times 10^{-19} \times 100000 \frac{1.9217 \times 10^{-10}}{107 \times 1.66054 \times 10^{-27}} = 458.0348 \text{ m/s}$$

The next position of the particle is then calculated with the use of equation (5.17)

$$\begin{aligned} x^{i+1} &= 75.146 \times 10^{-6} + 458.0348 \times 1.9217 \times 10^{-10} \\ &= 75.234 \times 10^{-6} \text{ mm} \\ z^{i+1} &= -0.2227 \times 10^{-6} + 76.4486 \times 1.9217 \times 10^{-10} \\ &= -0.2081 \times 10^{-6} \text{ mm} \end{aligned}$$

The sample calculations of the stochastic method indicated that particle experiences a force opposing its current velocity, i.e. the assumption of a drag force created by the colliding helium atoms is valid.

Bibliography

Alkhazov, G., Batist, L., Bykov, A., Vitman, V., Letokhov, V., Mishin, V., Panteleyev, V., Sekastky, S. and Fedoseyev, V. (1991). Application of a high efficiency selective laser ion source at the IRIS facility. *Nucl. Instrum. Meth. A*, vol. 306, pp. 400–402.

Atkins, P. (1998). *Physical Chemistry*. 7th edn. Oxford University Press, New York.

Bäumer, R. (1990). *AVR- experimental high-temerature reactor*. VDI Verlag, Düsseldorf.

Bogaerts, A. and Chen, Z. (2005). Effects of laser parameters on laser ablation and laser-induced plasma formation: A numerical modeling investigation. *Spectrochim. Acta, Part B*, vol. 60, pp. 1280–1307.

Bondeson, A., Serdyuk, Y. and Gubanski, S. (2002). High-pressure plasmas for radar wave absorption. Scienticic report, Swedish defence research agency.

Borra, J. (2006). Nucleation and aerosol processing in atmospheric pressure electrical discharges: powders production, coatings and filtration. *J. Phys. D: Appl. Phys*, vol. 39, pp. R19–R54.

Cabalín, L. and Laserna, J. (1998). Experimental determination of laser induced breakdown thresholds of metals under nanosecond Q-switched laser operation. *Spectrochimica. Acta, Part B*, vol. 53, pp. 723–730.

Chang, J., Lawless, P. and Yamamoto, T. (1991). Corona discharge processes. *IEEE Trans. Plasma Sci.*, vol. 19, no. 6, pp. 1152–1166.

Chen, D., Du, H., Li, W. and Shu, C. (2005). Numerical modeling of dielectrophoresis using meshless approach. *J. Micromec. Microeng.*, vol. 15, pp. 1040–1048.

Cronje, P. (2007). Verification of PBMR MIS - summary and results. Unpublished, iThemba LABS.

Crowe, C., Elger, D. and Roberson, J. (2001). *Engineering Fluid Mechanics*. 7th edn. Wiley, New Jersey.

Dekker, A. (1967). *Solid State Physics*. Macmillan, London.

Devins, J., Curdts, E., Endicott, H., Moran, J., Oliver, F., Perkins, J., Sommerman, G. and Starr, W. (1963). Definition of terms related to corona. *IEEE Trans. Power Appar. and Syst.*, vol. 82, no. 69, pp. 1044–1050.

Fedoseyev, V., Huber, G., Köster, U., Lettry, J., Mishin, V., Ravn, H. and Sebastian, V. (2000). The ISOLDE laser ion source for exotic nuclei. *Hyperfine Interact.*, vol. 127, pp. 409–416.

Figliola, R. and Beasley, D. (2000). *Theory and Design for Mechanical Measurements*. 3rd edn. Wiley, New Jersey.

Gold, A. and Bedd, H. (1965). Theory of multiphoton ionization. *Phys. Rev. Lett.*, vol. 14, no. 3, pp. 60–63.

Guru, B. and Hüsyin, R.H. (2005). *Electromagnetic Field Theory Fundamentals*. 2nd edn. Cambridge University Press, Cambridge.

Hirsch, E. (2005). Thermionic emission change through ambient gas diffusion. *J. Phys. D: Appl. Phys.*, vol. 38, no. 14, pp. 2353–2359.

Hook, J. and Hall, H. (1996). *Solid state physics*. 2nd edn. Wiley, Chichester.

Howatson, A. (1965). *An Introduction to Gas Discharge*. Pergamon Press, London.

Inframat Advaced Materials (2002). Silver (Ag) Powder: Datasheet.

Jackschath, C., Rabin, I. and Schulze, W. (1992). Electron impact ionization of silver clusters Ag, n<36. *Z. Phys. D - Atoms, Molecules and Clusters*, vol. 22, pp. 517–520.

Jones, T. (1995). *Electromechanics of particles*. Cambridge University Press, New York.

Jordaan, W. (2009). Depth profile with SXPS.

Kadaksham, A., Sing, P. and Aubry, N. (2004). Dielectrophoresis of nanoparticles. *Electrophoresis*, vol. 25, pp. 3625–3632.

Kadaksham, J., Sing, P. and Aubry, N. (2006). Manupilation of particles using dielectrophoresis. *Mech. res. commun.*, vol. 33, pp. 108–122.

Kang, K., Xuan, X., Kang, Y. and Li, D. (2006). Effects of dc-dielectrophoretic force on particle trajectories in microchannels. *J. Appl. Phys.*, vol. 99, no. 064702.

Kántor, T. (2001). Electrothermal vaporization and laser ablation sample introduction for flame and plasma spectrometric analysis of solid and solution samples. *Spectrochim. Acta, Part B*, vol. 56, pp. 1523–1563.

Koirtyohann, S., Stephen Jones, J. and Yates, D. (1980). Nomenclature system for the low-power argon inductively coupled plasma. *Anal. Chem.*, vol. 52, pp. 1965–1966.

Lide, D. (1996). *CRC Handbook of Chemistry and Physics*. 77th edn. CRC Press, New York.

Lindfield, G. and Penny, J. (2000). *Numerical methods using Matlab*. 2nd edn. Prentince Hall, New Jersey.

Llewellyn-Jones, F. (1966). *Ionization and Breakdown in Gases*. Methuen, London.

Lun, J. (2008). Development of a vacuum arc thruster for nanosatellite propulsion. MscThesis, University of Stellenbosch, Stellenbosch.

Mahoney, W. and Andres, R. (1995). Aerosol synthesis of nanoscale clusters using atmospheric arc evaporation. *Mater. Sci. Eng. A-Struct.*, vol. 204, pp. 160–164.

Masuda, H., Higashitani, K. and Yoshida, H. (2006). *Powder technology handbook*. 3rd edn. Taylor and Francis, New York.

McQuirrie, D. and Simon, J. (1997). *Physical chemistry: A molecular approach*. University Science Books, Sausalito.

Metglo (2009). Metal glazing, 2 Patrys Crescent, Brackenfell, Cape Town.

Miller, J. (1994). *Laser Ablation Principles and Applications*. Springer-Verlag, Berlin.

Miller, J. and Haglund, R. (1998). *Laser Ablation and Desorption*. Academic Press, San Diego.

Mills, A. (1999). *Heat transfer*. 2nd edn. Pretince Hall, New Jersey.

Mishin, V., Fedoseyev, V., Kluge, H., Letokhov, V., Ravn, H., Scheerer, F., Shirakabe, Y., Sundell, S., Tengblad, O. and the ISOLDE Collaboration (1993). Chemically selective laser ion-source for the CERN-ISOLDE on-line mass seperator facility. *Nucl. Instrum. Meth. B*, vol. B72, pp. 550–560.

Mizuno, A. (2000). Electrostatic precipitation. *IEEE Trans. Dielectr. Electr. Insul.*, vol. 7, no. 5, pp. 615–624.

Mohan, N., Undeland, T. and Robbins, W. (1995). *Power electonics: Converters, Applications and Design*. 2nd edn. Wiley, New York.

Moore, W. (1957). *Physical Chemistry*. 3rd edn. Longmans, Green and Co, London.

Neaman, D. (2001). *Electronic circuit analysis and design*. 2nd edn. McGraw Hill, Singapore.

Nichols, W., Malyavanatham, G., Henneke, D., Brock, J., Becker, M., Keto, J. and Glicksman, W. (2000). Gas and pressure dependence for the mean size of nanoparticles produced by laser ablation of flowing aerosols. *J. Nanopart. Res.*, vol. 2, pp. 141–145.

Niu, H. and Houk, R. (1996). Fundamental aspects of ion extraction in inductevily coupled plasma mass spectrometry. *Spectroshim. Acta, Part B*, vol. 51, pp. 779–815.

Ostrovskaya, G. and Zaĭdel', A. (1973). Laser spark in gases. *Sov. Phys.-Usp*, vol. 16, no. 6, pp. 834–855.

Parker, K. (2003). *Electrical operation of electrostatic precipitators*. Institute of Electrical Engineers, London.

Pereiro, M. and Baldomir, D. (2007). Structure of small silver clusters and static response to an external electric field. *Phys. Rev. A*, vol. 75, no. 033202, pp. 1–9.

Peréz, A. (2002). Charge and force on a conducting sphere between two parallel electrodes. *J. Electrostat.*, vol. 56, pp. 199–217.

Sato, K., Kitamura, Y. and Suzuki, H. (1993). Liquid metal ion source, US Patent 5194739.

Sawa, K., Shiozawa, S., Kunitomika, K. and Tanaka, T. (2004). A study of silver behaviour in gas-turbine high temperature gas-cooled reactor. Paper XA9642785, Japan Atomic Energy Research Institute, Ibaraki.

Schulze, W., Frank, F., Charlé, K. and Tesche, B. (1984). The preparation of metal clusters and molecules by means of the gas aggregation technique. *Ber. Nunsenge. Phys. Chem.*, vol. 88, pp. 263–265.

Scütze, A., Jeong, J., Babayan, S., Park, J., Selwyn, G. and Kicks, R. (1998). The atmospheric-pressure plasma jet: A review and comparison to other plasma sources. *IEEE Trans. Plasma Sci.*

Sears, F. (1964). *An Introduction to Thermodynamics, the Kinetic Theory of Gasses, and Statistcal Mechanics*. 2nd edn. Addison-Wesley.

Taylor, D. and Secker, P. (1994). *Industrial Electrostatics: Fundamentals and Measurements*. Wiley, Taunton.

Treschhalov, A., Korge, H., Chizhi, A. and Vill, A. (1997). The role of He2 molecules in plasma kinetics of high pressure helium fast discharge. *Int. Conf. on Phenomena in Ionized Gases*.

van der Merwe, J. (2004). Development and validation of fission product release models and software at PBMR. 2nd International Topical Meeting on High Temperature Reactor Technology, Beijing, China.

van der Merwe, J. and Clifford, I. (2008). Development and application of the PBMR fission product release calculation model. *Nucl. Eng. Des.*, vol. 238, pp. 3092–3101.

van Rossum, G. (2008). Python tutorial.

Wucher, A. (1993). Internal energy of sputtered metal clusters. *Phys Rev. B*, vol. 49, no. 3, pp. 2012–2020.

Zander, A. and Hieftje, G. (1978). Determination of trace metals by microwave plasma spectrometry with an atmospheric pressure helium discharge. *Anal. Chem.*, vol. 50, pp. 1257–1260.

Zeng, J., Jia, H., An, J., Han, X., Xu, W., Zhao, B. and Ozaki, Y. (2008). Preparation and SERS study of triangular silver nanoparticle self-assembled films. *J. Raman Spectrosc.*, vol. 39, pp. 1673–1678.